

THE SERENDIPITOUS EXTRAGALACTIC X-RAY SOURCE IDENTIFICATION (SEXSI) PROGRAM. III. OPTICAL SPECTROSCOPY¹

MEGAN E. ECKART², DANIEL STERN³, DAVID J. HELFAND⁴,
FIONA A. HARRISON², PETER H. MAO^{2,5}, AND SARAH A. YOST^{2,6}

Draft version February 5, 2008

ABSTRACT

We present the catalog of 477 spectra from the *Serendipitous Extragalactic X-ray Source Identification (SEXSI)* program, a survey designed to probe the dominant contributors to the 2 – 10 keV cosmic X-ray background. Our survey covers 1 deg² of sky to 2 – 10 keV fluxes of 1×10^{-14} erg cm⁻² s⁻¹, and 2 deg² for fluxes of 3×10^{-14} erg cm⁻² s⁻¹. Our spectra reach to *R*-band magnitudes of $\lesssim 24$ and have produced identifications and redshifts for 438 hard X-ray sources. Typical completeness levels in the 27 *Chandra* fields studied are 40 – 70%. The vast majority of the 2 – 10 keV-selected sample are active galactic nuclei (AGN) with redshifts between 0.1 and 3; our highest-redshift source lies at $z = 4.33$. We find that few sources at $z < 1$ have high X-ray luminosities, reflecting a dearth of high-mass, high-accretion-rate sources at low redshift, a result consistent with other recent wide-area surveys. We find that half of our sources show significant obscuration, with $N_H > 10^{22}$ cm⁻², independent of unobscured luminosity. We classify 168 sources as emission-line galaxies; all are X-ray luminous ($L_x > 10^{41}$ erg s⁻¹) objects with optical spectra lacking both high-ionization lines and evidence of a non-stellar continuum. The redshift distribution of these emission-line galaxies peaks at a significantly lower redshift than does that of the sources we spectroscopically identify as AGN. We conclude that few of these sources, even at the low-luminosity end, can be powered by starburst activity. Stacking spectra for a subset of these sources in a similar redshift range, we detect [Ne V] $\lambda 3426$ emission, a clear signature of AGN activity, confirming that the majority of these objects are Seyfert 2 galaxies in which the high-ionization lines are diluted by stellar emission. We find a total of 33 objects lacking broad lines in their optical spectra which have quasar X-ray luminosities ($L_x > 10^{44}$ erg s⁻¹), the largest sample of such objects identified to date. In addition, we explore seventeen AGN associated with galaxy clusters and find that the cluster-member AGN sample has a lower fraction of broad-line AGN than does the background sample.

Subject headings: catalogs – surveys – X-rays: galaxies – galaxies: active – X-rays: general – X-rays: galaxies: clusters

1. INTRODUCTION

A primary goal of extragalactic X-ray surveys is to determine the nature and evolution of accretion power in the Universe. Accreting massive black holes are observed over more than five orders of magnitude in luminosity, and exhibit a broad range of intrinsic X-ray absorption (from negligible levels to Compton-thick obscuration with $N_H \gtrsim 10^{24}$ cm⁻²). Additionally, cosmic X-ray sources undergo significant evolution between the current epoch and redshifts of $z \sim 3$. Measuring this enormous phase space requires broadband X-ray surveys extending from essentially the whole sky (to constrain the bright end) to the deepest surveys carried out with the most sensitive telescopes available over sky regions comparable to the telescope field of view.

Enormous progress has been made at the faintest end over

the last five years with Mega-second surveys performed by *Chandra* and *XMM* (see review by Brandt & Hasinger 2005). Together, these surveys have covered more than a thousand square arcminutes to depths of $f_{2-10 \text{ keV}} \lesssim 10^{-15}$ erg cm⁻² s⁻¹. These projects have resolved a significant fraction of the diffuse extragalactic X-ray background (at least in the lower half of the accessible energy band – Worsley et al. 2005). Spectroscopic optical followup has been successful in classifying and measuring redshifts for a large fraction (over half) of the resolved sources.

Also very important in covering the interesting phase space are surveys with depths $f_{2-10 \text{ keV}} \lesssim 10^{-14}$ erg cm⁻² s⁻¹. The slope of the extragalactic X-ray $\log N - \log S$ relation breaks at $f_{2-10 \text{ keV}} = 1 - 2 \times 10^{-14}$ erg cm⁻² s⁻¹ (Cowie et al. 2002; Harrison et al. 2003), so that sources in this flux range dominate the integrated light from accretion. In this brightness range, source densities on the sky are a few hundred per square degree, requiring surveys covering on the order of a square degree or more to obtain statistically useful samples for the study of source properties and the evolution of the population.

A number of programs are surveying regions of this size and depth, accompanied by significant optical followup efforts. The CLASXS survey (Yang et al. 2004) obtained data in a 0.4 deg² contiguous region in the Lockman Hole; optical spectroscopy has identified about half of the sample of 525 objects (Steffen et al. 2004). The ChaMP (Kim et al. 2004) survey utilizes extragalactic *Chandra* pointings largely from the guest observer (GO) program to identify sources that are not associated with the primary target. ChaMP, which ul-

¹ The majority of data presented herein were obtained at the W.M. Keck Observatory, which is operated as a scientific partnership among the California Institute of Technology, the University of California and NASA. The Observatory was made possible by the generous financial support of the W.M. Keck Foundation.

² Space Radiation Laboratory, 220-47, California Institute of Technology, Pasadena, CA 91125

³ Jet Propulsion Laboratory, California Institute of Technology, Mail Stop 169-506, Pasadena, CA 91109

⁴ Columbia University, Department of Astronomy, 550 West 120th Street, New York, NY 10027

⁵ University of California at Los Angeles, Department of Earth and Space Sciences, 595 Charles Young Dr. East, Los Angeles, CA 90095

⁶ University of Michigan, Department of Physics, 2464 Randall Laboratory, 450 Church St., Ann Arbor, MI 48109

timately aims to cover several square degrees over a range of depths, is also accompanied by an optical source identification effort (Green et al. 2004; Silverman et al. 2005). The HELLAS2XMM survey (e.g., Baldi et al. 2002; Fiore et al. 2003; Perola et al. 2004) is taking a similar approach with fields from *XMM-Newton*.

The subject of this paper is the *Serendipitous Extragalactic X-ray Source Identification (SEXSI)* program, a survey using *Chandra* GO and GTO fields specifically selected to obtain a significant sample of identified objects in the flux range from a few times 10^{-13} to 10^{-15} erg cm $^{-2}$ s $^{-1}$. To accomplish this, SEXSI covers more than 2 deg 2 of sky. Harrison et al. (2003, hereafter Paper I) describes the X-ray source sample, Eckart et al. (2005, hereafter Paper II) describes the optical imaging followup, and this paper presents results of the optical spectroscopy. We have 477 spectra, of which 438 are of sufficient quality to provide redshifts and optical classifications. The $L_x - z$ phase space covered by our survey is shown in Figure 1.

In our sample of 438 spectroscopically-identified sources (which have counterpart magnitudes $R \lesssim 24$) we confirm with high significance a number of results found in other surveys. We find that few AGN at $z < 1$ have high rest-frame X-ray luminosities, reflecting a dearth of high-mass, high-accretion-rate sources at low redshift. In addition, our sample of broad-lined AGN peaks at a significantly higher redshift ($z > 1$) than do sources identified as emission-line galaxies. We find that 50% of our sources show significant obscuration, with $N_H > 10^{22}$ cm $^{-2}$, independent of intrinsic luminosity. We have identified nine narrow-lined AGN at $z > 2$ having quasar luminosities ($L_x > 10^{44}$ erg s $^{-1}$). This is consistent with predictions based on unified AGN models.

We investigate in some detail the nature of the large sample of 168 sources classified as emission-line galaxies. These X-ray luminous ($10^{41} - 10^{44}$ erg s $^{-1}$) galaxies have optical spectra lacking both high-ionization lines and evidence for a non-stellar continuum. We conclude that few of these galaxies, even at the low-luminosity end, can be powered by starburst activity. By stacking 21 spectra for sources in a similar redshift range in order to increase the signal to noise, we detect [Ne V] $\lambda 3426$ emission, an unambiguous signature of AGN activity. This suggests that the majority of these sources are Seyfert 2 galaxies, where the high-ionization lines are diluted by stellar emission and reduced in intensity by nuclear extinction.

We organize the paper as follows: § 2 discusses the overall design of the spectroscopic followup program; § 3 describes the data collection and reduction; § 4 details how we determine redshifts and source classifications; § 5 presents the catalog; § 6 discusses the population statistics of the sample; § 7 provides details on the characteristics of each source class as well as the line-free spectra; § 8 discusses the sample completeness and selection effects; § 9 presents the global characteristics of the sample and provides a comparison to other surveys; § 10 explores the nature of emission-line galaxies; § 11 provides a discussion of spectroscopically-identified AGN associated with galaxy clusters; and § 12 provides a summary. We adopt the standard cosmology throughout: $\Omega_m = 0.3$, $\Omega_\lambda = 0.7$, and $H_0 = 65$ km s $^{-1}$ Mpc $^{-1}$. Unless otherwise mentioned, error estimates and error bars refer to 1σ errors calculated with Poissonian counting statistics.

2. SURVEY DESIGN

The SEXSI survey is designed to obtain optical identifications for a large sample of hard (2 – 10 keV) X-ray sources detected in extragalactic *Chandra* fields in the flux range $10^{-13} - 10^{-15}$ erg cm $^{-2}$ s $^{-1}$. This range contains sources which are the dominant contributors to the 2 – 10 keV extragalactic background, filling the gap between wide-area, shallow surveys (e.g., HELLAS – La Franca et al. 2002; ASCA Large Sky Survey – Akiyama et al. 2000; ASCA Medium Sensitivity Survey – Akiyama et al. 2003) and the deep, pencil-beam surveys (e.g., CDF-N – Alexander et al. 2003; Barger et al. 2003; CDF-S – Rosati et al. 2002; Szokoly et al. 2004).

Covering this phase space requires surveying 1 – 2 deg 2 with ~ 50 ksec exposures. SEXSI selected 27 archival, high Galactic latitude fields ($|b| > 20^\circ$), covering a total survey area of more than 2 deg 2 at $f_{2-10 \text{ keV}} \geq 3 \times 10^{-14}$ erg cm $^{-2}$ s $^{-1}$ and more than 1 deg 2 for $f_{2-10 \text{ keV}} \geq 1 \times 10^{-14}$ erg cm $^{-2}$ s $^{-1}$. To maximize sensitivity in the hard band, we selected archival observations taken with the Advanced Camera for Imaging Spectroscopy (ACIS I- and S-modes; Bautz et al. 1998). The exposure times range from 18 to 186 ks, with three quarters of the fields having good-time integrations of between 40 and 100 ks.

Paper I provides details of the X-ray source extraction and analysis; we provide a brief summary here. In each field we initially used `wavdetect` to identify sources in soft (0.3 – 2.1 keV) and hard (2.1 – 7 keV) band images. In a subsequent step, we tested the significance of each source and eliminated sources with nominal chance occurrence probability $P > 10^{-6}$, which led to an average expected rate of ≤ 1 false detections per field. We extracted photons from each source, and used energy-weighted exposure maps to convert background-subtracted source counts to fluxes in the standard soft (0.5 – 2 keV) and hard (2 – 10 keV) bands, adopting a power-law spectral model with photon index $\Gamma = 1.5$. In addition, we corrected the source fluxes for Galactic absorption. We eliminated all *Chandra* target objects from the sample, with the exception of possible galaxy cluster members which we include in the catalog but flag accordingly. The X-ray catalog contains 1034 hard-band-selected sources. An additional catalog of 879 sources which have soft-band detections but which lack hard-band detections is presented in the Appendix of Paper I.

The SEXSI optical followup program is designed to maximize the fraction of spectroscopically identified sources in the survey area. We primarily used the MDM 2.4 m and the Palomar 60-inch and 200-inch telescopes for imaging, and the Keck telescopes for spectroscopy. We image each field in the *R*-band to minimum limiting magnitudes $R_{\text{limit}} \sim 23$, a depth chosen to match the typical limit where classifiable optical spectra can be obtained in 1-hour integrations with Keck. Since the majority of sources in our X-ray flux range have optical counterparts at this limit, this is a good tradeoff between areal coverage and depth.

Paper II describes the optical imaging and counterpart identification in detail. We iteratively matched the optical images to the X-ray catalog, utilizing optical astrometry to correct the *Chandra* pointing error for each field (typically these corrections are $\lesssim 1''$). For the 262 sources with imaging depths $22 < R_{\text{limit}} < 23$, 160 (61%) have identified counterparts, while for the 434 sources with $23 < R_{\text{limit}} < 24$, 291 (67%) have identified counterparts, and for the 167 sources with $R_{\text{limit}} > 24$, 124 (74%) have identified counterparts. Our

total sample of 947 sources with unambiguous photometry (e.g., no contamination from nearby bright stars, etc.) identifies 603 counterparts (64%).

Optical spectra of X-ray counterparts were primarily obtained using multi-slit spectrographs at the W.M. Keck Observatory: the Low Resolution Imaging Spectrometer (LRIS; Oke et al. 1995) on Keck I and the Deep Extragalactic Imaging Multi-Object Spectrograph (DEIMOS; Faber et al. 2003) on Keck II. Our basic slit mask design strategy was to place slits on all identified 2 – 10 keV SEXSI sources with counterpart magnitudes $R \lesssim 23$ (or, occasionally, from imaging in other bands when R -band images were not yet available). For the majority of the masks made for LRIS, these sources received the highest priority; we then filled any extra space on the mask with sources from our soft-band-only catalog, and then with fainter optical counterparts. The soft-band-only spectra are not included in this paper. For DEIMOS masks we followed basically the same procedure. However, DEIMOS’s large field-of-view affords space to place “blind” slits at the X-ray positions of hard-band sources which lack optical identifications.

Table 1 provides a summary of the SEXSI fields and our spectroscopic completeness for each. Note that the optical photometric identification completeness should be taken into account when gauging spectroscopic completeness – most sources for which we have found either very faint optical counterparts or only a limiting magnitude were not pursued spectroscopically.

3. OPTICAL SPECTROSCOPY: DATA COLLECTION AND REDUCTION

Although the majority of the SEXSI spectroscopy was obtained using LRIS on Keck I and DEIMOS on Keck II, a small fraction ($\sim 2\%$) of the spectra were collected with Double-spec (Oke & Gunn 1982) at the Palomar 200 inch (5 m) telescope. Below we describe the data collection and reduction techniques for each of the three instruments. A small subset (19 sources) of the spectra were previously published in Stern et al. (2002a,b) and Stern et al. (2003). Section 8 addresses the composition of the sample obtained from each instrument and possible sample biases that might occur as a consequence of the differing capabilities of the spectrographs; we show any such effects are small in our final sample.

3.1. LRIS Data

The 293 LRIS spectra included in our catalog were collected between September 2000 and June 2002. LRIS has a $5.5' \times 8.0'$ field of view that we typically filled with 5 – 20 slitlets. Our aim was followup of $R \lesssim 23$ SEXSI sources. Exposures of 1 – 2 hours provided sufficient signal to determine redshifts and perform classifications for most such objects (see § 4). The SEXSI source density varies with *Chandra* exposure time and off-axis angle, leading to a large range in slitlets per mask. The masks were machined with $1.4''$ wide slitlets.

LRIS is a dual-beam spectrograph, with simultaneous blue (LRIS-B) and red (LRIS-R) arms. LRIS-R has a 2048×2048 detector with $0.212''$ pixel $^{-1}$. From September 2000 to early June 2002, LRIS-B had a 2048×2048 pixel engineering-grade CCD with a similar platescale to the red-side. In June 2002, prior to our final LRIS observing run, the CCD was replaced by a science-grade mosaic of two 2048×4096 CCDs with $0.135''$ pixel $^{-1}$. The new CCDs were selected to have high near-UV and blue quantum efficiency. Steidel et al.

(2004) provides a more detailed description of the new LRIS-B.

We used the 300 lines mm $^{-1}$ ($\lambda_{\text{blaze}} = 5000$ Å) grism for blue-side observations providing a dispersion of 2.64 Å pixel $^{-1}$ pre-upgrade and 1.43 Å pixel $^{-1}$ post-upgrade. For red-side observations we employed either the 150 lines mm $^{-1}$ ($\lambda_{\text{blaze}} = 7500$ Å) grating providing a dispersion of 4.8 Å pixel $^{-1}$ or the 400 lines mm $^{-1}$ ($\lambda_{\text{blaze}} = 8500$) grating providing 1.86 Å pixel $^{-1}$. In cases where only LRIS-R was available, we used the 150 lines mm $^{-1}$ grating. The 400 lines mm $^{-1}$ grating was only employed when we were using both arms of the spectrograph. We typically split the red and blue channels at 5600 Å though occasionally the 6800 Å dichroic was used. These spectrometer configurations provide wavelength coverage across most of the optical window. The wavelength window for each individual spectrum is included in the catalog (§ 5), since coverage depends on the source position on the slitmask and the particular setup parameters.

The majority of the LRIS observations (227 sources) used both arms of the spectrograph with the 400 lines mm $^{-1}$ grating, while 51 of the earliest LRIS spectra used only LRIS-R. A final 19 spectra used a dichroic, but have only blue-side (4 sources) or red-side (15 sources) coverage due to technical problems during the observations.

Most of our LRIS masks were observed for a total integration time of 1 – 1.5 hr, usually consisting of three consecutive exposures. Between exposures we dithered $\sim 3''$ along the slit in order to facilitate removal of fringing at long wavelengths ($\lambda \gtrsim 7200$ Å). The LRIS data reductions were performed using IRAF⁷ and followed standard slit-spectroscopy procedures. Some aspects of treating the slit mask data were facilitated by a home-grown software package, BOGUS⁸, created by D. Stern, A.J. Bunker, and S.A. Stanford. We calculated the pixel-to-wavelength transformation using Hg, Ne, Ar, and Kr arc lamps and employed telluric emission lines to adjust the wavelength zero point. The spectra on photometric nights were flux-calibrated using long-slit observations of standard stars from Massey et al. (1990) taken with the same configuration as the multislit observations.

3.2. DEIMOS Data

Our 163 DEIMOS spectra were collected over three nights in August 2003⁹. The DEIMOS field of view is $4' \times 16'$, approximately four times that of LRIS, allowing more slitlets per mask. Observations used the 600 lines mm $^{-1}$ grating blazed at 7500 Å with the GG455 order-blocking filter, eliminating flux below 4550 Å. With this setup, the spectrograph afforded spectral coverage from roughly 4600 Å to $1 \mu\text{m}$, covering most of the optical window, though the blue-side sensitivity does not extend as far into the near-UV as does LRIS-B. The observations of each mask were broken into three exposures of 1200 s to allow rejection of cosmic rays; no dithering was performed between exposures to allow for easy adoption

⁷ IRAF is distributed by the National Optical Astronomy Observatory, which is operated by the Association of the Universities for Research in Astronomy, Inc., under cooperative agreement with the National Science Foundation.

⁸ BOGUS is available online at <http://zwolfkinder.jpl.nasa.gov/~stern/homepage/bogus.html>

⁹ A serendipitous galaxy at $z = 6.545$ in SEXSI field MS 1621 was also identified during the DEIMOS observing run. This was the third most distant object known at the time of the discovery, and had interesting implications for the ionization history of the Universe (Stern et al. 2005).

of the pipeline reduction software (see below).

Calibration data consisting of three internal quartz flats and an arc lamp spectrum (Xe, Hg, Ne, Cd, and Zn) were obtained for each mask during the afternoon. The DEIMOS flexure compensation system ensures that the calibration images match the science data to better than ± 0.25 pixels.

The DEIMOS data reduction was performed using the automated pipeline developed by the DEEP2 Redshift Survey Team (Newman et al. 2005). Minor adjustments to the code were needed to process data from slit masks with too few slitlets or a slitlet that was too long for the original code. These changes were performed by both the authors and DEEP2 team members M. Cooper and J. Newman. The pipeline follows standard slit spectroscopy reduction procedures, performing all steps up to and including extraction and wavelength calibration.

3.3. Doublespec Data

While it is impractical to use the Palomar 200 inch (5 m) telescope for spectroscopy of sources fainter than $R = 21$, Doublespec was used in long slit mode for brighter sources that did not fit well onto Keck slit masks. Doublespec is a dual-beam spectrograph; we used the 600 lines mm^{-1} ($\lambda_{\text{blaze}} = 3780 \text{ \AA}$) grating for blue-side observations ($1.07 \text{ \AA pixel}^{-1}$), the 158 lines mm^{-1} ($\lambda_{\text{blaze}} = 7560 \text{ \AA}$) grating for red-side observations ($4.8 \text{ \AA pixel}^{-1}$), and the 5200 \AA dichroic, which provided coverage of most of the optical window. Most of our Doublespec observations were performed for a total integration time of 30 min, usually consisting of three consecutive exposures. Between exposures we dithered along the slit in order to facilitate removal of fringing at long wavelengths. Our small number of Doublespec spectra (ten) were reduced using standard IRAF slit-spectroscopy procedures.

4. REDSHIFT DETERMINATION AND SOURCE CLASSIFICATION

From the 477 spectra collected, we have obtained spectroscopic redshifts for 438 of the 1034 $2 - 10 \text{ keV}$ sources from Paper I. We do not include spectroscopic followup of any of the soft-only sources presented in the Appendix of Paper I, as the goal of our program has always been to focus our telescope and analysis time on the hard-band populations.

To obtain source redshifts, we measure the observed line centers and average the corresponding redshifts. When possible, we avoid using broad lines in determining source redshifts; in particular, we exclude lines such as C IV $\lambda 1549$ that are known to be systematically blueshifted from the object's systemic redshift (Vanden Berk et al. 2001). When possible we measure the narrow oxygen lines, [O II] $\lambda 3727$ or [O III] $\lambda 5007$, although determining source redshifts to $< 1\%$ is not essential for our scientific goals. When our emission or absorption line identification is tentative, we flag the source in the catalog. This occurs in $\sim 5\%$ of the cases – typically faint sources which lack bright, high-ionization lines.

When a source has a reasonable signal yet lacks identifiable spectral features, we include it in the source catalog and document the wavelength range observed. These sources mainly show faint, power-law-like continua, although in a few cases the signal-to-noise is quite high. Sources so faint that the continuum is not clearly detected are excluded from the catalog.

In addition to determining redshifts, our spectroscopic data allows us to group the sources into broad classes based on their spectral features. This classification is independent of the sources' X-ray properties. The broad goal of this classification is to separate sources that *appear* to have normal galaxy

spectra from those that exhibit features characteristic of an active nucleus – high-ionization lines that are either broad or narrow. In detail, our spectral classification is as follows:

- **Broad-Lined AGN (BLAGN):** We classify sources as BLAGN if they have broad ($\text{FWHM} \gtrsim 2000 \text{ km s}^{-1}$) emission lines such as Ly α , C IV $\lambda 1549$, C III] $\lambda 1909$, Mg II $\lambda 2800$, [Ne V] $\lambda\lambda 3346, 3426$, H β , H α . These sources include Type 1 Seyferts and QSOs, which in the unified theory (Antonucci 1993) are objects viewed with the obscuring torus face on and the central nuclear region unobscured. An example of a typical BLAGN optical spectrum is shown in Figure 2.
- **Narrow-Lined AGN (NLAGN):** We classify sources as NLAGN if they have high-ionization emission lines similar to those seen in BLAGN, but with $\text{FWHM} \lesssim 2000 \text{ km s}^{-1}$. Typical high-ionization lines indicating the presence of an AGN are C IV $\lambda 1549$, C III] $\lambda 1909$, and [Ne V] $\lambda 3426$. Low-ionization lines such as Ly α , Mg II $\lambda 2800$, H β , H α , etc., will usually also be present given appropriate wavelength coverage, but are not alone sufficient to classify a source as a NLAGN. Figure 3 provides three examples. These sources are the obscured AGN in the unified model (Antonucci 1993), viewed edge-on with an obscured view of the nucleus. In earlier studies of the lower- z universe, line ratios such as [O III] $\lambda 5007/\text{H}\beta$, [N II] $\lambda 6583/\text{H}\alpha$, etc., have been used to differentiate spectra that show narrow lines due to ionization by hot stars from spectra that show narrow lines due to an active nucleus (e.g., Veilleux & Osterbrock 1987). We do not measure such line ratios or apply them in our classification. Our sources span a large range in redshift and most are faint in the optical. Thus the emitted-frame spectral coverage varies greatly from source to source, and our spectral and spatial resolutions are too low to deblend and measure ratios accurately. There may be a handful of sources classified as ELG (see below) that could be re-classified as AGN-dominated based solely on their line ratios in our data, but this number of sources is expected to be small (< 10).
- **Emission-Line Galaxies (ELG):** Extragalactic sources with narrow emission lines, but with no obvious AGN features in their optical spectra (e.g., high-ionization and/or broad lines) are classified as ELG. The emission lines in these spectra indicate that the ionization mechanism dominating the *optical* light we receive is from hot stars, not from a hard, power-law source. This classification does not rule out the presence of an underlying active nucleus; indeed, we believe the X-ray emission from the vast majority of this subsample does arise from AGN activity. Figure 4 shows two example ELG spectra. These objects typically exhibit narrow lines such as [O II] $\lambda 3727$, H β , and [O III] $\lambda\lambda 4959, 5007$, and often have narrow [Ne III] $\lambda 3869$ emission, CaHK $\lambda\lambda 3934, 3968$ absorption, and the continuum break at 4000 \AA (D4000). Narrow [Ne V] $\lambda 3426$ and other high ionization lines are not detected in our ELG spectra – sources with such lines are classified as NLAGN.
- **Absorption-Line Galaxies (ALG):** We distinguish between galaxies showing emission lines (ELG) and

early-type galaxies (ALG), where the latter have continua marked only by absorption features, notably the D4000 continuum break and the CaHK $\lambda\lambda 3934, 3968$ absorption lines. Figure 5 shows an example spectrum.

- **Stars:** SEXSI fields are selected to be at high Galactic latitude to avoid contaminating our extragalactic sample with 2 – 10 keV emitting stars, but we do identify a small number of Galactic stars as optical counterparts (at $z = 0$). Seven of the optically-bright SEXSI sources are identified in the literature as stars (Paper II); the other sources so identified are from our spectroscopy of fainter sources. Section 7.6 discusses the bright stars in more detail and assesses the possibility that the optically-fainter objects are chance coincidences.

As mentioned above, these classifications depend only on the optical spectroscopic appearance, not on X-ray properties such as luminosity or intrinsic obscuring column density. With the exception of only a few sources, the identified extragalactic SEXSI sources have X-ray luminosities which suggest the presence of an accreting supermassive black hole. The emission-line galaxies, which are prevalent in our sample, do not show any optical indication of emission lines from atoms ionized by an X-ray source with copious hard X-ray emission. Instead, the ELG lines are typical of normal galaxies with lines from atoms excited by at best moderately energetic photons that can be produced thermally by the hottest stars. This apparent discrepancy in the optical and X-ray source properties is discussed further in § 10.

5. THE CATALOG

In Table 2 we present the catalog of 477 hard-band SEXSI sources with optical spectroscopic data; the catalog is also available in machine-readable format in the online version of the *Astrophysical Journal*. Complete X-ray data and optical photometry for these sources are presented in Papers I and II, respectively. The remaining ~ 550 unidentified sources from the complete sample of 1034 hard-band SEXSI sources do not have optical spectroscopic data and are omitted from this catalog. The first six columns present the X-ray source data, while the following columns present optical counterpart information – photometric data followed by spectroscopic data. The final columns describe the X-ray luminosity and the column density – quantities determined by combining the X-ray data with the redshift.

Column 1 presents source names, designated by “CXO-SEXSI” followed by standard truncated source coordinates. X-ray source positions, α_x and δ_x , corrected for the mean X-ray-to-optical offsets to eliminate *Chandra* pointing errors, are shown in columns 2 – 3. Column 4 lists the off-axis angle (OAA, the angular distance in arcmin of the source position from the telescope aim point). The 2 – 10 keV flux (in units of 10^{-15} erg cm^{-2} s^{-1}), converted from counts assuming $\Gamma = 1.5$ and corrected for Galactic absorption, is presented in column 5, while column 6 gives the source hardness ratio, $HR = (H - S)/(H + S)$, where H and S are photons cm^{-2} s^{-1} in the 2 – 10 keV and 0.5 – 2 keV bands, respectively. Here, as in Paper II, we quote hardness ratios derived from the net soft X-ray counts recorded at the hard-band source position when there was not a significant soft-band source detected (as distinct from Paper I, in which these cases were reported as

$HR = 1$). In addition, for a subset of these cases, when the soft-band counts recorded at the hard-band position were less than twice the soft-band background counts, the HR is considered a lower-limit, is flagged as such in the catalog, and is set to $HR = (H - S_{\text{limit}})/(H + S_{\text{limit}})$, where $S_{\text{limit}} = 2 \times$ soft-band background counts corrected by the exposure map.

The data describing the optical counterparts begin in column 7, with the photometric optical counterpart flag (optflag), a code essential for interpreting the optical photometric data (see Table 2 footnote). Note that in this spectroscopic catalog the majority of entries in this column are optflag = 1, indicating a solid optical identification, since a successful spectroscopic identification depends on having a counterpart bright enough that emission lines or absorption features are detectable. In a handful of cases the optical flag is a 2, indicating a limiting magnitude. These cases occur either when we placed a slitlet on an optical counterpart identified in a band other than R , or when a slitlet was placed ‘blindly’ at the X-ray source position even though no optical counterpart was present to the depth of our imaging data.

Column 8 is the R -band magnitude of the optical counterpart; in the next column we show the limiting R magnitude for the image from which the optical counterpart, or a limit thereto, was derived. Next we present the logarithmic X-ray-to-optical flux ratio (column 10), given by the relation

$$\log(f_x/f_o) = \log f_{2-10 \text{ keV}} + (R/2.5) + 5.50, \quad (1)$$

derived using the Kron-Cousins R -band filter transmission function (see Paper II and references therein). Note that special attention must be paid to the optical flag when interpreting the data of columns 8 – 10. For example, if the code is a 2 (optical counterpart not detected), then columns 8 and 10 describe limits on each quantity.

The optical spectroscopic data begins with the redshift in column 11, followed by the classification in column 12 (see § 4 for details of the redshift and classification determinations). Column 13 provides notes on individual sources where necessary.

The rest-frame wavelength range in angstroms for each optical spectrum is recorded in column 14; when a source spectrum shows continuum only and no redshift has been determined, we present the observed-frame wavelength range. This column is essential for determining which spectral features are accessible for a given source. It is important to know, for example, whether the absence of high-ionization lines (typical of AGN and necessary for an AGN classification) is a consequence of non-detection in the measured spectrum or as the result of inadequate spectral coverage. In most cases both the blue and red sides of the spectrographs were employed; if this is the case and there is a significant spectral coverage gap ($> 100 \text{ \AA}$) between the red and blue sides, a note is added in column 13.

Column 15 presents the log of the absorbed rest-frame 2 – 10 keV X-ray luminosity in erg s^{-1} , calculated from the hard-band flux (column 5) and the redshift assuming an X-ray photon index of $\Gamma = 1.5$.

The final three columns (16–18) present the log of the neutral hydrogen column density (N_H) in cm^{-2} and the associated 1σ lower- and upper-limit to the value. These values are determined by X-ray spectral fitting of each source using XSPEC¹⁰, a spectral fitting program. Since many SEXSI sources have a low number of counts in the X-ray we did

¹⁰ Available at <http://heasarc.gsfc.nasa.gov/webspec/webspec.html>

not allow a many-free-parameter fit; instead, we performed the fits assuming an intrinsic power-law spectrum with photon index $\Gamma = 1.9$ typical of AGN continua. We fixed Γ and the Galactic N_H at $z = 0$ and allowed only the intrinsic column density at the source redshift to vary. The Galactic N_H value used for each field is given in Paper I, Table 2. The photoelectric absorption was determined using Wisconsin cross-sections (Morrison & McCammon 1983). The fitting was performed using C-statistic minimization instead of chi-squared minimization since the observed data bins have few counts (Cash 1979, and the XSPEC Manual, Appendix B). The fits use data from 0.3 – 7.0 keV, to match the energy range we used to extract counts in Paper I. The X-ray spectral data analysis was aided greatly by `acis_extract`¹¹ Version 3.91 (Broos et al. 2002), software written in IDL that assists in performing the many CIAO and XSPEC tasks involved in analyzing the spectra of large numbers of sources observed with ACIS. For the spectral analysis presented here we use CIAO Version 3.2 and CALDB Version 3.1.

Spectra were extracted for each source with a spectroscopic redshift (excluding stellar sources at $z = 0$). We choose 1.4967 keV as the primary PSF energy at which the PSF fraction is to be computed, and a PSF fraction of 0.8. Individual auxiliary response files (ARF's) and redistribution matrix files (RMF's) were calculated for each source.

We extracted a background spectrum for each source from a local circular background region that includes at least 100 counts and an exposure ratio between background and source region of at least four, taking care to mask out all X-ray sources (SEXSI sources, including soft-only sources, target point sources, and extended cluster emission). The background spectra were scaled based on the ratio of total exposure in the source extraction region to that of the background region.

For ACIS-I observations, all sources on all chips were fit; for ACIS-S observations, only sources on chips 6-8 were fit since PSF libraries do not exist for chips 2-3 given an ACIS-S pointing. Fourteen SEXSI sources fall in this category and are marked in catalog; the N_H values reported for them are derived instead using hardness ratios: we determine what column density is necessary, given the source redshift, to produce the measured hardness ratio assuming an underlying intrinsic power-law spectrum with photon index $\Gamma = 1.9$. We use WebPIMMS¹² for this calculation.

Throughout the paper, the luminosities we refer to are the obscured (observed) luminosities presented in column 15, unless we specifically indicate that we are using intrinsic, unobscured luminosities, corrected for absorption by the obscuring column density at the source redshift. To calculate the unobscured luminosity we multiply L_x in column 15 by an approximate correction factor calculated using WebPIMMS, assuming an intrinsic $\Gamma = 1.9$, the best-fit N_H value, and the source redshift.

We now discuss the 23 sources flagged with an 'A': sources whose optical spectra are from potential counterparts which lie just outside the formal matching area. In the photometry catalog from Paper II, these sources were listed as having limiting R -magnitudes (optflag=2) since there were no optical counterparts in the search area. We include the spectroscopic information for these sources in the main catalog here (Table 2) and present the new photometric and astrometric

information in Table 3. This Table lists the X-ray source position as well as the new R -magnitude and its error and the offset between the X-ray and optical position (in R.A. ($\Delta\alpha = \alpha_x - \alpha_o$), Dec. ($\Delta\delta = \delta_x - \delta_o$), and total position error ($\Delta r = \sqrt{\Delta\alpha^2 + \Delta\delta^2}$). Column (9) gives the original X-ray search radius (which depends on *Chandra* OAA), and the final column presents $\log(f_x/f_o)$.

Of these 23 sources, 5 are BLAGN, 1 is a NLAGN, 12 are ELGs, 2 are ALGs, and 3 are stars. Given the low surface density of AGN on the sky, we assume that all of the six sources with spectra indicative of AGN activity are true counterparts. Comparing the BLAGN and NLAGN to the ELGs, we see that $6/212 = 3\%$ of the active galaxies are outside the search radius (as expected for radii defined as approximately 2σ error radii), while $12/168 = 7\%$ of the ELG are outside. The surface density of ELGs is also much higher than that of AGN, and thus it is likely that some of the 12 ELG are chance coincidences. The numbers for stars ($3/19 = 16\%$) and ALG ($2/8 = 25\%$) are even higher; these objects are even more likely to be chance coincidences (see also § 7).

The number of false matches due to an optical source randomly overlapping the matching search area depends on the depth of both the X-ray and optical images as well as the size of the match area, which is determined by the X-ray source off-axis angle. In Paper II, Section 3 we estimated the number of false matches considering the probability that an optical source would overlap the X-ray match area; now that we have our set of identifications, we can estimate the number of false matches on a source-by source basis, taking into account the particular match areas and optical magnitudes of the identified sources in each class as well as the optical source density of that class.

The optical sources that dominate in our high-Galactic latitude fields are normal galaxies, sources that would be classified spectroscopically as ELG or ALG. The false match rate will be lower than that estimated in Paper II for several reasons, most importantly that the R -magnitude of many of the spectroscopically identified sources are considerably brighter than the limiting magnitudes of the optical images. In addition, since *Chandra* is more sensitive closer to the aim point, the source density is highest for low-OAA sources with the smaller match areas, and spectroscopic observing efficiency favors these high-space-density sources. Taking into account each ELG and ALG match area and R -magnitude, we calculate the false match probability for each source. Considering the 176 ELG and ALG we estimate a total of $\lesssim 4$ false ELG or ALG matches. The surface density of (optically-identifiable) active galaxies is $\sim 100\times$ lower than the normal-galaxy surface density for $R \lesssim 23$ in optical surveys (e.g., Wolf et al. 2003), thus we estimate that there will be < 1 false NLAGN or BLAGN match. These estimates support our assertion that all of the BLAGN and NLAGN from Table 3 are true counterparts.

6. HARD X-RAY SOURCE POPULATION STATISTICS

6.1. Redshift distribution

Figure 6 shows the redshift distribution for the 419 spectroscopically-identified extragalactic sources (the 19 stars are excluded). The top panel (a) presents the entire distribution with the optical spectroscopic classifications indicated in different shades. Panels (b) – (e) present the same z -distribution with a different source class shaded in each panel to highlight their very different redshift distributions.

¹¹ Available at http://www.astro.psu.edu/xray/docs/TARA/ae_users_guide.html.

¹² Available at <http://heasarc.gsfc.nasa.gov/Tools/w3pimms.html>

These plots show that the 2 – 10 keV sources are dominated by two classes: BLAGN which show the typical broad, high-ionization-line signature indicative of gas near a source emitting copious hard X-rays, and ELGs, a class of sources that show only emission lines typical of normal galaxies.

The BLAGN population (shaded in panel (b)) exhibits a broad redshift distribution; it includes 50% of the identified sources and has a mean redshift $\langle z \rangle_{\text{BLAGN}} = 1.46 \pm 0.75$, with objects ranging from $z = 0.06$ to our highest redshift source at $z = 4.33$.

The next panel (c) shows the emission-line galaxies, which comprise 40% of the identified sources. This redshift distribution is distinct from that of the BLAGN, with a much lower average redshift as well as a much tighter distribution about the average: $\langle z \rangle_{\text{ELG}} = 0.75 \pm 0.36$. Note that there are no ELGs found above $z = 1.56$, and only three are above $z = 1.4$ (two of which are flagged as tentative identifications). There are two essential facts to keep in mind when discussing the ELG redshift distribution. First, although the optical spectra of these sources are identified as a result of emission from the host galaxy, the 2 – 10 keV X-ray luminosities are, with the exception of eleven sources, above $10^{42} \text{ erg s}^{-1}$, which is too high to be produced purely from stars and stellar remnants in a star-forming galaxy (see § 10.1). Second, the decline in sources above $z \sim 0.8$ does not necessarily represent the underlying distribution of hard X-ray emitting ELG in the universe, but is more likely a result of observational biases. There are several strong selection effects that dominate at higher redshift, most importantly the fact that as a typical galaxy is seen at greater distances, it gets too faint for us to identify optically (see § 8); the redshift desert – the absence of strong emission lines within the typical wavelength regime covered – also militates against finding ELGs above $z \approx 1.4$. Figure 7 presents a scatter plot of R -magnitude versus redshift, showing the rapid rise in ELG (triangles) R -magnitude as z increases as compared to, for example, the broad spread in R over a large z range exhibited by the BLAGN (black crosses).

Panel (d) of Figure 6 displays the redshift range for the 32 NLAGN, sources that show narrow high-ionization lines indicative of an obscured active nucleus. These sources comprise only $\sim 8\%$ of the total identified sources. The redshift distribution is broad, with $\langle z \rangle_{\text{NLAGN}} = 1.41 \pm 1.01$, similar to the BLAGN distribution.

The final category of sources are the absorption line galaxies (ALG) that make up only a very small fraction of our sample. These, like the ELG, are found primarily at $z < 1$ ($\langle z \rangle_{\text{ALG}} = 0.64 \pm 0.23$), with none at $z > 1.2$. Selection effects similar to those that affect the identification of ELGs also constrain this distribution.

6.2. X-ray flux and X-ray-to-optical flux ratio distributions

Figure 8 shows the 2 – 10 keV flux distribution for spectroscopically-identified extragalactic sources with $R < 22$ (top panel) and $R > 22$ (bottom panel); source classes are indicated by shading. Not surprisingly, the distribution of optically-fainter sources has a lower average $f_{2-10 \text{ keV}}$ than does the distribution of $R < 22$ sources. This effect has been seen previously in many of the *Chandra* and *XMM-Newton* surveys (e.g., Hornschemeier et al. 2001). At all but the faintest fluxes the optically-brighter distribution is dominated by BLAGN (black), while the optically-fainter distribution is dominated by ELG (dark gray). The relationship between R -magnitude distribution, redshift, and source class will be explored in detail in § 10.2.

A related distribution is the $\log(f_x/f_o)$ distribution for identified extragalactic SEXSI sources presented in Figure 9. Again, source classes are indicated by shading. The large majority of SEXSI sources are found with $-1 < \log(f_x/f_o) < 1$, typical values for AGN. The higher values of $\log(f_x/f_o)$ generally indicate more obscuration – the 2 – 10 keV light is relatively unaffected by the obscuring material while the AGN optical light is absorbed. The highest $\log(f_x/f_o)$ sources in the identified sample are dominated by ELG.

6.3. X-ray luminosity distribution

The majority of the spectroscopically-identified SEXSI sources have 2 – 10 keV luminosities between 10^{43} and $10^{45} \text{ erg s}^{-1}$; all but twelve sources (eleven ELGs, one NLAGN) have $L_x > 10^{42} \text{ erg s}^{-1}$. Figure 10 shows the (a) 2 – 10 keV and (b) 0.5 – 2 keV luminosity distributions. Since SEXSI is a purely hard-band-selected sample, the top panel includes all identified sources, while the bottom panel displays the subset of these sources having significant soft-band *Chandra* detections as well as a dashed histogram showing upper limits to sources undetected below 2 keV. In addition, Figure 11 shows a scatter plot of HR versus 2 – 10 keV luminosity.

The BLAGN tend to be softer sources – they mainly fall below $HR \sim 0.2$ in Figure 11 – and thus most have significant soft detections and are included in black in both panels of Figure 10. The BLAGN dominate the higher-luminosity end of the 2 – 10 keV distribution, while they comprise almost the entirety of the high-luminosity end of the 0.5 – 2 keV distribution. The other contribution to the high-luminosity hard-band sources is from the NLAGN. These tend to be harder (probably obscured) sources; thus, their corresponding 0.5 – 2 keV luminosities are lower (four have no soft-band detections).

The ELG dominate the 2 – 10 keV luminosity distribution below $\sim 10^{43.5} \text{ erg s}^{-1}$ where the BLAGN distribution falls away and the ELG numbers rise. The ELGs have a broad range of HR s; thus, there are many ELG (26) without significant soft detections. The limit to these detections are shown in the dashed histogram.

Although they are few in number, the ALG we do detect all have 2 – 10 keV luminosities between $10^{42.5}$ and $10^{44} \text{ erg s}^{-1}$, indicating all likely host hidden AGN. A subset of our ELG plus all of our ALG represent the population of sources dubbed X-ray Bright, Optically Normal Galaxies (XBONGs; see Comastri et al. 2002, and references within), sources that show X-ray luminosities indicative of AGN activity but which lack optical spectroscopic indication of the underlying AGN.¹³

6.4. Absorbing column density distribution

Figure 12 presents the N_H distribution for BLAGN, ELG, and NLAGN. ALG are omitted from this plot owing to their small number (see § 7.4). The BLAGN (top panel) are distributed broadly in N_H , with many more unobscured ($N_H < 10^{22} \text{ cm}^{-2}$) sources than for either the ELG or NLAGN populations. A total of 60 (29%) of the BLAGN have $N_H > 10^{22} \text{ cm}^{-2}$, while 149 (71%) have $N_H < 10^{22} \text{ cm}^{-2}$. Note that inclusion in our sample requires a significant hard-band X-ray

¹³ We refrain from using the term “XBONG” further in this paper because it lacks a clear definition; e.g., does XBONG refer to all X-ray luminous sources that lack optical AGN lines or *only* such sources that have optical spectra dominated by stellar absorption features?

detection – we expect that many of the 879 soft-only sources presented in Table 6 of Paper I will be unobscured BLAGN, and thus the population statistics and N_H distributions will be very different for a sample selected in the full-band (0.5 – 8 keV). The middle panel of Figure 12 presents the ELG. The majority of these sources have $N_H > 10^{22} \text{ cm}^{-2}$ – only 27% (43 sources) have $N_H < 10^{22} \text{ cm}^{-2}$. The NLAGN sources appear even more obscured than the ELG. Of the 32 NLAGN only six (19%) have $N_H < 10^{22} \text{ cm}^{-2}$, with more than half the sample having $N_H > 10^{23} \text{ cm}^{-2}$.

7. SOURCE CLASSES

7.1. Broad-lined AGN

The BLAGN are the most common source type in our spectroscopically-identified sample, comprising over half of all sources; they are by far the dominant source type above $z \gtrsim 1.4$. At the highest luminosities, these are (type 1) quasars; the lower luminosity sources are Seyfert 1 galaxies. They are also the easiest type of source to identify over a broad redshift range; their optical counterparts tend to be bright and they have easily-detectable broad emission lines. Table 4 gives a list of commonly detected lines and the percentage of time each is detected. Figure 13 shows the hardness ratio distribution split by R -band magnitude, with the top panel including sources with $R < 22$ and the bottom panel showing the optically-fainter sources. At $R < 22$ the BLAGN, shown in black, dominate the distribution, with a sharp peak at $HR \sim -0.5$. In Paper II we speculated that this HR peak near -0.5 was due to unobscured Seyferts and quasars, since that HR corresponds to a power-law photon index (Γ) between 1.8 and 1.9, a typical value for unobscured broad-line AGNs; the spectroscopy presented here confirms that conjecture.

Figure 12 shows the N_H distribution of the BLAGN in the top panel. In the unified AGN model, the existence of broad lines indicates a relatively unobstructed view to the central regions of the nucleus with low obscuring column densities ($N_H < 10^{22} \text{ cm}^{-2}$). While our BLAGN do have the lowest mean HR among our four source classes, we still find that $29\% \pm 4\%$ have $N_H > 10^{22} \text{ cm}^{-2}$, indicating significant X-ray absorption. However, a significant fraction of these sources are at a high enough redshift that their N_H values are less-well constrained due to the absorption edges shifting out of the *Chandra* bandpass (see lower right panel of Figure 14 and § 8). To quantify this effect, we consider the 114 BLAGN at $z < 1.5$; only 12% of this subset have $N_H < 10^{22} \text{ cm}^{-2}$, compared to 29% for BLAGN at all redshifts. For the 62 BLAGN with $z < 1$, the fraction is even lower (9%). This systematic trend also likely explains the tendency for many of the most luminous BLAGN in Figure 12 to be the most obscured. SEXSI, as with any flux-limited survey, has a redshift-luminosity relation (Figure 1): our most distant sources are the most luminous sources, and this systematic effect makes them also appear most obscured.

Furthermore, the column density measurements can be affected by changes in the Galactic N_H (which is fixed during the spectral fitting): small underestimates in the true Galactic N_H can give rise to overestimates of the intrinsic column density. We note that, for consistency with all previous work, we have used for Galactic absorption column density the N_{HI} derived from 21 cm observations (Dickey & Lockman 1990). This common practice is incorrect, however; the X-ray absorption column density is two to three times the N_{HI} value, since it is the heavy elements, rather than hydrogen, that absorb X-rays, and they are present in the molecular and ionized

phases of the ISM as well as in the atomic phase (e.g., Iyengar et al. 1975). Doubling or tripling the Galactic N_H value can reduce the inferred intrinsic column density by a large factor, particularly for high-redshift sources, and particularly for sources from fields with relatively large Galactic column densities. Indeed, we find the fraction of high- N_H BLAGN monotonically increases as the Galactic column density increases, from 25% for the 10 fields with $N_H < 2 \times 10^{20} \text{ cm}^{-2}$, to 28% for the eleven fields with $2 < N_H < 7 \times 10^{20} \text{ cm}^{-2}$, to 32% for the four fields with $N_H \sim 9 \times 10^{20} \text{ cm}^{-2}$, to 70% for the two fields with $N_H \sim 20 \times 10^{20} \text{ cm}^{-2}$. Any use of the N_H distribution in this, and all other, survey paper(s) for quantitative purposes must take the uncertainty in Galactic column density and the insensitivity of measurements for high-redshift sources into account.

The Doppler-broadened emission lines exhibit a distribution of widths; for the purposes of consistency, SEXSI puts a strict cutoff between narrow- and broad-lined sources at 2000 km s^{-1} , following Veilleux & Osterbrock (1987). Some sources have a line or lines that are just above this width cut and thus are classified as BLAGN, although their other properties may be more similar to a typical NLAGN. Our BLAGN classification includes sources with broad-absorption lines blue-shifted with respect to the object redshift (BALQSO) or broad-absorption at the source redshift. Of the nine sources with $N_H > 10^{23} \text{ cm}^{-2}$, four of the sources are noted as possible BALQSO's, a type of quasar associated with high N_H values (e.g., Gallagher et al. 2002).

7.2. Narrow-lined AGN

The NLAGN, comprising 8% of our sample, tend to be both the most obscured objects and highly luminous. Of our 32 NLAGN, five had no optical counterpart in our imaging — four of these were blind pointings at the X-ray positions in fields with $R_{\text{limit}} = 23 - 24$, while the fifth was from our shallowest field with $R_{\text{limit}} = 21.1$. The 27 NLAGN with optical counterpart photometry have $\langle R \rangle = 22.0 \pm 1.6$, while the BLAGN have $\langle R \rangle = 20.9$.

As mentioned in § 4, the redshift distribution of the NLAGN is broad, extending over the redshift range $z = 0 - 4$. The NLAGN are the only narrow-lined sources in the sample with $z > 1.5$. This fact is largely a consequence of a two-part selection effect: 1) bright, high-ionization UV emission lines are available only for objects at higher z , while we reach the redshift desert for typical galaxy emission lines found in ELG at $z > 1.5$, and 2) for redshifts sufficiently high that $\text{Ly}\alpha$ moves into the optical window, normal galaxies would be too faint both optically and at X-ray energies in our moderate-depth, wide-area survey. In addition, the higher mean luminosity of the NLAGN makes them visible to higher redshift.

For the NLAGN, we find an average (obscured) luminosity near $10^{44} \text{ erg s}^{-1}$: $\langle \log L_{2-10 \text{ keV}} \rangle = 43.8 \pm 0.6$. Fifteen sources have obscured quasar luminosities, with $L_{2-10 \text{ keV}} > 10^{44} \text{ erg s}^{-1}$ and, of these, 73% are found at $z > 1.5$. Twelve out of these fifteen galaxies have $R > 23$, while two have limiting R magnitudes of 21.1 and 22.9, and one has $R = 21.7$. Of the sources with lower luminosities, two have luminosities near $10^{42} \text{ erg s}^{-1}$. The other fifteen have $43.0 < \log L_{2-10 \text{ keV}} < 44.0$. The non-quasar luminosity ($L_x < 10^{44} \text{ erg s}^{-1}$) sources are all found at redshifts below $z = 1.5$, with $0.3 < z < 1.3$. The luminosities presented in the catalog and referred to in this paragraph are all *obscured* 2 – 10 keV rest-frame luminosities, uncorrected for the intrinsic obscuring column. Since the majority of the NLAGN are obscured, their intrinsic luminosities

are larger. At $z = 0$ and $N_H < 10^{23} \text{ cm}^{-2}$ unobscured luminosity will be increased by a factor of $\lesssim 2$, while at $N_H = 10^{24} \text{ cm}^{-2}$ the unobscured X-ray luminosity increases by a factor of ~ 10 . At higher redshifts this increase is not as large since the lower energy X-rays that are most subject to absorption shift out of the observed frame; at $z = 1$ ($z = 2$) the $N_H < 10^{23} \text{ cm}^{-2}$ unobscured luminosity is increased by a factor of ~ 1.2 (~ 1.04) and the $N_H = 10^{24} \text{ cm}^{-2}$ unobscured luminosity increases by ~ 2.6 (~ 1.36). Using unobscured luminosities, 17 (53%) of NLAGN have quasar luminosities.

7.3. Emission-line galaxies

One of the surprising discoveries made by the various *Chandra* and *XMM-Newton* surveys conducted to date is the large population of X-ray sources that lack AGN signatures in their optical spectra, and yet have X-ray luminosities too high to be powered by stellar emission alone. In § 10 we discuss the nature of these sources; here we explore the properties of the ELG found in our sample. Table 4 shows the typical emission lines detected in our ELG spectra (e.g., [O II] $\lambda 3727$, [O III] $\lambda 5007$, etc.). In addition, it shows that 45% of the 148 ELG with the requisite wavelength coverage show CaHK $\lambda\lambda 3934, 3968$ absorption and 42% of the 146 ELG with requisite wavelength coverage show the D4000 break.

Of the 168 ELG, we find an average (obscured) luminosity nearly an order of magnitude lower than for the NLAGN: $\langle \log L_{2-10 \text{ keV}} \rangle = 43.14 \pm 0.05$ (this rises to $\log L_x = 43.25 \pm 0.04$ if we exclude the eleven sources with $L_x < 10^{42} \text{ erg s}^{-1}$ which, in principle, could be starburst galaxies – but see § 10). Thirteen sources (8%) have (obscured) quasar luminosities, $> 10^{44} \text{ erg s}^{-1}$. The majority of the ELG tend to be obscured and, thus, their intrinsic luminosities are larger; considering unobscured luminosities, 16 (9%) ELG have quasar luminosities.

Twelve identified extragalactic SEXSI sources have $L_{2-10 \text{ keV}} < 10^{42} \text{ erg s}^{-1}$; eleven of the twelve are classified as ELG with $0.09 < z < 0.34$. In § 10.1 we discuss these sources and the possibility that their X-ray emission is starburst-dominated instead of AGN-dominated.

7.4. Absorption-line galaxies

Absorption-line galaxies are not found in great numbers in our survey. Although nearly half of our ELG spectra show absorption features, such as CaHK absorption and/or the D4000 break, those sources also have emission lines, most frequently [O II] $\lambda 3727$. With 98% of our spectroscopy from the Keck 10 m telescopes, our ability to detect faint lines is greater than in surveys that use smaller telescopes and thus our identification statistics may be skewed towards ELG. In addition, some surveys (e.g., ChaMP – Silverman et al. 2005) classify sources as ALG even if emission lines are detected.

Of the 438 sources with redshift and classification information, only 8 ($< 2\%$) are identified as ALGs. Of these eight, two are flagged as having only a tentative line identification, meaning their redshift and class identification is likely but not secure. In addition, two other ALGs are flagged as falling just outside the X-ray-to-optical counterpart search area (see Table 3). The distances of these two objects from the edges of their respective search areas are $\sim 1''$, among the larger offsets found in Table 3. One more source identified in the catalog is flagged as an ALG that is identified using the spectrum of one of two optical sources within the X-ray-to-optical search area — we would need additional data (e.g., a spec-

trum of the other source or an on-axis *Chandra* observation) to determine the true counterpart identification.

Setting aside these special cases, we find that there are only three sources with a secure identification as an ALG — less than 1% of the identified sources. This fraction is lower than in some other surveys, as discussed further in § 9.1.

7.5. Line-free spectra

Of the 477 spectra we collected, 39 exhibit roughly power-law continuum emission with no detectable line emission. Here we explore the possibility that the sources are BL Lac objects – AGN that have X-ray and radio emission but show no emission lines in their optical spectra – and the alternative notion that they are the higher-redshift end of the ELG distribution.

7.5.1. BL Lac Contribution

Prominent among the serendipitous sources found in the first wide-area X-ray imaging survey – the *Einstein Medium Sensitivity Survey* (EMSS; Gioia et al. 1990; Stocke et al. 1991) – were BL Lac objects which comprised $\sim 6\%$ of the point sources detected. Subsequent radio and X-ray surveys for BL Lacs have left the population statistics of this relatively rare AGN class somewhat uncertain owing to the non-Euclidean $\log N - \log S$ relation for X-ray-selected objects, and the debate over the relative proportions of the X-ray-bright and radio-bright segments of the population. The two recent X-ray surveys using, respectively, the whole *ROSAT All-Sky Survey* (RASS) and the Greenbank radio catalog (Laurent-Muehleisen et al. 1999), and the *ROSAT/VLA North Ecliptic Pole* survey (Henry et al. 2001) define the $\log N - \log S$ relation for X-ray-selected objects down to a flux of $1 - 3 \times 10^{-13} \text{ erg cm}^{-2} \text{ s}^{-1}$ in the $0.5 - 2 \text{ keV}$ band. Thus, reaching the SEXSI flux limit of $10^{-15} \text{ erg cm}^{-2} \text{ s}^{-1}$ requires an extrapolation of nearly two orders of magnitude and a shift from soft X-rays to hard X-rays. Our detection of BL Lacs, or a lack thereof, could be constraining.

Adopting the mean power law slope of $\Gamma = 2.2$ derived from a large collection of RASS-detected BL Lacs by Brinkmann et al. (1997) and assuming only Galactic absorption, the $2 - 10 \text{ keV}$ flux should be 95% of the $0.5 - 2 \text{ keV}$ band flux. Using the SEXSI coverage of 1 deg^2 at $10^{-14} \text{ erg cm}^{-2} \text{ s}^{-1}$ and 0.1 deg^2 at $2.5 \times 10^{-15} \text{ erg cm}^{-2} \text{ s}^{-1}$ (Figure 1 in Paper I) with this flux correction factor, and extrapolating the $\log N - \log S$ for X-ray-detected BL Lacs from Figure 5 of Henry et al. (2001) ($\alpha \sim 0.7$), we expect between 0.5 and 1 BL Lacs to appear in SEXSI. Increasing the $\log N - \log S$ slope by 0.1 (well within the uncertainties) more than doubles this number. Furthermore, if we use the radio number counts for BL Lacs at 1.0 mJy from Figure 5 of Giommi et al. (1999), we would also expect roughly one source in our survey area (although, again, the extrapolation required is nearly two orders of magnitude in radio flux density). Note that while the extreme, high-energy-peaked BL Lacs discussed in Giommi et al. (1999) make up only $\sim 2\%$ of this expected radio population, the fact that our survey goes nearly three orders of magnitude deeper in X-ray flux means that essentially all of the radio-selected objects should be detected.

Using large-area, public radio surveys we checked for radio emission from our 39 sources that exhibit line-free spectra. FIRST (15) and NVSS (24) radio images were examined for each of these sources; no sources were detected in the FIRST images to a 3σ limit of 0.75 mJy . Of the NVSS images, 19 had upper limits of $\sim 1.4 \text{ mJy}$, while three were

in a single noisy field with upper limits closer to 5 mJy. One source (J125306.0-091316) is within the contours of an extended NVSS source, but the low resolution of that survey ($\sim 50''$) makes it difficult to establish an association. The final source, J022215.0+422341, has a 2.8 mJy NVSS source within $10''$ (1.5σ), and may represent the expected ~ 1 radio-loud BL Lac source in our survey area. This general lack of radio counterparts leads us to conclude that most of these 39 line-free SEXSI sources are not BL Lacs.

7.5.2. ELGs in the redshift desert?

Since it is highly likely that the majority of these line-free objects are not BL Lacs, what are they? In Figure 15, we examine the notion that these objects are predominantly ELGs in which the [O II] $\lambda 3727$ line has slipped beyond the wavelength coverage of our spectra. We estimate a redshift for each continuum-only source by assuming that [O II] $\lambda 3727$ falls just longward of the optical spectral range for each source. Six of the objects have spectra with limited wavelength coverage, and could fall within the redshift distribution of the other ELGs at $z < 1.5$; the remaining 34 objects would have to be at higher redshifts (see lower left panel of Figure 15).

As would be expected if their mean redshift is higher, their magnitude distribution is shifted toward fainter values: 85% are fainter than $R = 22$ while only 57% of the ELGs are this faint (comparing only sources with $R_{\text{limit}} > 22$). The median R -magnitude for the ELG is 22.2, while for the continuum-only sources, $R_{\text{median}} > 23$ – the measurement is limited by our imaging depths. The f_x distributions of the two samples are statistically indistinguishable, while the HR distribution of the lineless objects is slightly softer, consistent with the fact that we can more easily detect unobscured objects at higher redshift. The values of L_x derived using the estimated redshifts are consistent with the rest of the ELG distribution, although, again, since the sources are by definition at higher redshift but have similar 2 – 10 keV fluxes, the median value of L_x is higher (see lower panel in Figure 15). We determine that these continuum-only sources are *consistent* with being the high-redshift end of the ELG population.

Teister et al. (2004) combine X-ray luminosity functions with spectral energy distributions of AGN to model the X-ray and optical distributions of X-ray sources from the GOODS survey and find that the predicted distribution for $R < 24$ sources is consistent with the GOODS spectroscopically-identified redshift distribution. The sources that remain spectroscopically unidentified are predicted to be either optically faint, obscured sources nearby or in the redshift desert, consistent with our notion that the SEXSI line-free sources are part of the redshift-desert ELG population.

The population statistics of the SEXSI sample change if we include these 39 line-free spectra with the ELG sample: $44.8\% \pm 3.1\%$ BLAGN, $42.7\% \pm 3.0\%$ ELG, $6.9\% \pm 1.2\%$ NLAGN, and $1.7\% \pm 0.6\%$ ALG. Adopting this assumption, the BLAGN and ELG fractions are the same within 1σ , at ~ 43 –44% each.

7.6. Stars

Of the 969 X-ray sources covered by our optical images, seven are associated with bright ($8.5 < R < 14$) stars, all of which were previously detected by ROSAT (although several are apparently identified here for the first time); these seven sources are labeled as ‘star’ in Table 2. All have colors of spectral types G to M and hardness ratios at the softest end of the distribution ($-0.73 < HR < -0.95$); six out of seven

have hard-band X-ray-to-optical flux ratios in the range $10^{-2.5}$ to 10^{-4} , typical of the upper end of the stellar L_x/L_o distribution (cf. Pizzolato et al. 2003; Feigelson et al. 2004). The seventh source has $\log(f_x/f_o) \sim -1.8$ which is extraordinarily high; however, since it is one of the five brightest sources in our entire survey, the identification with a 12^{th} magnitude star is likely correct. The very small fraction of stars ($< 1\%$) we detect is simply a consequence of our hard-band selection criterion.

Of the 468 spectra we obtained for the fainter optical counterparts, an additional eleven objects have stellar spectra at zero redshift. One of these is a 20^{th} magnitude object with strong H and He emission lines superposed on TiO bands, characteristic of a cataclysmic variable. The spectrum for this source is shown in Figure 16. The observed velocity is -274 km s^{-1} marking it as a candidate for a rare halo CV, although the high velocity may simply mean the system was at an extremum in orbital phase at the time of our observation. The remaining stellar objects are likely to all be chance coincidences. Five are fainter than 20^{th} magnitude, have hardness ratios $HR > -0.5$, and have $\log(f_x/f_o) > -0.3$, e.g., values quite atypical of stellar X-ray sources. In order to eliminate the possibility that a giant hard X-ray flare was responsible for the detected source, we examined the light curves for all five sources and found no evidence of dramatic variability. We calculated the probability of chance coincidence for each source using stellar and X-ray number counts and error radii for each field, and found that all had probabilities $\gtrsim 10\%$; in a survey with 27 fields, all are comfortably consistent with being chance alignments of a foreground star with a faint background source that is the true origin of the X-ray emission.

The remaining five stellar spectra are for counterparts with magnitudes $16.7 < R < 18$. CXOSEXSI J152151.6+074651, the softest of the five stars, showed evidence of variability, with a rapidly declining count rate in the first 5% of the observation. Two of the others lie outside the formal error circles (see Table 3), making it likely they are chance coincidences. The remaining two sources have extreme $\log(f_x/f_o)$ values (> -1 , using a hard-band f_x) and $HR > -0.3$; it is unlikely that these stars are the true counterparts.

8. SELECTION EFFECTS AND SAMPLE COMPLETION

Like all surveys with *Chandra*, the steep rolloff in effective area above $\sim 5 \text{ keV}$ limits the range of column densities that can be probed by SEXSI. Our sample includes only sources detected in the 2 – 7 keV band, limiting our ability to identify sources with $\log N_H \gtrsim 23.4$ at $z \lesssim 1$. In addition, we become less able to constrain N_H for high-redshift sources, where the absorption cutoff for typical columns shifts out of the soft band (to $E \lesssim 0.3 \text{ keV}$). For a $z = 2$ source this happens for columns $N_H \lesssim 10^{22} \text{ cm}^{-2}$. This effect can be seen in Figure 14, which shows the hardness ratio distribution in different redshift bins. In the highest bin ($z > 2$), the hardness ratios tend towards -0.5 . Figure 17 shows N_H versus z and illustrates the inability to constrain well the N_H measurement of high- z , low-column density sources.

Compared to some ‘hard-selected’ surveys, we are somewhat biased against steep-spectrum X-ray sources. We have focused our followup effort on sources with independent hard-band detections. By comparison, some surveys compile source lists by searching full-band images and then count a source as a hard-detection if it has positive counts in the hard-band image (e.g., Stern et al. 2002b; Yang et al. 2004); this will happen $\sim 50\%$ of the time due to statistical fluc-

tuations in the background when no hard-band counts are recorded. These catalogs will therefore include a higher fraction of steep-spectrum sources.

Completeness at our followup magnitude limits varies with source class and redshift range. The procedures we use to classify sources depend on specific lines, so that the redshift and R magnitude ranges over which we can properly identify sources depend on the source type. BLAGN are relatively easy to identify even at our typical followup limit of $R = 23 - 24$, since their broad lines constitute a significant fraction of the total R band luminosity. NLAGN, ELG, and ALG are all more challenging to identify at the faint end, since their typical line-to-continuum ratios are smaller. The ELG, which are identified only from nebular lines such as [O II] $\lambda 3727$, [O III] $\lambda 5007$, etc., have a large “redshift desert” from $z \sim 1.4 - 2.2$, where the [O II] $\lambda 3727$ has shifted into the IR and Ly α has yet to shift into the optical from the UV. Our 39 sources with continuum-only emission have X-ray and optical properties consistent with the notion that they are ELG in the redshift desert (§ 7.5.2). For most ELG, the optical counterparts are roughly consistent with L^* host galaxies and thus their R -band magnitude increases predictably with redshift (see § 10.2), unlike BLAGN, for example, where the optical luminosity is dominated by AGN emission and thus R is related to L_x . Thus, there are likely many more ELGs at higher redshifts that we have not spectroscopically followed up due to faint R -band counterparts; the ELG we do identify at $z \gtrsim 1$ typically have little continuum emission.

Since we use two different instruments for spectroscopy, we have investigated the extent to which their different quantum efficiencies as a function of wavelength may have affected source identification. The blue arm of LRIS (LRIS-B) has good sensitivity further into the near-UV than does the blue side of DEIMOS. There was one case where we had both a DEIMOS spectrum and an LRIS spectrum of a source which suggested different classifications: the DEIMOS spectrum showed only ELG lines, while the LRIS spectrum had a broad Mg II $\lambda 2800$ line on the blue side which led to the final classification as a BLAGN. This seems to be an isolated case in our sample, although there are few sources for which we have both LRIS and DEIMOS coverage.

We checked the statistics of the sources we identified with these two instruments, ignoring the Doublespec data from the Palomar 200 inch (5 m) since it only comprises 2% of the sample and includes only bright sources. We find no significant difference in classification statistics between the 137 sources classified by DEIMOS and the 280 sources classified by LRIS. With DEIMOS, we find $48.9 \pm 6.0\%$ (67) BLAGN while in the LRIS spectra, $48.2 \pm 4.1\%$ (135) are BLAGN; DEIMOS and LRIS identify $40.1 \pm 5.4\%$ (55 sources) and $37.5 \pm 3.7\%$ (105) ELGs, respectively. Both instruments classify a small number of targets as ALG (both $< 2\%$), and find a small number of stars ($\sim 3 - 5\%$).

The only marginal difference we find is in the rate of identifying NLAGN. Using LRIS, we identify 26/280 such sources ($9.3 \pm 1.8\%$), while with DEIMOS we find only 6/137 sources ($4.4 \pm 1.8\%$). The NLAGN DEIMOS may be missing would be classified as ELG. This difference probably results from the superior LRIS-B sensitivity, which allows faint, narrow, high-ionization UV-lines such as C III] $\lambda 1909$ or C IV $\lambda 1549$ to be detected at observed wavelengths below $\simeq 5000$ Å enabling LRIS to properly identify NLAGN in the redshift range $1 \lesssim z \lesssim 2$. Also, the [Ne V] $\lambda 3426$ line does not shift

into the band covered by DEIMOS until $z \sim 0.3 - 0.4$ and, as a consequence, we should also expect more low- z NLAGN with LRIS. These trends are seen in the data – of the six NLAGN identified with DEIMOS, only one has $1 < z < 2$, a source identified by its [Ne V] $\lambda 3426$ line at $z = 1.28$. There are no DEIMOS-identified NLAGN below $z = 0.8$ and half of the sources are found at $z > 2$. LRIS, on the other hand, identifies eight (31% of its) NLAGN at $1 < z < 2$ and another eight at $z \lesssim 0.5$.

Figure 18 gives an indication of our spectroscopic completeness (defined as the fraction of spectroscopically-identified sources as compared to the number of 2 – 10 keV SEXSI sources) as a function of several quantities: 2 – 10 keV flux, R -magnitude, $\log(f_x/f_o)$, and HR . *Chandra* targets that were eliminated from the X-ray catalog (e.g., nearby galaxies, quasars, extended target cluster emission – see Paper I) are not considered SEXSI sources, while X-ray point sources near target clusters are included in the catalog. To best illustrate the selection effects, separate from incompleteness due to lack of follow-up, we plot data only from the seventeen fields where we have a substantial fraction of spectroscopically-identified sources (see Table 1). All fields were included in this subset if they had 50% completeness; we added six fields that have $< 50\%$ completeness when a high fraction of $R < 24$ sources are identified. When considering only photometrically identified $R < 24$ sources the fraction of spectroscopically-identified sources ranges from 67% to 100%. These $R < 24$ completeness numbers depend on the particular R_{limit} of each field since some imaging does not reach $R = 24$ (see Paper II). These seventeen fields contain 725 2 – 10 keV SEXSI sources and 375 (52%) spectroscopically identified sources (86% of all spectroscopic ID’s presented in this article). The fields contain 445 photometrically identified $R < 24$ counterparts (84% of the photometrically identified $R < 24$ sources in these fields have spectroscopic ID’s). Figure 18 shows histograms of all 725 X-ray sources from these fields (open histogram), sources with optical spectroscopic z and class (shaded black), and sources with optical follow-up but continuum only – no z or class (shaded gray). The hatched histogram shows sources with $R > R_{\text{limit}}$.

The first plot of Figure 18 shows that the spectroscopic completeness in 2 – 10 keV flux is relatively even, 45% – 70% complete for $10^{-13.5} < f_{2-10 \text{ keV}} < 10^{-15} \text{ erg cm}^{-2} \text{ s}^{-1}$, where the majority of the sources lie. The last plot shows that the distribution of spectroscopic identifications in HR is $\sim 40\% - 65\%$ for the majority of sources, with 80% – 100% identification rates for the softest bins. The middle two plots show that, as expected, the fraction classified decreases towards fainter R -magnitudes, from 80% near $19 \lesssim R \lesssim 22$, to $\sim 30\%$ at $23 < R < 24$ (note that this bin has the highest number of sources). The third plot illustrates the distribution in $\log(f_x/f_o)$. The identification rate again is near 80% for low $\log(f_x/f_o)$ and then falls to $< 40\%$ for $\log(f_x/f_o) > 0.5$, which is expected due to the difficulty identifying sources at faint optical fluxes.

Figure 14 shows scatter plots of HR versus R -magnitude for five redshift bins. As discussed above, the average HR becomes smaller as redshift increases since at higher redshift the HR is less sensitive to changes in N_H . The first three boxes ($z < 1.5$) contain the majority of the open circles (non-BL sources) due to the large ELG population. The correlation between ELG R -magnitude and z is apparent – for $z < 0.5$ the majority of non-BL sources are spread from $16 \lesssim R \lesssim 22$, while for $0.5 < z < 1$ the spread shifts to $20 \lesssim R \lesssim 24$, and

for $1 < z < 1.5$ the sources are almost all found at $R > 22$. The non-BL sources at $z > 1.5$ (all NLAGN) on average have $R > 22$. The BLAGN (filled circles) lie predominantly at low HR s with a spread in R -magnitude; some are optically bright even at high- z (typical of unobscured quasars/AGN).

9. GLOBAL CHARACTERISTICS OF THE SAMPLE AND COMPARISON WITH OTHER SURVEYS

9.1. Redshift Distribution

The SEXSI sample confirms several of the basic conclusions of other survey work. First, as can be seen in Figure 1, very few low-redshift AGN have high rest-frame X-ray luminosities. Only 22/203 (11%) of sources with $z < 1$, and 1/65 (1.5%) with $z < 0.5$ have unobscured $L_x \geq 10^{44}$ erg s $^{-1}$. The difference in survey volume cannot alone explain this trend. Of the high-luminosity $z < 1$ sources, the majority (65%) are BLAGN. Even accounting for the smaller volume surveyed at low-redshift, if the X-ray to bolometric luminosity of this sample is typical of AGN (if there is not an uncharacteristically high fraction of the accretion luminosity emitted at longer wavelengths), then this reflects a dearth of high-mass, high-accretion-rate sources at low redshift. This was hinted at in the deep surveys (Barger et al. 2001), albeit from small survey volumes. Steffen et al. (2004) found this effect in the 0.4 deg 2 CLASXS survey, and we confirm it here with SEXSI, which samples the high-luminosity, low- z population with a high degree of completeness over ~ 2 deg 2 .

Figure 19 shows the source redshift distributions found by SEXSI, ChaMP (Silverman et al. 2005), CLASXS (Steffen et al. 2004), CYDER (Treister et al. 2005), and HELAS2XMM (Fiore et al. 2003). Broad-lined AGN are shown by filled histograms, while non-broad-lined sources are left unshaded. To provide the best comparison to our sample of hard-band-selected sources, we have eliminated sources from CLASXS and CYDER which have significant soft or broad-band detections, but where the hard flux is determined from a small number of counts ($S/N < 2$), and should therefore be considered an upper limit. To obtain similar hard-band detection significance to SEXSI, we impose a cut at $f_{2-10 \text{ keV}} < 2 \times 10^{-15}$ erg cm $^{-2}$ s $^{-1}$, removing approximately 50 sources from the CLASXS sample. CLASXS reaches a similar magnitude limit for spectroscopy as SEXSI. We adopt the ChaMP hard sample from Silverman et al. (2005) that includes *Chandra* sources selected to have $S/N > 2$ in the 2.5 – 8 keV band. ChaMP obtained optical spectroscopic classifications for 44% (220 sources) of their sample of 497 hard-band *Chandra* sources, primarily for sources with counterparts having $R < 22$.

All the surveys demonstrate that the BLAGN population peaks at higher redshift than the sample as a whole. NLAGN and ELG peak at $z < 1$ in all samples, and show rapid evolution up to $z \sim 0.7$. It should be noted that for $z \gtrsim 1$, incompleteness due to the faintness of optical counterparts is a significant factor, so the decline in source density above this redshift is likely an artifact of the spectroscopic survey depth. As can be seen from the second panel of Figure 14, almost all SEXSI non-BLAGN sources above $z = 1$ have $20 < R < 24$, with half above $R = 22$, so that our survey limit of $R = 23 - 24$ implies we are increasingly incomplete above this redshift. ChaMP's shallower spectroscopic magnitude cutoff ($R \lesssim 22$) results in the sharper redshift cutoff of the ChaMP non-BLAGN population compared to SEXSI (ChaMP finds no non-BLAGN above $z = 0.8$, whereas the SEXSI NLAGN spread to above $z = 3$ and ELG/ALG to $z \approx 1.5$). SEXSI,

CYDER and CLASXS, with similar survey depths for spectroscopy, find similar redshift distributions.

The ChaMP BLAGN z -distribution is broader and flatter than that of SEXSI, with a larger fraction of broad-lined sources at $z > 2$. Again, this is largely a result of selection effects. The ChaMP X-ray source population is on average softer than ours, due to the fact that they select sources from full-band images and include any source with a hard-band $S/N \geq 2$. Combined with the predominance of BLAGN in the $z > 1$, $R < 21$ sample (see Figure 7), this results in a larger relative fraction of BLAGN.

In addition, we note that ChaMP finds a significantly larger fraction of ALG (7%). This is simply a matter of nomenclature. They classify as ALG sources with absorption lines and a D4000 break whether or not they exhibit weak emission lines. Our ALG are strictly sources in which only absorption features are detected. Since 50% of our 168 ELG do show absorption features, our sample would contain *more* ALG than ChaMP if we adopted their definition; our greater ability to detect weak lines explains any discrepancy.

9.2. Obscured Sources

To explore the fraction of obscured sources, we split our sample at $\log N_H = 22$. Figure 20 shows the fraction of obscured sources ($\log N_H > 22$) as a function of *unobscured* 2 – 10 keV flux (fluxes corrected for intrinsic N_H obscuration) for spectroscopically identified sources from SEXSI (filled circles), GOODS CDFN (triangles; E. Treister, private communication), and ChaMP (diamonds; Silverman et al. 2005). The datapoints are calculated using the survey catalogs, binned into flux ranges shown by the vertical dashed lines at the bottom of the plot. Each SEXSI, ChaMP, and GOODS CDFN datapoint is offset slightly along the x-axis for clarity and the number of sources in each bin is indicated at the bottom.

Both SEXSI and ChaMP N_H values are calculated using X-ray spectral fitting, which also provides individual (asymmetric) errors for each column density. We would like to calculate a fraction of obscured sources and its associated error taking into account both the individual N_H errors from the spectral fits and Poisson counting statistics. To calculate the fraction of obscured sources for each flux bin we first generate, for each individual source in that flux bin, a Monte Carlo distribution of 1000 N_H values. To account for the asymmetric error bars provided by the spectral fitting, we generate two Gaussian distributions, one with a standard deviation equal to σ^+ and one with a standard deviation equal to σ^- . The two distributions are then patched together to make a single, asymmetric Gaussian distribution. ChaMP reports 90% confidence error bars instead of 1σ , as SEXSI does, so we estimate that the ChaMP σ is equal to $1/1.65$ times the 90% confidence limit. Because the purpose of this exercise is to calculate a fraction of sources above and below $\log N_H = 22$, we do not need to take into account N_H values in these distributions that, for example, fall below 0 or are otherwise unphysical. By construction, each distribution has 500 N_H values above and below the best-fit value.

We then use the Monte Carlo N_H values to calculate the mean and standard deviation of obscured fractions ($\log N_H > 22$) in each flux bin. These are plotted in Figures 20 and 21. The plotted error bars are the 1σ errors that result from adding the standard deviation described above in quadrature with Poisson counting error ($\frac{\sqrt{N}}{N}$, where N is the number of sources in each bin). For many sources, the column density

and associated errors constrain the source to lie either solidly above or below $\log N_H = 22$; thus the individual N_H errors contribute negligibly to the uncertainty in the fraction of obscured sources; the errors from the Poisson counting statistics strongly dominate the overall error bars.

The GOODS CDFN sources are calculated from hardness ratios and thus do not have similar errors from the fits. For these sources we simply calculate a fraction of obscured sources by counting the number with $\log N_H > 22$ in each bin and dividing by the number of sources in that bin. The errors presented are solely from Poisson counting statistics, which provide an adequate comparison since the counting errors dominate in the SEXSI and ChaMP calculation.

In Figure 20 the SEXSI data shows an obscured fraction consistent with ~ 0.5 for all flux ranges, with a marginally significant decrease with increasing flux. In the second through fourth bins, which include sources from $3 \times 10^{-15} - 3 \times 10^{-14} \text{ erg cm}^{-2} \text{ s}^{-1}$, the range over which the $2 - 10 \text{ keV } \log N - \log S$ changes slope, there are 314 SEXSI sources, providing a tight constraint on the obscured fraction. All three of these fractions fall between 0.5 and 0.6.

The GOODS CDFN data shows a higher fraction of obscured sources, though most of the flux bins contain few sources (since the majority of GOODS sources fall below our flux limit) and thus have large errors. Since GOODS uses hardness ratios to calculate their N_H values we explored the difference between the SEXSI N_H values when calculated as described using the XSPEC fits, and when using the *HR*. Both methods are described in more detail in § 5. Figure 21 shows the fraction of obscured SEXSI sources calculated using absorbed (observed) $2 - 10 \text{ keV}$ fluxes. The black filled circles are calculated using the method described above, with the N_H values from the spectral fits. The lighter gray points show the fraction of obscured sources when we use N_H values calculated from *HR*'s. There is an obvious difference: the *HR*-calculated fractions of obscured sources are consistently higher, across the entire flux range. In the bin from $\sim 3 \times 10^{-15} - 1 \times 10^{-14} \text{ erg cm}^{-2} \text{ s}^{-1}$, where we have 149 sources, the two values are not even consistent to within 1σ . This discrepancy arises mainly from sources with the lowest column densities. For sources with a significant ($\gtrsim 5 \times 10^{21} \text{ cm}^{-2}$) column density from the X-ray spectral fit, the N_H values from the two methods are typically consistent within errors. The large discrepancy arises from sources where the XSPEC fit finds no significant obscuration ('<' in the catalog), though the $1 \sigma^+$ high value does include significant obscuration (even $\log N_H > 22$) in some cases — see Figure 17. For such sources, the *HR*-calculated value is often $> 10^{22} \text{ cm}^{-2}$. This difference seems to result from details of the calculation. For example, a source with many counts near 0.3 keV will affect the XSPEC fit differently than the *HR*-based N_H calculation. To calculate *HR*, as described in more detail in Paper I, we extract counts from $0.3 - 2.1 \text{ keV}$ and from $2.1 - 7 \text{ keV}$ and transform each value using the appropriate exposure map into the standard band ($0.5 - 2 \text{ keV}$ and $2 - 10 \text{ keV}$) fluxes. Our exposure maps correction assumes $\Gamma = 1.5$. We then use these fluxes to calculate the N_H values. Thus, a source with many counts near 0.3 keV but fewer at 2 keV will result in an increased flux for the entire $0.5 - 2 \text{ keV}$ band, while in the X-ray spectral fit we know that those counts are actually at 0.3 keV . The *HR* based N_H values will have large individual errors, and these are not taken into account on the plots. Thus, the discrepancy of the fraction of obscured sources in Figure 20 is not wholly unexpected.

The ChaMP data show consistently smaller fractions of obscured sources in all flux ranges, although the discrepancy is highly significant only for the flux bin from $\sim 3 \times 10^{-15} - 1 \times 10^{-14} \text{ erg cm}^{-2} \text{ s}^{-1}$. The lower obscured fractions in ChaMP results from the predominance of BLAGN, which, as described above, arises from the brighter magnitude limit of their spectroscopic followup. As a population, the BLAGN have lower obscuration than the NLAGN and ELG. This selection effect is illustrated in Figures 8 and 13. From our sample, 79% of BLAGN have $R < 22$ and 52% have $R < 21$. Combining these with the N_H histogram split by source type, one can see that a brighter optical spectroscopic followup limit will cause an N_H distribution with fewer obscured sources. Not only will there be more BLAGN compared to other source types, but of the BLAGN found, a higher fraction are unobscured sources brighter in R .

Figure 22 shows the fraction of obscured sources as a function of unobscured luminosity for sources with spectroscopic redshifts. The luminosities are calculated using unobscured fluxes and the calculation of each fraction and associated error are determined as described for Figure 20. The SEXSI sample (filled circles) shows a constant fraction of obscured sources of ~ 0.5 . The difference with ChaMP can once again be explained by the difference in spectroscopic followup depth. SEXSI's most obscured sources tend to be NLAGN and ELG (see Figure 12).

Of the total sample of NLAGN, 26/32 (81%) are obscured ($N_H > 10^{22} \text{ cm}^{-2}$) and of those with the highest luminosities ($L_x > 10^{44} \text{ erg s}^{-1}$) all fifteen (100%) are obscured. Of the more numerous ELG, 119/162 (73% \pm 7%) are obscured. For the quasar-luminosity ELG, 11/13 (85%) are obscured. These numbers are both consistent with the obscured fraction of NLAGN. These sources make up about half of the total SEXSI AGN sample, and thus they contribute heavily to the obscured fractions seen in Figure 22. They have median magnitudes of $R \gtrsim 22$; following up brighter sources only misses most of these low-luminosity, obscured AGN.

9.3. Obscured Sources with Quasar Luminosities

According to unified AGN models (Antonucci 1993), hard X-ray surveys should find significant numbers of type-2 quasars (e.g., quasars viewed edge-on, through significant amounts of absorbing material). These will be identified as X-ray sources with large N_H , $L_x \gtrsim 10^{44} \text{ erg s}^{-1}$, and with narrow-lined optical counterparts. Confirming candidate type-2 quasars is, however, difficult. The two *Chandra* deep fields have found fourteen narrow-lined sources with quasar X-ray luminosities (Norman et al. 2002; Barger et al. 2003; Dawson et al. 2003; Szokoly et al. 2004). Of these, only Dawson et al. (2003) has published an infrared spectrum confirming that lines, such as $H\alpha$, that are redshifted out of the optical, are narrow.

In the SEXSI survey we find 17 sources with *unobscured* rest-frame luminosities above $10^{44} \text{ erg s}^{-1}$ which we classify as NLAGN, and 16 which we classify as ELG. Of these 33 sources, 32 (97%) have $N_H > 10^{22} \text{ cm}^{-2}$. Nine of these, all NLAGN, have $z > 2$. This $z > 2$ type-2 quasar density is roughly consistent with the $1 - 2$ type-2 quasars per deep *Chandra* field predicted by Stern et al. (2002b), although it is unlikely that all of our candidates are true type-2 quasars (e.g., see Halpern et al. 1999; Stern et al. 2002a). We note that by comparison to our 33 narrow-lined quasars, ChaMP find no luminous, narrow-lined quasars. This difference is mainly attributable to their shallower spectroscopic coverage. Of our

narrow-lined quasars, only five have $21 < R < 22$ while the rest have $R > 22$ – and, in fact, most NLAGN quasars have $R > 23$.

10. THE NATURE OF THE EMISSION-LINE GALAXIES

SEXSI has identified a substantial population of X-ray luminous ($10^{41} - 10^{44}$ erg s $^{-1}$) sources with optical spectra lacking both high-ionization lines and evidence for a non-stellar continuum. Such sources, with typical redshifts $z < 1$, are found in most *Chandra* and *XMM* surveys, in particular in the deep fields (see Brandt & Hasinger 2005, and references therein). The nature of this population is somewhat uncertain. Moran et al. (2002) suggest that most are akin to Seyfert galaxies where dilution by the host-galaxy light hinders detection of the high-ionization lines. In some cases, these high-ionization lines may also be weak due to partial obscuration. Some ELG, however, have optical spectra of high signal-to-noise, implying the AGN signatures are extremely weak or absent (Comastri et al. 2002). A number of suggestions as to the nature of these sources have been made. At the low-luminosity end of the distribution, some may be powered by starburst activity; Yuan & Narayan (2004) suggest that some may be AGN with radiatively inefficient accretion flows. Alternatively, they may be AGN that are entirely obscured (over 4π sr) so that ionizing photons cannot escape the nuclear region (Matt 2002). A few may also be BL Lac objects (Brusa et al. 2003).

In this section we discuss constraints that we can place on the SEXSI sample of ELG.

10.1. Low-luminosity ELG; Powered by Star Formation?

Starburst galaxies exhibit low-ionization, narrow emission lines and produce significant hard X-ray fluxes, and so must be considered as potential contributors to the low-luminosity end of our ELG population. Their X-ray emission arises from a combination of hot gas heated in supernova remnant shocks and the population of high-mass X-ray binaries whose compact components are produced in these supernovae. Starburst galaxy radio emission is predominantly synchrotron emission from cosmic rays accelerated in these same remnants; since the galaxy residence time for the cosmic rays is comparable to the lifetime of the X-ray binary population, the X-ray and radio luminosities are correlated (Ranalli et al. 2003). The most luminous local starburst is NGC 3256; detailed spectral analysis by Moran et al. (1999) of this galaxy showed that it has a 2 – 10 keV X-ray luminosity of 2.5×10^{41} erg s $^{-1}$, produced by a star formation rate of $\sim 40 M_{\odot}$ yr $^{-1}$. Helfand & Moran (2001) use the radio source $\log N - \log S$ relation in conjunction with the specific X-ray luminosity per O-star and the ratio of radio to X-ray luminosities in starbursts to predict a surface density for 2 – 10 keV X-ray sources attributable to starburst galaxies of 2.2 deg $^{-2}$ at the SEXSI flux threshold of 2×10^{-15} erg cm $^{-2}$ s $^{-1}$.

More recent work by Ranalli et al. (2003), Grimm et al. (2003), and Gilfanov et al. (2004) explicitly use 2 – 10 keV luminosity as a star-formation rate indicator and reach similar conclusions. With a total sample of 37 local star-forming galaxies, NGC 3256 remains the most luminous, although two of six candidate star-forming galaxies selected by Ranalli et al. (2003) from the *Chandra/Hubble* Deep Field have inferred luminosities of $\sim 3 \times 10^{42}$ erg s $^{-1}$, implying star for-

mation rates of several hundred solar masses per year. These authors predict higher surface densities of $10 - 20$ deg $^{-2}$ at 2×10^{-15} erg cm $^{-2}$ s $^{-1}$ and $1 - 2.5$ deg $^{-2}$ at 1×10^{-14} erg cm $^{-2}$ s $^{-1}$. Folding these higher predicted densities with our areal coverage curve from Paper I predicts that we should have 1–3 such objects in our 2 deg 2 sample of hard X-ray sources.

A total of 11 ELGs in our sample have hard X-ray luminosities $L_x < 10^{42}$ erg s $^{-1}$, and another 11 have $10^{42} < L_x < 10^{42.5}$ erg s $^{-1}$ (this upper limit would imply a star formation rate of $\sim 600 M_{\odot}$ yr $^{-1}$ according to the Ranalli et al. (2003) calibration). We examined radio images for all 22 galaxies from the FIRST (Becker et al. 1995) and NVSS (Condon et al. 1998) surveys. Of the 17 sources that fell within the FIRST survey limits, 15 have upper limits of $f_{20\text{ cm}} < 0.75$ mJy and one (in a slightly noisy field) has a limit of ~ 1 mJy. The final source, J170423.0+514321, is coincident with a bright (17 mJy) barely resolved double (or core-jet) source, clearly marking it as an AGN. For the five sources appearing only in the NVSS, four have upper limits of 1.5 – 2 mJy, while the fifth, J030532.6+034301, is coincident with a subthreshold source with a flux density of a little over 2 mJy (although a slight positional offset suggests the possibility of a chance coincidence).

When plotted on the $L_x - L_r$ correlation plot of Ranalli et al. (2003), both the two possible detections described above and the upper limits place galaxies factors of 3 – 10 above the correlation (i.e., they are too X-ray bright for their radio luminosities – or upper limits thereon – to be starburst galaxies). A few of the ELG with $L_x > 10^{42.5}$ erg s $^{-1}$ are also coincident with weak radio sources. However, their X-ray luminosities fall more than an order of magnitude above the Ranalli et al. (2003) L_x/L_r correlation for starbursts. Thus, consistent with the expectations of the starburst surface density described above, we conclude that few if any of the ELGs in our sample have X-ray luminosities dominated by star formation – essentially all must be powered by accretion.

10.2. Non-Stellar Emission

The hypothesis that ELG are dominated in the optical by galaxy light rather than non-stellar emission can be tested to some degree by plotting $\log(f_x/f_o)$ as a function of $\log(L_{2-10\text{ keV}})$ (Fiore et al. 2003). Figure 23 shows this for BLAGN (top panel), and sources which lack broad emission lines (bottom panel) for the SEXSI sample, together with sources from HELLAS2XMM and CDFN. The BLAGN, clearly dominated by accretion luminosity, are clustered at high luminosity, whereas the non-BLAGN sources show a correlation between $\log(f_x/f_o)$ and $\log(L_{2-10\text{ keV}})$. Fiore et al. (2003) argue that the correlation between the two quantities indicates that the optical light is largely dominated by $\sim L^*$ host galaxy light in the non-broad-lined sources, approximately independent of AGN luminosity. This is seen by the relatively small (one decade) scatter in optical flux seen over a large range (four decades) in X-ray flux. This correlation is due to a relationship in $R - z$ that is independent of L_x ; Figure 7, the $R - z$ plot, shows that the R -magnitude of the ELG (triangles) varies predictably with z (with some scatter). Bauer et al. (2004) show that this $\log(f_x/f_o) - L_x$ relationship does not hold for $R \gtrsim 24$, the optical brightness at which the $R - z$ track of Fiore et al. (2003) and simple galactic evolution tracks begin to differ noticeably.

Figure 24 plots the Fiore et al. (2003) correlation for NLAGN and ELG separately. The ELG generally fall on the best-fit line from Fiore et al. (2003), but the NLAGN

tend to fall below the line. This suggests that NLAGN have brighter X-ray-luminosity-normalized-optical magnitudes than do ELG. This would be consistent with NLAGN having a smaller fraction of their AGN optical emission obscured from view. Again, this result is not unexpected, as Figure 7 shows that NLAGN do not have the same $R-z$ relationship as ELG; instead many of the NLAGN have redshifts much higher than would be expected if their R -magnitude were simply dominated by L^* galaxy light. Figure 24 also suggests that searching only the highest $\log(f_x/f_o)$ sources for type 2 quasars, as suggested by Fiore et al. (2003), will miss some of the highest-luminosity NLAGN accessible via optical spectroscopy with current telescopes.

10.3. Search for Faint High-Ionization Lines

In this section we discuss difficulties in detecting weak high-ionization lines over the SEXSI redshift range, and investigate to what extent narrow-line AGN signatures may be present, but not detected in individual spectra. In addition, we ask if significant numbers of BLAGN could be identified as ELG due to host-galaxy dilution.

Dilution of AGN light by emission from the host galaxy, and the resulting difficulty in detecting weak high-ionization lines, is certainly an important factor in optically classifying the population of ELG. Moran et al. (2002) obtained wide-slit integrated spectra (including both the nuclear region and the galaxy) of well-studied, nearby Seyfert 2 galaxies to mimic observations of distant sources and found that eleven of eighteen galaxies would not be considered Seyfert 2's based on their integrated spectra: the nuclear emission lines had diminished flux compared to the stellar lines, so that the line-flux ratios (e.g., $[\text{N II}] \lambda 6583/\text{H}\alpha$, $[\text{O III}] \lambda 5007/\text{H}\beta$) were consistent with the values observed in H II regions or starburst galaxies, not with those of Seyfert 2's. These sources were all at low redshift, so that optical spectroscopy covers a different observed wavelength range than is the case for the large majority of our objects; these line-flux ratio diagnostics are not available for most of our sources.

SEXSI classifies ELG based on failure to detect broad or narrow high-ionization lines, rather than on quantitative line-flux ratio measurements. Here we explore the line-detection statistics as a qualitative indicator of line-flux ratios and source class diagnostic. The relatively broad redshift range and significant stellar continuum makes $\text{H}\beta$ difficult to detect; we identify it in only 21% of 113 ELG with appropriate wavelength coverage (Table 4). In two-thirds of the 103 lower- z ELG we do detect $[\text{O III}] \lambda 5007$. High $[\text{O III}] \lambda 5007/\text{H}\beta$ ratios are found in Sy2 spectra but also in H II region-like galaxy spectra; without another line ratio such as $[\text{N II}] \lambda 6583/\text{H}\alpha$ or $\text{S II } (\lambda 6716 + \lambda 6731)/\text{H}\alpha$ we are unable to securely classify the optical spectrum as a NLAGN. 151 ELG spectra include $[\text{Ne III}] \lambda 3869$ coverage, but only 6% show the emission line. Strong $[\text{Ne III}] \lambda 3869$ is also found in Sy2 spectra, but again multiple line-ratios are needed to secure the Sy2 classification. $[\text{Ne III}] \lambda 3869$ is a weaker line in Seyfert 2 spectra, and was shown to be easily erased by dilution by Moran et al. (2002); thus, the low detection rate of $[\text{Ne III}] \lambda 3869$ is not constraining.

The line that primarily allows us to identify a source as a NLAGN rather than an ELG over much of our redshift range is $[\text{Ne V}] \lambda 3426$. This line is redshifted into the optical window over the redshift range $0.1 \lesssim z \lesssim 1.8$, the range within which most of the ELG in our sample lie. The other typical high-ionization UV lines do not shift into the optical until

$z \sim 1.1$ ($\text{C III}] \lambda 1909$) and $z \sim 1.6$ ($\text{C IV } \lambda 1549$). Thus, it is detection of $[\text{Ne V}] \lambda 3426$, or the lack thereof, that most often places a source in the NLAGN or ELG subsample.

As shown in Table 4, 80% of the NLAGN with $[\text{Ne V}] \lambda 3426$ access have $[\text{Ne V}] \lambda 3426$, while only 20% of our BLAGN exhibit this line. The fraction of the NLAGN in which $[\text{Ne V}] \lambda 3426$ is present should be treated as an upper bound, since in the range $z < 1-2$ we cannot identify the source *unless* $[\text{Ne V}] \lambda 3426$ is present. Thus there are many instances where a NLAGN has no $[\text{Ne V}] \lambda 3426$ detection in its spectrum, consistent with the idea that $[\text{Ne V}] \lambda 3426$ may be hidden, and, due to wavelength coverage, a significant fraction of NLAGN will be classified as ELG since only $[\text{Ne V}] \lambda 3426$ is useful for making the distinction.

In contrast, we conclude that few BLAGN are classified as ELG due to finite wavelength coverage. 89% of our BLAGN with wavelength coverage of the $\text{Mg II } \lambda 2800$ line do show broad $\text{Mg II } \lambda 2800$ emission. $\text{Mg II } \lambda 2800$ shifts into the optical near $z \sim 0.4$, thus the $\text{Mg II } \lambda 2800$ line is accessible in the majority of the ELG spectra but broad emission is not detected. Since the $\text{Mg II } \lambda 2800$ detection rate is so high, we conclude that BLAGN are not easily misclassified as ELG, even at $z \lesssim 1$, when the broad, high-ionization lines farther in the UV (e.g., $\text{C III}] \lambda 1909$, $\text{C IV } \lambda 1549$) do not lie in our spectral range. A note of caution is in order, however; Glikman et al. (2004) have shown that dust-reddened quasars which exhibit only narrow lines in their optical spectra, can have broad Paschen lines in the near-IR.

Our basic conclusion is that many of the ELG may be classified as NLAGN in higher S/N spectra and/or with wider wavelength coverage, but that few are broad-lined sources we have misclassified. This conclusion is consistent with the N_H distribution of the ELG (85% of which have $N_H > 10^{22} \text{ cm}^{-2}$). To further test this hypothesis we have stacked a group of ELG optical spectra to increase the signal-to-noise, searching for $[\text{Ne V}] \lambda 3426$ emission that is the hallmark of NLAGN over much of our redshift range.

Figure 25 presents the spectrum created by stacking 21 ELG spectra obtained with LRIS on the Keck I Telescope. Sources from our March and June 2002 observations were used such that the spectra were obtained with the same spectrometer configuration. Of these spectra, we chose 21 sources with $0.7 < z < 1.2$. This redshift range ensures that the $[\text{Ne V}] \lambda 3426$ emission line will fall on LRIS-R from 5800–7500 Å (observed frame). The stacking procedure used standard stacking commands in IRAF. First each spectrum is shifted to its rest frame using `dopcor` and then these spectra are combined with `scombine` using median weighting. The weights of each spectrum were close to 0.05 as would be expected for equal weighting; no single individual bright spectrum dominated the stacked spectrum.

The stacked spectrum shows the features typical in individual ELG at these wavelengths: the strong $[\text{O II}] \lambda 3727$ emission line, the $\text{CaHK } \lambda\lambda 3934, 3968$ absorption lines and the D4000 continuum break. The stacked spectrum also shows additional absorption features such as $\text{H10 } \lambda 3798$, $\text{H9 } \lambda 3835$, and $\text{H}\zeta \lambda 3889$. $[\text{Ne III}] \lambda 3869$ emission, which is seen in only 6% of the ELG spectra, is well-detected in the stacked spectrum. Most importantly, however, is the detection of $[\text{Ne V}] \lambda 3426$. This emission is produced by highly-ionized Ne, confirming the presence of a strong AGN X-ray ionizing continuum and consistent with the idea that our ELG population contains a significant fraction of NLAGN.

11. SOURCES ASSOCIATED WITH TARGET AND NON-TARGET GALAXY CLUSTERS

Few cluster galaxies have been determined to have obvious AGN signatures; in this section we explore the population of spectroscopically-identified SEXSI AGN associated with known galaxy clusters. The pre-*Chandra* best estimate was that 1% of cluster galaxies host AGN (Dressler & Gunn 1983). This estimate came from laborious optical spectroscopic studies of galaxies. *Chandra*'s unprecedented angular resolution in the 2 – 10 keV band allows identification of X-ray emitting galaxies that appear in images near the cluster center. While some of these sources will be unassociated AGN, searching these sources for cluster-member AGN is much more efficient than searching in the optical for AGN signatures, since the optical source density is high compared to the X-ray source density; furthermore, as we have discussed throughout this paper, many of the X-ray sources assumed to be AGN from their high X-ray luminosities will have no obvious optical indication of nuclear activity.

Martini et al. (2002) obtained spectra of the optically-bright ($R < 20$) counterparts to 2 – 10 keV *Chandra* sources near A2104, a well studied $z = 0.154$ cluster, and found that at least 5% of the cluster galaxies (6 sources) had X-ray fluxes consistent with AGN activity, while only $\sim 1\%$ showed AGN activity in the optical in agreement with the earlier estimates derived via optical surveys. We explore this finding further here using our larger sample of cluster X-ray sources.

11.1. Target Clusters

Of the SEXSI fields, fifteen (56%) have galaxy clusters as targets. Three of these are nearby clusters ($z = 0.014 - 0.045$), two are at $0.18 < z < 0.22$, and the rest are at $z > 0.43$. In Paper I we flagged sources when they fell within 1 co-moving Mpc of the cluster center as projected on the sky. The area associated with this 1 Mpc radius region and the sources within the area (the flagged sources) were excluded from our $\log N - \log S$ calculation to avoid biasing our background sample. The SEXSI spectroscopic followup, however, establishes source redshifts, enabling the determination of cluster membership. Table 5 lists the SEXSI cluster fields and details the spectroscopic completeness among cluster-flagged sources and the spectroscopically identified X-ray emitting cluster members.

Of the three nearby clusters for which the 1 Mpc radius covered more than the entire *Chandra* field-of-view, we have spectra for 43 of the 103 sources, and none are at the cluster redshift. This result is likely a consequence our spectroscopic followup strategy which skipped the brightest sources (likely cluster members) to focus on background sources.

Of the twelve higher- z cluster fields, we have taken 41 spectra of sources that fall near the cluster in our image and have discovered that ten of the flagged sources are at the target cluster redshift (see Table 5). Of these ten, only three show high-ionization optical emission lines characteristic of active galaxies, although all ten have 2 – 10 keV luminosities of $L_x \gtrsim 10^{43}$ erg s $^{-1}$, suggesting an active nucleus. Of the ten confirmed members, the BLAGN have luminosities of $\log L_x = 43.3, 43.8,$ and 44.5 with obscuring column densities of $N_H < 10^{21.2}, 0,$ and $10^{21.5}$ cm $^{-2}$, respectively. The ELG have $42.9 < \log L_x < 44.0$ and $22.6 < \log N_H < 23.4$. The ALG has $\log L_x = 43.4$ and $\log N_H = 21.9$. All of the non-broad-lined sources are considered obscured ($\log N_H > 22$), save the ALG just below the $\log N_H = 22$ cutoff. In addition to the ten sources within 1 Mpc (projected), we identify three

additional sources at the target cluster redshift lying from 1 – 2 Mpc (projected) from the cluster center. These three sources are all ELG with $L_x > 10^{43}$ erg s $^{-1}$.

Of the thirteen sources listed in Table 5 within ~ 2 Mpc of the target clusters we find that only $23\% \pm 13\%$ are BLAGN (3 sources). One of these BLAGN has broad lines barely over our 2000 km s $^{-1}$ cut; this radio source, MG1 J04426+0202, was the target of the CL 0442+0202 *Chandra* exposure (see Stern et al. 2003); thus, we exclude this field from the analysis. We then find that only $17\% \pm 12\%$ (two of twelve sources) of the confirmed cluster AGN have broad lines. The target clusters for which we have identified member AGN have redshifts in the range $0.46 < z < 1.27$, where ELG's are still readily detectable. If we naively look at the SEXSI 2 – 10 keV source class statistics including only sources in that z range, we find $37\% \pm 4\%$ (82 sources) BLAGN and $52\% \pm 4\%$ (114 sources) ELG. Though our cluster member AGN sample is relatively small, they hint that the fraction of BLAGN is lower in cluster AGN than in the SEXSI background sample.

11.2. Non-Target Clusters Identified in Holden et al. (2002)

In addition to the thirteen target cluster member AGN we also report on two additional clusters from Holden et al. (2002); we have identified two cluster member AGN (ELG) in each cluster. The "Notes" column and associated footnotes of Table 5 references these serendipitous clusters, with redshift determinations from spectroscopic followup of our 2 – 10 keV sources. Appendix A of Holden et al. (2002) reports two new X-ray emitting groups or low-mass clusters of galaxies, discovered as extended sources, in SEXSI fields RX J0910 and RX J1317; their study included no optical spectroscopic followup. We have spectra of 2 – 10 keV SEXSI sources nearby these non-target clusters.

For SEXSI field RX J0910, we have identified two ELG at $z \simeq 1.1$, $\sim 2'$ from the position of CXOU_J091008.6+541856. The X-ray analysis of Holden et al. (2002) suggests two redshift possibilities due to a T, z degeneracy: $z = 0.68 \pm 0.06$ or $z = 1.18^{+0.08}_{-0.07}$. The two SEXSI ELG, CXOSEXSI_J090954.0+541752 and CXOSEXSI_J090955.5+541813, are at $z = 1.101$ and $z = 1.102$ and $2.4'$ and $2.0'$ away (projected 1.2 Mpc and 1.1 Mpc) from the position of CXOU_J091008.6+541856. These sources are 3.2 Mpc projected ($6.17'$) from the target-cluster of the field, RX J0910+5244 ($z = 1.11$). Our spectroscopic redshifts at $z \sim 1.1$ agree within 1σ of the higher- z prediction of Holden et al. (2002).

The other serendipitous cluster is in SEXSI field RX J1317, which had a target of cluster RX J1317+2911 ($z = 0.805$). The *Chandra* data analysis of CXOU_J131654.2+291415 by Holden et al. (2002) suggests a cluster with $T = 2.9^{+3.1}_{-2.1}$ keV and $z = 0.42^{+0.14}_{-0.10}$. We have identified two 2 – 10 keV sources that fall from $1.7' - 4.2'$ of the reported position and have redshifts around $z \sim 0.58$. The sources, CXOSEXSI_J131700.2+291307 and J131706.2+291058 at $z = 0.580$ and 0.579 , fall ~ 0.8 Mpc and 2.0 Mpc (projected) from the CXOU_J131654.2+291415, an indication of a cluster at $z \sim 0.58$. This redshift agrees within $\sim 1 \sigma$ of the prediction in Holden et al. (2002).

Including these four additional cluster AGN in our comparison of cluster member class statistics to those of the SEXSI background sample, we find a fraction of cluster BLAGN to be even lower: $12\% \pm 8\%$. This fraction again is calculated excluding SEXSI field CL 0442+0202. Comparing to

the SEXSI background sample from $0.46 < z < 1.27$ which contains $37\% \pm 4\%$ BLAGN, we find a stronger indication (albeit still short of 3σ) that the AGN cluster-member sample has fewer BLAGN than does the background sample.

12. SUMMARY

We have presented a sample of 477 spectra of 2 – 10 keV *Chandra* sources. Of our 438 spectroscopically-identified sources with counterpart magnitudes $R \lesssim 24$, we confirm with high significance a number of results found in other surveys. We find that few AGN at $z < 1$ have high rest-frame X-ray luminosities, reflecting a dearth of high-mass, high-accretion-rate sources at low redshift. In addition, our sample of broad-lined AGN peaks at significantly higher redshift ($z > 1$) than do sources we identify as emission-line galaxies. We find that 50% of our sources show significant obscuration, with $N_H > 10^{22} \text{ cm}^{-2}$, independent of intrinsic luminosity. We have identified nine narrow-lined AGN with $z > 2$ having quasar luminosities ($L_x > 10^{44} \text{ erg s}^{-1}$). This is consistent with predictions based on unified AGN models.

We have investigated in some detail the nature of the large sample of 168 sources which we classify as emission-line galaxies. These X-ray luminous objects (most with $L_x > 10^{42} \text{ erg s}^{-1}$) have optical spectra lacking both high-ionization lines and evidence for non-stellar continuum. We conclude that few of these sources, even at the low-luminosity end, can be powered by starburst activity. By stacking 21 spectra for sources in a similar redshift range in order to increase the signal-to-noise, we are able to identify [Ne V] $\lambda 3426$ emis-

sion, a clear signature of AGN activity. This demonstrates that the majority of these sources are Seyfert 2 galaxies, where the high-ionization lines are diluted by stellar emission and/or extinguished by dust.

We are grateful to Michael Cooper and Jeffrey Newman of UC Berkeley for their help with the DEIMOS data reduction pipeline. The analysis pipeline was developed at UC Berkeley with support from NSF grant AST-0071048. We thank Patrick Broos of Penn State for his generous help with *acis_extract* and Chandra Fellow Franz Bauer for a careful reading of the manuscript and many helpful suggestions. We also thank Ed Moran, Mark Davis, and Alison Coil for collaboration on the CL 0848+4454 spectroscopy. We wish to recognize and acknowledge the significant cultural role that the summit of Mauna Kea plays within the indigenous Hawaiian community. We are fortunate to have the opportunity to conduct observations from this mountain. In addition, this research has made use of NASA's Astrophysics Data System Abstract Service and the NASA/IPAC Extragalactic Database (NED) which is operated by the Jet Propulsion Laboratory, California Institute of Technology, under contract with NASA. This work has been supported by NASA NAG5-6035 (DJH), as well as by a small *Chandra* archival grant. MEE gratefully acknowledges support from the NASA Graduate Student Research Program. The work of DS was carried out at the Jet Propulsion Laboratory, California Institute of Technology, under a contract with NASA.

REFERENCES

- Akiyama, M., Ueda, Y., Ohta, K., Takahashi, T., and Yamada, T. 2003, *ApJS*, 148, 275
- Akiyama, M. *et al.* 2000, *ApJ*, 532, 700
- Alexander, D. M. *et al.* 2003, *AJ*, 126, 539
- Antonucci, R. 1993, *ARA&A*, 31, 473
- Baldi, A., Molendi, S., Comastri, A., Fiore, F., Matt, G., and Vignali, C. 2002, *ApJ*, 564, 190
- Barger, A. *et al.* 2003, *AJ*, 126, 632
- Barger, A. J., Cowie, L. L., Bautz, M. W., Brandt, W. N., Garmire, G. P., Hornschemeier, A. E., Ivison, R. J., and Owen, F. N. 2001, *AJ*, 122, 2177
- Bauer, F. E., Alexander, D. M., Brandt, W. N., Schneider, D. P., Treister, E., Hornschemeier, A. E., and Garmire, G. P. 2004, *AJ*, 128, 2048
- Bautz, M. W. *et al.* 1998, in *Proc. SPIE Vol. 3444*, p. 210-224, X-Ray Optics, Instruments, and Missions, Richard B. Hoover; Arthur B. Walker; Eds., 210-224
- Becker, R. H., White, R. L., and Helfand, D. J. 1995, *ApJ*, 450, 559
- Brandt, W. N. and Hasinger, G. 2005, *astro-ph/0501058*
- Brinkmann, W. *et al.* 1997, *A&A*, 323, 739
- Broos, P., Townsley, L., Getman, K., and Bauer, F. 2002, *ACIS Extract*, An ACIS Point Source Extraction Package, Pennsylvania State University
- Brusa, M. *et al.* 2003, *A&A*, 409, 65
- Cash, W. 1979, *ApJ*, 228, 939
- Comastri, A. *et al.* 2002, *ApJ*, 571, 771
- Condon, J. J., Cotton, W. D., Greisen, E. W., Yin, Q. F., Perley, R. A., Taylor, G. B., and Broderick, J. J. 1998, *AJ*, 115, 1693
- Cowie, L. L., Garmire, G. P., Bautz, M. W., Barger, A. J., Brandt, W. N., and Hornschemeier, A. E. 2002, *ApJ*, 566, L5
- Dawson, S., McCrady, N., Stern, D., Eckart, M. E., Spinrad, H., Liu, M. C., and Graham, J. R. 2003, *AJ*, 125, 1236
- Dickey, J. M. and Lockman, F. J. 1990, *ARA&A*, 28, 215
- Dressler, A. and Gunn, J. E. 1983, *ApJ*, 270, 7
- Eckart, M. E., Laird, E. S., Stern, D., Mao, P. H., Helfand, D. J., and Harrison, F. A. 2005, *ApJS*, 156, 35
- Faber, S. M. *et al.* 2003, in *Instrument Design and Performance for Optical/Infrared Ground-based Telescopes*. Edited by Iye, Masanori; Moorwood, Alan F. M. *Proceedings of the SPIE*, Volume 4841, pp. 1657-1669 (2003), ed. M. Iye & A. F. M. Moorwood, 1657-1669
- Feigelson, E. D. *et al.* 2004, *ApJ*, 611, 1107
- Fiore, F. *et al.* 2003, *A&A*, 409, 79
- Gallagher, S. C., Brandt, W. N., Chartas, G., and Garmire, G. P. 2002, *ApJ*, 567, 37
- Gilfanov, M., Grimm, H.-J., and Sunyaev, R. 2004, *MNRAS*, 347, L57
- Gioia, I. M., Maccaro, T., Schild, R. E., Wolter, A., Stocke, J. T., Morris, S. L., and Henry, J. P. 1990, *ApJS*, 72, 567
- Giommi, P., Menna, M. T., and Padovani, P. 1999, *MNRAS*, 310, 465
- Glikman, E., Gregg, M. D., Lacy, M., Helfand, D. J., Becker, R. H., and White, R. L. 2004, *ApJ*, 607, 60
- Green, P. J. *et al.* 2004, *ApJS*, 150, 43
- Grimm, H.-J., Gilfanov, M., and Sunyaev, R. 2003, *MNRAS*, 339, 793
- Halpern, J. P., Turner, T. J., and George, I. M. 1999, *MNRAS*, 307, L47
- Harrison, F. A., Eckart, M. E., Mao, P. H., Helfand, D. J., and Stern, D. 2003, *ApJ*, 596, 944
- Helfand, D. J. and Moran, E. C. 2001, *ApJ*, 554, 27
- Henry, J. P., Gioia, I. M., Mullis, C. R., Voges, W., Briel, U. G., Böhringer, H., and Huchra, J. P. 2001, *ApJ*, 553, L109
- Holden, B. P., Stanford, S. A., Squires, G. K., Rosati, P., Tozzi, P., Eisenhardt, P., and Spinrad, H. 2002, *AJ*, 124, 33
- Hornschemeier, A. E. *et al.* 2001, *ApJ*, 554, 742
- Iyengar, V. S., Naranan, S., and Sreekantan, B. V. 1975, *Ap&SS*, 32, 431
- Kim, D.-W. *et al.* 2004, *ApJS*, 150, 19
- La Franca, F. *et al.* 2002, *ApJ*, 570, 100
- Laurent-Muehleisen, S. A., Kollgaard, R. I., Feigelson, E. D., Brinkmann, W., and Siebert, J. 1999, *ApJ*, 525, 127
- Martini, P., Kelson, D. D., Mulchaey, J. S., and Trager, S. C. 2002, *ApJL*, 576, L109
- Massey, P., Gronwall, C., and Pilachowski, C. A. 1990, *PASP*, 102, 1046
- Matt, G. 2002, *Royal Society of London Philosophical Transactions Series A*, 360, 2045
- McLean, B. J., Greene, G. R., Lattanzi, M. G., and Pirenne, B. 2000, in *ASP Conf. Ser. 216: ADASS IX*, 145
- Moran, E. C., Filippenko, A. V., and Chornock, R. 2002, *ApJ*, 579, L71
- Moran, E. C., Lehnert, M. D., and Helfand, D. J. 1999, *ApJ*, 526, 649
- Morrison, R. and McCammon, D. 1983, *ApJ*, 270, 119
- Newman, J. A. *et al.* 2005, in preparation
- Norman, C. *et al.* 2002, *ApJ*, 571, 218
- Oke, J. B. and Gunn, J. E. 1982, *PASP*, 94, 586
- Oke, J. B. *et al.* 1995, *PASP*, 107, 375
- Perola, G. C. *et al.* 2004, *A&A*, 421, 491

- Pizzolato, N., Maggio, A., Micela, G., Sciortino, S., and Ventura, P. 2003, A&A, 397, 147
- Ranalli, P., Comastri, A., and Setti, G. 2003, A&A, 399, 39
- Rosati, P. *et al.* 2002, ApJ, 566, 667
- Silverman, J. D. *et al.* 2005, ApJ, 618, 123
- Steffen, A. T., Barger, A. J., Capak, P., Cowie, L. L., Mushotzky, R. F., and Yang, Y. 2004, AJ, 128, 1483
- Steidel, C. C., Shapley, A. E., Pettini, M., Adelberger, K. L., Erb, D. K., Reddy, N. A., and Hunt, M. P. 2004, ApJ, 604, 534
- Stern, D. *et al.* 2002a, ApJ, 568, 71
- . 2002b, AJ, 123, 2223
- Stern, D., Holden, B., Stanford, S. A., and Spinrad, H. 2003, AJ, 125, 2759
- Stern, D., Yost, S. A., Eckart, M. E., Harrison, F. A., Helfand, D. J., Djorgovski, S. G., Malhotra, S., and Rhoads, J. E. 2005, ApJ, 619, 12
- Stocke, J. T., Morris, S. L., Gioia, I. M., Maccacaro, T., Schild, R., Wolter, A., Fleming, T. A., and Henry, J. P. 1991, ApJS, 76, 813
- Szokoly, G. P. *et al.* 2004, ApJS, 155, 271
- Treister, E. *et al.* 2004, ApJ, 616, 123
- Treister, E. *et al.* 2005, ApJ, 621, 104
- Vanden Berk, D. E. *et al.* 2001, AJ, 122, 549
- Veilleux, S. and Osterbrock, D. E. 1987, ApJS, 63, 295
- Wolf, C., Wisotzki, L., Borch, A., Dye, S., Kleinheinrich, M., and Meisenheimer, K. 2003, A&A, 408, 499
- Worsley, M. A. *et al.* 2005, MNRAS, 107
- Yang, Y., Mushotzky, R. F., Steffen, A. T., Barger, A. J., and Cowie, L. L. 2004, AJ, 128, 1501
- Yuan, F. and Narayan, R. 2004, ApJ, 612, 724

TABLE 1
SEXSI FIELDS.

Name	R.A. (J2000)	Decl. (J2000)	Exp. [ks]	# 2–10 keV srcs in X-ray area ^a	# 2–10 keV srcs in opt area ^b	# with phot. ID $R < 22$	# with phot. ID $R < 23$	# with phot. ID $R < 24^c$	# with z	# with cont. ^d
NGC 891	02 22 33	+42 20 57	51	21	19	10	13	14	6	3
AWM 7	02 54 28	+41 34 47	48	28	24	11	14	16	14	2
XRF 011130	03 05 28	+03 49 59	30	33	33	17	21	24	20	2
NGC 1569	04 30 49	+64 50 54	97	33	31	18	19	19	16	3
3C 123	04 37 55	+29 40 14	47	26	25	13	15	15	7	3
CL 0442+0202	04 42 26	+02 00 07	44	45	37	2 ^e	2 ^e	2 ^e	7	0
CL 0848+4454	08 48 32	+44 53 56	186	81	72	25	37	49	47	4
RX J0910	09 10 39	+54 19 57	171	92	89	25	43	55	40	4
1156+295	11 59 32	+29 14 44	49	44	42	20	24	29	7	0
NGC 4244	12 17 30	+37 48 32	49	31	28	9	17	19	8	0
NGC 4631	12 42 07	+32 32 30	59	23	23	7	11	12	0	0
HCG 62	12 53 08	−09 13 27	49	39	37	22	27	30	20	2
RX J1317	13 17 12	+29 11 17	111	62	60	17	29	31	27	1
BD 1338	13 38 25	+29 31 05	38	45	43	20	26	29	23	0
RX J1350	13 50 55	+60 05 09	58	35	33	12	15	15	0	0
3C 295	14 11 20	+52 12 21	23	8	8	3	5	5	4	0
GRB 010222	14 52 12	+43 01 44	18	23	23	14	18	18	12	0
QSO 1508	15 09 58	+57 02 32	89	47	39	11	15	17	18	0
MKW 3S	15 21 52	+07 42 32	57	36	33	16	20	21	8	1
MS 1621	16 23 36	+26 33 50	30	25	24	11	13	15	11	2
GRB 000926	17 04 10	+51 47 11	32	30	29	19	21	23	20	1
RX J1716	17 16 52	+67 08 31	52	46	45	13	22	28	29	0
NGC 6543	17 58 29	+66 38 29	46	21	21	9	10	11	6	1
XRF 011030	20 43 32	+77 16 43	47	27	23	8	12	12	5	2
MS 2053	20 56 22	−04 37 44	44	48	44	23	27	31	23	2
RX J2247	22 47 29	+03 37 13	49	50	50	19	26	32	27	4
Q2345	23 48 20	+00 57 21	74	35	34	16	21	23	22	2
TOTAL			1648	1034	969	390	523	595	438	39

^aThis column gives numbers from the entire X-ray catalog from Paper I.

^bThis column gives numbers from the portion of the X-ray catalog that has adequate imaging coverage. This column excludes sources from the X-ray catalog that lack imaging coverage (optflag=0; Paper II) or fall near a bright source such that the optical counterpart is not identified and the R_{limit} cannot be determined (optflag=6; Paper II).

^cThis column gives the number of *confirmed* sources with $R < 24$. Additional sources may have $R < 24$ in cases where $R_{\text{limit}} < 24$.

^dSources with spectra that show continuum-only – no emission lines or absorption features – and thus no redshift or classification was determined.

^eField CL 0442+0202 has shallow R -band imaging ($R_{\text{limit}} = 21.1$). Since the numbers listed in this table are *confirmed* optical counterparts, this row indicates few R -band identifications.

TABLE 2
SEXSI OPTICAL SPECTROSCOPY CATALOG.

CXOSEXSI_ (1)	X-ray Data						Optical Counterpart Data											
	α_x (J2000) (2) ^a	δ_x (J2000) (3) ^a	OAA (4)	$S_{2-10}^{(-15)}$ (5)	HR (6) ^b	Flag (7) ^c	R (8)	R_{limit} (9)	$\log \frac{L_x}{L_{\odot}}$ (10)	z (11)	Class (12) ^d	Notes (13) ^e	$\Delta\lambda_{\text{rest}}$ (14) ^f	$\log L_x^{(2-10)}$ (15)	$\log N_H$ (16) ^g	$\log N_H^-$ (17) ^g	$\log N_H^+$ (18) ^g	
J022142.6+422654	02 21 42.75	+42 26 53.5	9.49	23.10	-0.33	1	18.73	24.3	-0.64	0.310	BLAGN	...	3553-7500	42.9	21.6 ^j	
J022205.0+422338	02 22 05.08	+42 23 37.7	4.24	8.73	0.84 ^h	1	20.37	24.3	-0.41	0.622	ELG	...	2953-6165	43.1	23.7	23.5	23.9	
J022210.8+422016	02 22 10.93	+42 20 16.1	2.17	3.63	-0.46	1	21.57	24.3	-0.31	3.563	BLAGN	...	1174-2321	44.3	22.1	<	22.7	
J022215.0+422341	02 22 15.12	+42 23 41.0	3.15	15.40	-0.41	1	22.52	24.3	0.70	4515-9740 ⁱ	
J022215.1+422045	02 22 15.19	+42 20 44.5	1.32	42.90	-0.42	1	17.33	24.3	-0.94	0.155	ELG	...	4454-8982	42.5	<	<	20.0	
J022215.5+421842	02 22 15.63	+42 18 41.7	2.46	6.79	0.28	1	20.33	24.3	-0.54	1.063	ELG	K	2695-5225	43.5	21.8	21.3	22.1	
J022219.3+422052	02 22 19.40	+42 20 51.6	0.54	6.38	0.37	1	23.82	24.3	0.83	5000-10225 ⁱ	
J022224.3+422139	02 22 24.45	+42 21 38.4	0.91	64.60	-0.44	1	17.41	24.3	-0.73	1.181	BLAGN	...	2152-4539	44.6	20.8	20.3	21.1	
J022236.3+421730	02 22 36.45	+42 17 30.2	4.23	12.00	0.01	1	22.38	24.3	0.53	5765-9700 ⁱ	
J025400.3+414006	02 54 00.28	+41 40 06.2	7.34	230.00	-0.41	1	19.56	24.2	0.69	0.420	BLAGN	...	4056-6651	44.1	20.8	20.3	21.0	
J025416.8+414142	02 54 16.78	+41 41 42.7	4.65	14.30	-0.44	1	22.36	24.2	0.60	2.635	BLAGN	...	1337-2751	44.6	22.8	22.5	22.9	
J025420.9+414032	02 54 20.92	+41 40 32.1	3.55	6.65	-0.18	2	24.20	24.2	1.00	4510-9700 ⁱ	
J025430.5+414213	02 54 30.51	+41 42 13.2	2.91	10.50	-0.18	1	20.96	24.2	-0.09	0.000	star	...	4520-9740	
J025435.6+414100	02 54 35.60	+41 41 00.3	1.37	27.90	-0.21	2	24.20	24.2	1.63	1.194	ELG	...	2431-4785	44.2	22.4	22.2	22.5	
J025437.0+414100	02 54 36.98	+41 41 00.7	1.26	24.60	-0.34	1	22.38	24.2	0.84	0.842	BLAGN	...	2874-5700	43.8	21.6	21.3	21.8	
J025438.5+414529	02 54 38.53	+41 45 29.2	5.64	16.70	-0.29	2	24.20	24.2	1.40	0.438	ELG	K	3376-6954	43.0	21.1	<	21.5	
J025440.6+414414	02 54 40.57	+41 44 14.5	4.39	6.04	-0.27	1	23.81	24.2	0.81	1.306	ELG	...	1960-4243	43.6	22.3	21.8	22.6	
J025443.4+414505	02 54 43.37	+41 45 05.1	5.28	9.01	-0.16	2	24.20	24.2	1.13	4605-9850 ⁱ	
J025445.5+414156	02 54 45.51	+41 41 56.3	2.36	6.10	0.30 ^h	4	22.57	24.2	0.31	0.763	ELG	...	2904-5870	43.1	23.3	22.9	23.6	
J025446.3+414757	02 54 46.32	+41 47 57.6	8.20	71.70	-0.37	1	18.12	24.2	-0.40	2.351	BLAGN	...	1507-3058	45.2	21.6	<	22.0	
J025446.3+414021	02 54 46.34	+41 40 21.1	1.36	13.50	-0.55	1	19.74	24.2	-0.47	1.516	BLAGN	...	1919-3974	44.1	21.9	21.5	22.1	
J025449.5+414550	02 54 49.51	+41 45 50.4	6.27	10.00	-0.43	1	22.67	24.2	0.57	2.458	BLAGN	...	1314-2826	44.4	22.4	21.7	22.7	
J025449.7+414530	02 54 49.68	+41 45 30.0	5.95	64.90	-0.46	1	19.62	24.2	0.16	1.370	BLAGN	...	1883-4092	44.7	20.7	<	21.4	
J025454.3+414006	02 54 54.32	+41 40 06.5	2.76	8.92	0.00	1	23.38	24.2	0.80	2.587	NLAGN	...	1239-2705	44.4	23.6	23.3	23.7	
J025509.9+415000	02 55 09.90	+41 50 00.5	11.62	39.10	-0.47	1	19.15	24.2	-0.25	0.730	BLAGN	...	3023-5179	43.9	<	<	20.8	
J030446.2+034948	03 04 46.26	+03 49 48.7	10.29	32.30	-0.51	1	20.17	23.2	0.08	0.778	BLAGN	...	3143-5340	43.9	20.3	<	21.4	
J030509.6+035027	03 05 09.64	+03 50 27.7	4.48	7.49	-0.00	1	20.72	23.2	-0.34	2.114	BLAGN	...	1518-3195	44.2	22.9	22.5	23.2	
J030512.8+034935	03 05 12.85	+03 49 36.0	3.68	8.61	-0.22	1	21.71	23.2	0.12	3.035	BLAGN	...	1220-2519	44.5	23.0	22.6	23.3	
J030514.2+034853	03 05 14.17	+03 48 53.9	3.50	25.40	0.45	1	21.84	23.2	0.64	0.913	NLAGN	...	2665-5397	43.9	23.0	22.9	23.1	
J030517.9+035046	03 05 17.91	+03 50 47.2	2.52	8.20	-0.62	1	20.12	23.2	-0.54	1.579	BLAGN	...	1773-3801	43.9	<	<	21.5	
J030522.3+035354	03 05 22.31	+03 53 55.0	4.13	6.54	-0.24	1	21.99	23.2	0.11	0.768	ELG	N	2519-5605	43.2	22.1	21.3	22.5	
J030522.7+034934	03 05 22.69	+03 49 35.4	1.27	5.13	0.63 ^h	1	23.08	23.2	0.44	1.089	ELG	...	2324-4786	43.4	23.8	23.5	24.0	
J030525.3+035211	03 05 25.35	+03 52 11.9	2.27	5.16	0.68 ^h	1	16.57	23.2	-2.16	0.090	ELG	...	4193-9010	41.1	23.6	23.3	23.8	
J030527.0+035528	03 05 26.97	+03 55 29.3	5.49	9.01	0.06	1	17.61	23.2	-1.50	0.000	star	A	5165-10380	
J030527.8+034656	03 05 27.84	+03 46 56.9	3.05	48.80	-0.25	1	19.90	23.2	0.15	0.351	ELG	...	4067-7772	43.3	21.3	21.0	21.5	
J030529.3+034115	03 05 29.30	+03 41 16.4	8.73	15.60	0.64 ^h	1	22.18	23.2	0.57	5250-10400 ⁱ	
J030532.4+035139	03 05 32.46	+03 51 40.2	2.08	27.90	-0.50	1	19.90	23.2	-0.09	1.183	BLAGN	...	2242-4635	44.2	21.4	<	21.8	
J030532.6+034301	03 05 32.58	+03 43 02.0	7.08	16.20	0.49	4	19.12	23.2	-0.64	0.241	ELG	...	3867-8058	42.5	23.2	23.1	23.4	
J030533.0+034927	03 05 32.99	+03 49 28.4	1.46	6.38	0.07	1	23.03	23.2	0.52	1.128	ELG	...	2255-4699	43.5	22.7	22.4	23.0	
J030534.2+034958	03 05 34.21	+03 49 58.9	1.67	10.40	-0.43	1	20.53	23.2	-0.27	1.495	BLAGN	...	1887-3987	44.0	22.0	21.0	22.3	
J030534.8+035147	03 05 34.82	+03 51 48.3	2.57	15.30	0.62	1	22.95	23.2	0.86	1.483	ELG	K	2027-4138	44.2	23.7	23.6	23.9	
J030535.8+034639	03 05 35.82	+03 46 40.4	3.92	10.10	-0.37	1	22.33	23.2	0.44	1.564	ELG	K	2145-4167	44.0	22.8	22.5	23.1	
J030537.0+034125	03 05 37.01	+03 41 26.0	8.88	81.80	-0.25	1	23.26	23.2	1.72	1.276	ELG	...	2311-4613	44.7	22.1	21.9	22.2	
J030538.1+034816	03 05 38.10	+03 48 17.4	3.15	7.88	0.82 ^h	2	23.20	23.2	0.69	4795-10000 ⁱ	
J030539.9+034148	03 05 39.92	+03 41 49.3	8.74	39.20	-0.49	1	20.84	23.2	0.43	1.137	BLAGN	...	2423-4859	44.3	<	<	21.2	
J030541.4+034806	03 05 41.42	+03 48 07.3	3.94	10.50	-0.37	1	22.77	23.2	0.63	0.710	ELG	...	2807-5847	43.3	21.7	<	22.2	
J030550.0+035008	03 05 50.06	+03 50 08.9	5.63	10.40	-0.35	1	21.67	23.2	0.19	1.104	BLAGN	...	2654-5123	43.7	21.6	<	22.1	
J042900.3+644608	04 29 00.36	+64 46 08.2	12.76	32.60	-0.81	3	13.80	21.5	-2.47	0.000	star	B	
J042941.6+644834	04 29 41.70	+64 48 33.9	7.91	17.20	0.79 ^h	1	21.02	21.5	0.14	0.767	ELG	...	2119-5660	43.6	23.2 ^{j,k}	
J042952.4+644253	04 29 52.54	+64 42 52.8	9.59	23.90	-0.25	1	21.75	21.5	0.58	2.049	BLAGN	...	1534-3279	44.6	22.7 ^j	
J042958.2+643938	04 29 58.33	+64 39 37.7	11.82	45.80	-0.36	2	21.00	21.0	0.56	4200-9500 ⁱ	

TABLE 2 — *Continued*

CXOEXSL_	X-ray Data						Optical Counterpart Data											
	α_x (J2000)	δ_x (J2000)	OAA	$S_{2-10}^{(-15)}$	HR	Flag	R	R_{limit}	$\log \frac{L_x}{L_{\odot}}$	z	Class	Notes	$\Delta\lambda_{\text{rest}}$	$\log L_x^{(2-10)}$	$\log N_{\text{H}}$	$\log N_{\text{H}}^-$	$\log N_{\text{H}}^+$	
(1)	(2) ^a	(3) ^a	(4)	(5)	(6) ^b	(7) ^c	(8)	(9)	(10)	(11)	(12) ^d	(13) ^e	(14) ^f	(15)	(16) ^g	(17) ^g	(18) ^g	
J043000.2+644525	04 30 00.29	+64 45 25.0	7.29	8.84	0.60 ^h	5	22.53	21.5	0.46	0.753	ALG	...	2852–5704	43.3	23.0 ^{jk}	
J043016.8+644317	04 30 16.90	+64 43 17.3	7.66	14.20	−0.29	1	19.92	21.5	−0.38	2.953	BLAGN	...	1328–2648	44.7	22.9 ^j	
J043025.2+645035	04 30 25.28	+64 50 35.0	3.29	8.71	−0.26	1	21.11	23.0	−0.12	1.573	BLAGN	...	2020–3886	44.0	22.7	22.5	22.8	
J043030.9+645205	04 30 30.98	+64 52 04.8	3.46	17.30	−0.35	1	18.71	23.0	−0.78	0.547	BLAGN	...	2585–5946	43.3	21.4	21.2	21.6	
J043032.6+644025	04 30 32.74	+64 40 24.7	9.66	29.20	−0.13	1	20.70	21.0	0.25	0.768	ELG	...	2319–5429	43.8	22.3 ^j	
J043034.3+644740	04 30 34.37	+64 47 40.0	3.06	44.20	−0.26	1	18.68	23.0	−0.38	4910–10000 ⁱ	
J043111.5+644947	04 31 11.60	+64 49 46.4	1.74	3.60	−0.12	1	21.21	22.5	−0.46	0.662	ELG	N	3206–6317	42.8	22.1	21.7	22.3	
J043113.2+645229	04 31 13.26	+64 52 29.0	3.32	29.70	−0.46	1	19.76	22.5	−0.12	1.579	BLAGN	...	1527–3450	44.5	21.4	20.9	21.6	
J043114.0+645107	04 31 14.08	+64 51 07.3	2.42	5.10	−0.95	3	12.41	22.5	−3.83	0.000	star	...	5140–10150	
J043114.5+645024	04 31 14.58	+64 50 24.3	2.15	9.22	0.03	1	22.28	22.5	0.38	5285–10450 ⁱ	
J043116.8+644950	04 31 16.90	+64 49 49.5	2.30	98.50	−0.84	3	12.29	22.5	−2.59	0.000	star	...	5425–10620	
J043120.5+645122	04 31 20.57	+64 51 21.9	3.13	20.40	−0.23	1	19.73	22.5	−0.30	0.638	ELG	...	3302–6150	43.5	21.4	21.3	21.6	
J043124.3+645121	04 31 24.42	+64 51 20.7	3.48	6.11	0.41	1	20.25	22.5	−0.61	0.521	ELG	...	3668–6574	42.8	22.6	22.4	22.7	
J043125.1+645154	04 31 25.22	+64 51 53.6	3.83	119.00	0.86	4	15.66	22.5	−1.16	0.279	ELG	...	4413–7689	43.5	23.2	23.1	23.2	
J043129.2+645052	04 31 29.34	+64 50 52.1	3.79	11.60	−0.08	1	18.55	22.5	−1.02	2.074	BLAGN	...	1219–3253	44.3	22.5	22.3	22.6	
J043641.6+295126	04 36 41.65	+29 51 26.7	12.83	526.00	−0.78	3	12.72	21.9	−1.69	0.000	star	B	
J043646.8+293832	04 36 46.84	+29 38 32.3	3.94	87.70	−0.13	1	18.81	21.9	−0.03	0.970	BLAGN	...	2286–4934	44.5	22.2	22.1	22.3	
J043650.1+293515	04 36 50.15	+29 35 15.9	5.31	6.49	−0.39	1	20.79	21.9	−0.37	4860–10000 ⁱ	
J043654.8+294018	04 36 54.89	+29 40 18.1	2.17	16.70	−0.12	1	20.06	21.9	−0.25	0.891	BLAGN	...	2562–5288	43.7	21.9	21.6	22.1	
J043656.2+293959	04 36 56.22	+29 39 59.9	1.80	8.91	0.25	1	20.53	21.9	−0.34	0.755	ELG	...	2809–5754	43.3	22.5	22.3	22.6	
J043657.4+294234	04 36 57.41	+29 42 34.8	3.34	6.39	0.10	2	21.90	21.9	0.06	4840–10000 ⁱ	
J043700.3+293525	04 37 00.33	+29 35 25.5	4.25	22.30	0.01	1	21.15	21.9	0.31	1.503	BLAGN	K	2161–4194	44.3	22.8	22.6	22.9	
J043701.1+294148	04 37 01.18	+29 41 48.5	2.32	12.50	0.75 ^h	1	20.41	21.9	−0.24	0.726	ELG	...	2954–5967	43.4	23.1	22.9	23.2	
J043712.4+294331	04 37 12.44	+29 43 31.0	4.30	35.70	−0.14	1	20.61	21.9	0.30	5595–10500 ⁱ	
J043712.5+294631	04 37 12.56	+29 46 31.5	7.16	25.10	−0.16	1	18.81	21.9	−0.58	2.533	BLAGN	...	1553–2915	44.8	22.8	22.7	22.9	
J044213.1+020437	04 42 13.18	+02 04 38.9	5.48	22.50	−0.13	2	21.10	21.1	0.29	1.380	BLAGN	...	1512–3235	44.3	22.2	21.9	22.4	
J044223.1+020208	04 42 23.13	+02 02 09.5	2.12	13.70	−0.56	1	20.39	21.1	−0.21	0.886	BLAGN	...	1908–4984	43.6	20.5	<	21.5	
J044223.1+020219	04 42 23.15	+02 02 20.5	2.29	25.50	−0.22	2	21.10	21.1	0.34	0.835	BLAGN	...	1961–4795	43.8	21.7	21.2	21.9	
J044223.5+020231	04 42 23.54	+02 02 32.7	2.47	4.16	−0.49	2	21.10	21.1	−0.44	2.749	BLAGN	...	960–2507	44.1	22.7	21.7	23.0	
J044223.7+020219	04 42 23.73	+02 02 20.6	2.26	66.60	−0.29	2	21.10	21.1	0.76	1.110	BLAGN	H	2654–4407	44.5	21.5	21.0	21.8	
J044224.1+020310	04 42 24.16	+02 03 12.0	3.09	9.06	0.33	0	1.133	ELG	...	2766–4453	43.7	22.1	21.9	22.3	
J044234.2+020510	04 42 34.21	+02 05 11.4	5.50	8.28	−0.31	2	21.10	21.1	−0.15	0.772	ELG	...	3047–4401	43.3	22.2	21.5	22.4	
J044236.1+020325	04 42 36.19	+02 03 26.9	4.25	15.10	−0.10	2	21.10	21.1	0.11	1.863	NLAGN	...	1257–1955	44.4	23.0	22.8	23.1	
J084811.7+445302	08 48 11.77	+44 53 03.3	7.77	8.01	0.44	1	23.46	24.4	0.79	3900–9000 ⁱ	
J084818.4+444844	08 48 18.52	+44 48 45.5	8.67	9.18	−0.40	1	20.66	24.4	−0.27	0.405	ELG	...	3380–6690	42.7	<	<	20.5	
J084822.2+445223	08 48 22.28	+44 52 25.0	6.15	3.54	−0.04	1	23.32	24.4	0.38	2.187	BLAGN	J	1317–2949	43.9	20.8	<	22.0	
J084822.5+445854	08 48 22.62	+44 58 55.9	7.17	3.67	−0.14	1	21.08	24.4	−0.50	0.413	NLAGN	A	2830–6475	42.3	21.7	<	22.1	
J084823.9+445852	08 48 23.94	+44 58 53.8	6.96	6.62	−0.46	1	22.01	24.4	0.12	1.342	BLAGN	A	1793–3970	43.7	21.9	21.6	22.1	
J084824.6+445355	08 48 24.70	+44 53 56.3	5.36	2.61	0.03	1	22.21	24.4	−0.20	0.747	ELG	...	2518–5294	42.7	22.4	22.2	22.6	
J084824.8+445740	08 48 24.83	+44 57 41.3	6.15	3.18	0.25	1	20.52	24.4	−0.79	0.337	ELG	A	2991–7068	42.1	22.5	22.3	22.6	
J084825.1+444808	08 48 25.14	+44 48 09.5	8.29	7.61	−0.55	1	20.73	24.4	−0.33	1.320	BLAGN	...	2327–4051	43.7	<	<	20.7	
J084827.2+445433	08 48 27.29	+44 54 35.1	4.87	9.98	−0.40	1	20.33	24.4	−0.37	0.899	BLAGN	J	2227–4939	43.5	<	<	20.5	
J084827.4+445604	08 48 27.51	+44 56 06.0	5.06	4.56	0.31	1	23.67	24.4	0.63	1.528	ELG	...	1424–3716	43.7	22.7	22.5	22.9	
J084830.2+445604	08 48 30.23	+44 56 06.0	4.60	2.55	−0.18	2	24.40	24.4	0.67	4800–9000 ⁱ	
J084831.6+445442	08 48 31.71	+44 54 43.6	4.09	2.44	−0.15	1	25.42	24.4	1.06	1.267	ELG	KN	1588–4146	43.2	22.0	21.6	22.3	
J084832.7+445711	08 48 32.75	+44 57 12.2	4.70	2.62	0.57	1	22.01	24.4	−0.28	0.749	ELG	...	2172–5431	42.7	23.0	22.9	23.1	
J084836.9+444818	08 48 37.02	+44 48 19.9	6.99	22.50	−0.49	1	20.67	24.4	0.12	0.646	BLAGN	...	2551–5443	43.5	<	<	20.0	
J084837.5+445710	08 48 37.60	+44 57 12.1	4.02	7.47	0.23	6	0.569	BLAGN	...	2421–6054	42.9	21.9	21.8	22.0	
J084837.9+445352	08 48 37.94	+44 53 53.2	3.06	4.62	0.15	1	24.22	24.4	0.85	3.287	NLAGN	...	979–2169	44.3	23.6	23.4	23.7	
J084840.3+445800	08 48 40.37	+44 58 01.3	4.29	49.20	−0.34	1	21.23	24.4	0.68	0.716	BLAGN	...	2447–5477	44.0	21.3	21.2	21.4	
J084840.5+445732	08 48 40.62	+44 57 33.3	3.89	9.72	−0.20	1	20.46	24.4	−0.33	3.093	BLAGN	J	934–2443	44.6	23.0	22.9	23.1	
J084843.2+445806	08 48 43.25	+44 58 07.2	4.09	3.74	0.69	1	21.54	24.4	−0.31	0.566	ELG	...	2426–6002	42.6	23.4	23.2	23.5	

TABLE 2 — *Continued*

CXOEXSL (1)	X-ray Data					Flag (7) ^c	Optical Counterpart Data											
	α_x (J2000) (2) ^a	δ_x (J2000) (3) ^a	OAA (4)	$S_{2-10}^{(-15)}$ (5)	HR (6) ^b		R (8)	R_{limit} (9)	$\log \frac{L_x}{L_{\odot}}$ (10)	z (11)	Class (12) ^d	Notes (13) ^e	$\Delta\lambda_{\text{rest}}$ (14) ^f	$\log L_x^{(2-10)}$ (15)	$\log N_{\text{H}}$ (16) ^g	$\log N_{\text{H}}^-$ (17) ^g	$\log N_{\text{H}}^+$ (18) ^g	
J084845.1+445453	08 48 45.18	+44 54 54.6	1.73	1.84	0.05	1	23.42	24.4	0.13	1.015	ELG	...	2084–4665	42.9	22.3	22.0	22.5	
J084845.4+445651	08 48 45.45	+44 56 52.8	2.83	1.55	0.20 ^h	1	24.93	24.4	0.66	1.329	ELG	...	3112–4036	43.1	23.4	23.2	23.5	
J084846.0+445945	08 48 46.11	+44 59 46.3	5.42	11.80	0.72	1	21.45	24.4	0.15	0.567	ELG	...	3012–5998	43.1	23.0	23.0	23.1	
J084846.4+444830	08 48 46.46	+44 48 32.0	6.22	7.07	0.47	1	20.55	24.4	−0.43	0.432	ELG	A	2932–6564	42.7	22.6	22.5	22.7	
J084846.5+445358	08 48 46.61	+44 53 59.8	1.56	2.98	−0.19	2	24.40	24.4	0.74	1.083	ELG	...	2016–4488	43.2	22.5	22.4	22.6	
J084853.8+445351	08 48 53.85	+44 53 52.7	0.71	4.93	0.26	1	21.68	24.4	−0.14	0.725	ELG	43.0	22.5	22.4	22.7	
J084854.4+445149	08 48 54.46	+44 51 50.4	2.73	14.90	−0.19	1	20.57	24.4	−0.10	1.035	BLAGN	...	2068–4486	43.8	21.7	21.5	21.8	
J084855.3+445009	08 48 55.33	+44 50 10.7	4.40	2.86	0.78 ^h	1	22.74	24.4	0.05	1.000	ELG	N	1800–4650	43.1	23.4	23.3	23.6	
J084856.6+445225	08 48 56.70	+44 52 26.8	2.16	6.60	−0.24	1	22.04	24.4	0.14	1.329	BLAGN	...	2361–3993	43.7	21.7	20.8	22.0	
J084857.7+445608	08 48 57.73	+44 56 09.5	1.67	2.50	−0.29	1	22.30	24.4	−0.18	0.621	ELG	...	2344–5675	42.5	21.8	21.5	22.0	
J084858.0+445434	08 48 58.11	+44 54 35.4	0.59	57.50	−0.56	1	19.58	24.4	0.09	0.573	BLAGN	...	2670–5975	43.8	<	<	<	
J084902.2+450003	08 49 02.27	+45 00 05.1	5.67	35.90	0.61	1	19.62	24.4	−0.10	0.524	NLAGN	...	2493–6069	43.5	22.8	22.8	22.9	
J084902.4+445705	08 49 02.49	+44 57 06.3	2.88	15.70	0.02	1	22.57	24.4	0.72	1.780	BLAGN	...	1366–3417	44.3	23.0	23.0	23.1	
J084902.5+450039	08 49 02.53	+45 00 40.5	6.25	12.60	−0.52	1	20.23	24.4	−0.31	0.523	BLAGN	...	2790–6106	43.1	<	<	20.0	
J084903.9+445023	08 49 04.02	+44 50 24.8	4.47	2.21	0.43	1	23.92	24.4	0.41	1.276	ELG	H	1845–4130	43.2	23.0	22.8	23.2	
J084904.0+445646	08 49 04.09	+44 56 47.1	2.76	2.19	0.38	1	25.12	24.4	0.89	1.263	ELG	...	2960–4197	43.2	23.1	22.9	23.2	
J084905.0+445714	08 49 05.06	+44 57 15.2	3.24	33.10	−0.47	1	19.54	24.4	−0.16	1.263	BLAGN	...	1869–4131	44.3	<	<	20.3	
J084905.3+445203	08 49 05.32	+44 52 04.3	3.12	9.62	0.64	1	24.61	24.4	1.33	1.266	ELG	H	2956–4148	43.8	23.4	23.3	23.5	
J084905.9+445037	08 49 06.02	+44 50 38.6	4.41	2.22	0.72 ^h	1	23.99	24.4	0.44	6700–9200 ⁱ	
J084906.3+450107	08 49 06.36	+45 01 08.9	6.89	15.40	−0.27	1	21.98	24.4	0.48	1.272	BLAGN	...	1672–4159	44.0	22.0	21.8	22.1	
J084907.2+445813	08 49 07.24	+44 58 14.8	4.29	3.51	−0.15	1	22.59	24.4	0.08	0.860	BLAGN	...	2043–5107	43.0	21.8	21.5	22.1	
J084907.5+450151	08 49 07.54	+45 01 52.3	7.64	5.01	0.01	1	22.36	24.4	0.14	0.091	ELG	...	3483–8661	41.1	22.1	21.9	22.2	
J084908.2+445810	08 49 08.29	+44 58 11.2	4.33	3.13	−0.40	1	23.97	24.4	0.58	2.320	BLAGN	...	1265–2831	43.9	21.6	<	22.1	
J084908.6+445842	08 49 08.65	+44 58 43.4	4.82	4.87	−0.04	1	25.16	24.4	1.25	1.333	ELG	...	2871–3986	43.6	22.4	22.2	22.6	
J084911.3+445008	08 49 11.33	+44 50 09.2	5.31	10.40	0.14	1	23.28	24.4	0.83	1.515	BLAGN	...	1669–3737	44.0	22.5	22.2	22.6	
J084913.6+445238	08 49 13.67	+44 52 39.1	3.86	2.95	0.81 ^h	1	24.06	24.4	0.59	1.201	ELG	...	3225–4270	43.2	23.8	23.6	23.9	
J084916.2+445954	08 49 16.23	+44 59 55.6	6.56	4.38	0.25	1	25.62	24.4	1.39	3900–9400 ⁱ	
J084918.0+450114	08 49 18.05	+45 01 15.2	7.85	10.20	0.86 ^h	1	23.25	24.4	0.81	1.021	ELG	...	1929–4700	43.6	23.7	23.6	23.8	
J084919.5+445707	08 49 19.57	+44 57 08.1	5.08	4.59	−0.34	6	1.259	ELG	...	1593–4161	43.5	20.7	<	21.0	
J084922.5+445356	08 49 22.54	+44 53 57.4	4.95	15.50	−0.44	1	18.88	24.4	−0.76	0.510	BLAGN	J	2384–6225	43.2	21.1	20.8	21.2	
J084923.2+445249	08 49 23.27	+44 52 51.0	5.33	9.85	−0.35	4	19.20	24.4	−0.83	2.177	BLAGN	...	1133–2958	44.3	22.4	22.2	22.5	
J084927.7+445456	08 49 27.76	+44 54 58.1	5.85	142.00	0.53	1	20.76	24.4	0.96	0.884	BLAGN	...	2016–5042	44.6	23.0	23.0	23.0	
J084930.4+445224	08 49 30.49	+44 52 25.6	6.68	5.48	−0.22	1	22.34	24.4	0.17	1.108	ELG	...	3178–4459	43.4	21.1	20.7	21.3	
J084931.3+445549	08 49 31.38	+44 55 50.5	6.60	6.26	−0.09	1	21.20	24.4	−0.22	0.567	ALG	A	2425–6062	42.9	21.7	21.3	21.8	
J084934.6+445448	08 49 34.69	+44 54 49.6	7.07	4.28	0.71 ^h	1	22.18	24.4	0.00	0.716	ELG	...	2214–5477	42.9	23.3	23.3	23.5	
J090954.0+541752	09 09 54.10	+54 17 55.0	6.89	5.67	0.71	1	22.07	23.9	0.08	1.101	ELG	I	1665–4188	43.4	23.5	23.5	23.7	
J090955.5+541813	09 09 55.55	+54 18 15.4	6.59	5.13	0.42	1	22.21	23.9	0.09	1.102	ELG	AI	1665–4281	43.4	23.1	23.0	23.2	
J090955.9+542915	09 09 55.98	+54 29 17.7	11.23	1570.00	−0.75	3	9.62	23.9	−2.46	0.000	star	B	
J091008.0+541401	09 10 08.11	+54 14 04.1	7.45	3.73	−0.20	1	22.58	23.9	0.10	0.811	ELG	...	1932–4969	43.0	20.8	<	21.5	
J091008.2+541524	09 10 08.25	+54 15 26.5	6.40	14.40	0.56	1	21.94	23.9	0.43	0.670	ELG	...	2095–5089	43.4	22.9	22.8	23.0	
J091011.0+542721	09 10 11.13	+54 27 24.0	8.46	614.00	−0.43	1	17.05	23.9	0.11	0.622	BLAGN	N	2157–5024	44.9	<	<	<	
J091012.7+541205	09 10 12.74	+54 12 07.8	8.75	15.20	0.40	1	22.49	23.9	0.68	0.792	ALG	AN	2416–5161	43.6	22.5	22.4	22.7	
J091017.4+541757	09 10 17.46	+54 17 59.3	3.74	4.80	−0.73	3	12.79	23.9	−3.70	0.000	star	B	
J091020.7+541848	09 10 20.81	+54 18 51.1	2.91	5.65	−0.33	1	19.64	23.9	−0.89	2.794	BLAGN	...	922–2424	44.3	22.4	22.3	22.6	
J091021.9+541529	09 10 21.98	+54 15 31.9	5.11	2.89	0.35	1	23.44	23.9	0.34	0.482	ELG	...	2361–5566	42.4	22.2	21.8	22.4	
J091022.2+542007	09 10 22.32	+54 20 09.8	2.46	5.69	0.28	1	22.37	23.9	0.20	0.898	ELG	N	2223–4952	43.3	22.8	22.7	22.9	
J091023.3+541358	09 10 23.41	+54 14 01.2	6.40	14.40	−0.53	1	20.68	23.9	−0.07	0.499	NLAGN	...	2401–5803	43.1	<	<	<	
J091026.8+541241	09 10 26.90	+54 12 43.7	7.48	60.50	0.04	1	18.78	23.9	−0.21	0.373	NLAGN	...	2694–6991	43.4	21.9	21.9	21.9	
J091027.0+542054	09 10 27.05	+54 20 56.5	2.00	17.50	−0.32	1	21.58	23.9	0.38	1.638	BLAGN	...	1364–3184	44.3	21.4	20.8	21.7	
J091028.5+542320	09 10 28.59	+54 23 23.1	3.73	1.91	0.13	1	23.68	23.9	0.25	1.960	BLAGN	J	1182–2635	43.5	23.3	23.1	23.4	
J091028.6+541634	09 10 28.69	+54 16 37.0	3.70	1.73	0.73 ^h	1	22.91	23.9	−0.10	0.907	ELG	...	1835–4273	42.7	24.0	23.7	24.1	
J091028.9+541523	09 10 29.03	+54 15 26.1	4.79	24.60	−0.38	1	22.03	23.9	0.70	0.647	BLAGN	...	2125–4918	43.6	20.0	<	20.8	

TABLE 2 — *Continued*

CXOEXSL_	X-ray Data						Optical Counterpart Data											
	α_x (J2000)	δ_x (J2000)	OAA	$S_{2-10}^{(-15)}$	HR	Flag	R	R_{limit}	$\log \frac{L_x}{L_{\odot}}$	z	Class	Notes	$\Delta\lambda_{\text{rest}}$	$\log L_x^{(2-10)}$	$\log N_{\text{H}}$	$\log N_{\text{H}}^-$	$\log N_{\text{H}}^+$	
(1)	(2) ^a	(3) ^a	(4)	(5)	(6) ^b	(7) ^c	(8)	(9)	(10)	(11)	(12) ^d	(13) ^e	(14) ^f	(15)	(16) ^g	(17) ^g	(18) ^g	
J091029.0+542717	09 10 29.05	+54 27 19.3	7.48	234.00	-0.43	1	18.48	23.9	0.26	0.526	BLAGN	N	2522–6061	44.4	<	<	<	
J091029.8+542746	09 10 29.84	+54 27 48.8	7.94	12.40	-0.40	1	20.30	23.9	-0.29	2.327	BLAGN	N	1202–2810	44.5	<	<	21.4	
J091030.9+541914	09 10 30.99	+54 19 16.7	1.39	7.79	-0.35	1	23.88	23.9	0.94	4000–9500 ⁱ	
J091031.9+542342	09 10 31.94	+54 23 45.0	3.90	3.27	0.28	1	25.37	23.9	1.16	3900–7900 ⁱ	
J091032.9+541246	09 10 33.00	+54 12 48.4	7.24	5.47	-0.17	1	19.63	23.9	-0.91	0.595	ELG	...	2194–5793	42.8	20.3	<	21.3	
J091034.2+542408	09 10 34.25	+54 24 10.7	4.25	2.41	-0.13	1	21.24	23.9	-0.62	0.340	ELG	AN	2835–6716	42.0	21.6	< 21.0	21.9	
J091037.8+541543	09 10 37.89	+54 15 46.1	4.23	6.65	-0.36	1	23.59	23.9	0.76	3700–7800 ⁱ	
J091037.9+541608	09 10 37.98	+54 16 10.4	3.82	5.48	-0.26	1	22.42	23.9	0.21	1.102	ELG	...	1665–3758	43.4	21.2	<	21.6	
J091039.8+542032	09 10 39.86	+54 20 34.7	0.60	8.90	-0.29	1	21.93	23.9	0.22	2.450	BLAGN	J	1043–2666	44.4	22.4	22.2	22.6	
J091040.0+542259	09 10 40.12	+54 23 01.5	3.04	4.37	0.01	1	20.76	23.9	-0.56	0.252	ELG	N	2875–7188	41.9	21.7	21.5	21.9	
J091040.8+542006	09 10 40.89	+54 20 08.6	0.30	2.42	0.74 ^h	1	22.38	23.9	-0.16	1.097	ELG	...	1812–4434	43.1	23.7	23.5	23.9	
J091041.4+541945	09 10 41.52	+54 19 47.9	0.40	26.30	-0.40	1	21.38	23.9	0.47	0.786	BLAGN	N	2239–5240	43.8	21.4	21.2	21.5	
J091041.9+542127	09 10 41.97	+54 21 29.6	1.56	2.75	-0.26	1	21.13	23.9	-0.61	0.598	BLAGN	...	2190–5632	42.6	21.7	21.3	22.0	
J091041.9+542340	09 10 42.02	+54 23 42.8	3.75	10.50	-0.35	1	23.02	23.9	0.73	1.638	BLAGN	...	1326–3184	44.1	21.8	21.5	22.0	
J091042.7+542034	09 10 42.81	+54 20 37.1	0.83	1.46	0.05	1	22.59	23.9	-0.30	1.108	ELG	H	1802–4411	42.9	22.6	22.3	22.9	
J091047.6+542211	09 10 47.66	+54 22 13.5	2.56	1.82	-0.34	1	23.99	23.9	0.36	1.341	ELG	...	1495–3908	43.1	21.3	<	21.9	
J091049.7+541330	09 10 49.80	+54 13 33.2	6.62	9.45	0.71	1	23.52	23.9	0.88	1.008	ELG	...	1743–4731	43.6	23.3	23.1	23.4	
J091053.3+541819	09 10 53.42	+54 18 21.6	2.64	1.98	-0.29	1	22.93	23.9	-0.03	1.850	BLAGN	...	1228–2842	43.5	21.1	<	22.1	
J091057.0+542340	09 10 57.11	+54 23 43.2	4.56	5.61	-0.39	1	22.53	23.9	0.26	1.935	BLAGN	...	1192–2555	44.0	<	<	21.6	
J091059.4+541715	09 10 59.44	+54 17 17.5	4.01	20.00	-0.21	1	22.46	23.9	0.79	1.860	BLAGN	...	1223–3041	44.5	22.1	21.9	22.2	
J091059.8+542335	09 10 59.85	+54 23 37.9	4.73	2.69	0.58	1	19.79	23.9	-1.15	0.333	NLAGN	...	2850–7051	42.0	22.9	22.7	23.1	
J091100.2+542540	09 11 00.31	+54 25 43.2	6.51	23.80	-0.23	1	21.41	23.9	0.44	1.890	BLAGN	...	1211–3044	44.6	22.1	21.8	22.2	
J091107.8+541822	09 11 07.92	+54 18 24.9	4.48	698.00	0.62	1	21.66	23.9	2.01	0.761	NLAGN	...	2157–5139	45.2	23.1	23.0	23.2	
J091108.5+541752	09 11 08.59	+54 17 54.7	4.77	8.69	-0.34	1	22.38	23.9	0.39	3.234	BLAGN	...	909–2170	44.6	22.6	22.4	22.8	
J091112.8+542306	09 11 12.86	+54 23 08.4	5.84	17.80	0.11	1	23.65	23.9	1.21	0.754	ELG	...	2166–4917	43.6	22.5	22.4	22.5	
J091115.4+541919	09 11 15.51	+54 19 21.3	5.34	4.34	-0.17	1	23.30	23.9	0.46	4100–9400 ⁱ	
J091129.6+541308	09 11 29.69	+54 13 11.2	10.04	34.30	-0.36	1	21.68	23.9	0.71	0.899	BLAGN	...	1895–5050	44.0	21.2	21.1	21.4	
J091135.9+540814	09 11 36.03	+54 08 17.1	14.36	27.90	-0.38	0	1.435	BLAGN	...	1437–3696	44.4	<	<	20.5	
J115917.7+291647	11 59 17.79	+29 16 48.6	3.67	3.67	0.67	1	22.05	24.4	-0.12	0.662	ELG	...	2166–5595	42.8	23.5	23.2	23.8	
J115924.1+291512	11 59 24.19	+29 15 13.7	1.62	9.74	0.88 ^h	1	21.25	24.4	-0.01	0.625	NLAGN	...	2215–5692	43.1	23.3	23.2	23.5	
J115927.2+291849	11 59 27.26	+29 18 51.0	4.43	4.28	0.19	1	18.57	24.4	-1.44	0.256	ELG	...	2866–7484	41.9	22.4	22.1	22.6	
J115929.7+291428	11 59 29.76	+29 14 29.9	0.23	15.40	-0.45	1	22.63	24.4	0.74	2.280	BLAGN	...	1067–2850	44.5	22.3	22.0	22.5	
J115930.1+291744	11 59 30.16	+29 17 45.2	3.27	6.48	-0.13	1	23.04	24.4	0.53	0.988	ELG	A	1760–4728	43.4	21.9	21.3	22.3	
J115931.1+291914	11 59 31.20	+29 19 15.4	4.77	5.94	0.39	1	23.89	24.4	0.83	2.425	NLAGN	...	1080–2627	44.2	22.6	22.0	23.0	
J115938.5+292055	11 59 38.54	+29 20 56.7	6.68	14.00	-0.45	1	21.36	24.4	0.19	0.922	BLAGN	J	1925–4838	43.7	21.5	20.3	21.8	
J121651.9+375438	12 16 51.91	+37 54 38.8	9.82	624.00	-0.51	3	12.96	22.9	-1.52	0.062	BLAGN	C	...	42.8	20.4 ^j	
J121726.9+374402	12 17 27.00	+37 44 02.9	2.96	25.10	0.52	1	22.15	23.4	0.76	0.727	ELG	...	2084–5500	43.7	22.8	22.7	22.9	
J121727.5+374412	12 17 27.55	+37 44 12.3	2.85	5.12	-0.36	1	22.21	23.4	0.09	0.679	ELG	...	2144–5866	42.9	21.9	21.7	22.0	
J121732.9+374644	12 17 32.96	+37 46 44.2	2.14	11.30	-0.34	1	20.90	23.4	-0.09	2.138	BLAGN	...	1115–3027	44.4	<	<	21.3	
J121733.0+375047	12 17 33.11	+37 50 47.3	4.50	4.98	-0.49	1	22.30	23.4	0.12	0.287	ELG	...	2719–7614	42.1	20.5	<	20.9	
J121739.5+374655	12 17 39.54	+37 46 55.1	3.44	5.38	0.86 ^h	1	23.04	23.4	0.45	0.000	star	A	3700–9900	
J121739.6+374646	12 17 39.68	+37 46 46.3	3.47	5.36	-0.51	2	23.40	23.4	0.61	2.987	NLAGN	...	928–2483	44.3	22.2	21.8	22.4	
J121740.1+374749	12 17 40.17	+37 47 49.3	3.70	20.80	-0.44	1	19.24	23.4	-0.49	1.795	BLAGN	J	1323–3398	44.5	<	<	20.6	
J125247.0-091637	12 52 47.01	-09 16 37.1	8.69	115.00	-0.53	1	18.24	23.4	-0.14	0.264	BLAGN	...	3058–7929	43.4	<	<	20.0	
J125252.8-091921	12 52 52.88	-09 19 21.5	10.20	76.30	-0.49	1	17.99	22.4	-0.42	1.111	BLAGN	...	1828–4737	44.6	<	<	20.8	
J125300.3-091104	12 53 00.37	-09 11 04.2	2.63	6.23	0.61 ^h	1	21.99	23.4	0.09	0.625	ELG	...	2154–6093	42.9	23.4	23.2	23.6	
J125301.9-091134	12 53 01.90	-09 11 34.0	2.54	6.90	-0.36	1	21.80	23.4	0.06	0.713	ELG	...	2159–5662	43.1	21.3	21.0	21.5	
J125302.4-091311	12 53 02.39	-09 13 11.7	3.65	106.00	-0.33	1	20.17	23.4	0.59	1.132	BLAGN	...	1512–4474	44.7	<	<	20.5	
J125302.9-091057	12 53 02.93	-09 10 57.5	2.01	6.97	0.65 ^h	1	20.86	23.4	-0.31	0.381	BLAGN	...	2535–7315	42.5	24.0	23.8	24.2	
J125303.0-091241	12 53 03.01	-09 12 41.7	3.15	15.80	-0.52	1	20.62	23.4	-0.05	0.983	ELG	...	1765–4992	43.8	21.0	20.6	21.2	
J125303.8-090809	12 53 03.84	-09 08 09.6	2.52	29.30	-0.16	1	17.96	23.4	-0.85	0.000	star	...	3865–9500	
J125304.7-090442	12 53 04.75	-09 04 42.3	5.57	17.50	-0.50	1	19.14	23.4	-0.60	1.706	BLAGN	...	1428–3695	44.3	<	<	20.9	

TABLE 2 — *Continued*

CXOEXSL (1)	X-ray Data						Optical Counterpart Data											
	α_x (J2000) (2) ^a	δ_x (J2000) (3) ^a	OAA (4)	$S_{2-10}^{(-15)}$ (5)	HR (6) ^b	Flag (7) ^c	R (8)	R_{limit} (9)	$\log \frac{L_x}{L_{\odot}}$ (10)	z (11)	Class (12) ^d	Notes (13) ^e	$\Delta\lambda_{\text{rest}}$ (14) ^f	$\log L_x^{(2-10)}$ (15)	$\log N_{\text{H}}$ (16) ^g	$\log N_{\text{H}}^-$ (17) ^g	$\log N_{\text{H}}^+$ (18) ^g	
J125305.3-090823	12 53 05.33	-09 08 23.5	2.11	31.60	-0.46	1	19.58	23.4	-0.17	0.499	NLAGN	...	2828-6671	43.4	<	<	20.0	
J125306.0-091316	12 53 05.99	-09 13 16.2	3.34	22.30	-0.08	1	21.84	23.4	0.58	3800-9400 ⁱ	
J125309.6-090323	12 53 09.64	-09 03 23.0	6.73	14.60	0.55	1	22.83	23.4	0.80	3800-9400 ⁱ	
J125310.4-091023	12 53 10.40	-09 10 23.4	0.28	12.80	-0.29	1	21.58	22.9	0.24	0.558	BLAGN	...	2458-6482	43.2	20.8	20.0	21.0	
J125310.4-091442	12 53 10.40	-09 14 41.9	4.59	5.58	0.05	1	21.60	23.4	-0.11	1.134	NLAGN	...	1686-4311	43.5	<	<	21.9	
J125311.1-091117	12 53 11.11	-09 11 17.5	1.20	11.80	0.55 ^h	1	20.28	23.4	-0.32	0.478	ELG	...	2571-6698	43.0	23.6	23.4	23.7	
J125312.6-090644	12 53 12.68	-09 06 44.0	3.42	6.02	-0.49	1	21.10	23.4	-0.28	0.000	star	...	3600-9500	
J125314.8-091300	12 53 14.83	-09 13 00.8	3.11	38.20	0.63	1	21.62	23.4	0.73	0.716	ELG	...	2097-5535	43.9	22.8	22.7	22.9	
J125315.2-091424	12 53 15.20	-09 14 24.3	4.47	30.20	0.66	1	23.82	23.4	1.51	1.154	NLAGN	...	1578-4178	44.2	23.2	23.1	23.2	
J125319.1-091116	12 53 19.13	-09 11 15.9	2.47	4.77	0.65 ^h	1	20.05	23.4	-0.80	0.478	ELG	...	2943-6292	42.6	22.9	22.7	23.1	
J125322.6-090246	12 53 22.64	-09 02 46.5	7.94	24.90	-0.22	1	16.69	23.4	-1.43	0.000	star	A	3870-10000	
J125323.2-090827	12 53 23.28	-09 08 27.3	3.60	18.90	0.44	1	21.93	23.4	0.55	0.503	ELG	...	2395-3759	43.2	22.7	22.6	22.8	
J125323.6-090429	12 53 23.63	-09 04 29.8	6.50	27.20	0.42	1	21.08	23.4	0.37	0.519	ELG	...	2601-6189	43.4	22.6	22.5	22.8	
J131653.0-291703	13 16 53.15	+29 17 04.7	7.94	16.40	-0.44	2	23.50	23.5	1.10	1.637	BLAGN	...	1338-3412	44.3	<	<	21.2	
J131654.1-291320	13 16 54.28	+29 13 22.5	4.98	15.60	-0.49	1	22.16	23.5	0.56	1.756	BLAGN	...	1415-3265	44.3	<	<	21.2	
J131654.6-291004	13 16 54.72	+29 10 06.2	3.85	31.00	0.06	1	22.15	23.5	0.85	0.908	ELG	...	2044-4848	44.0	22.4	22.3	22.4	
J131655.4-290753	13 16 55.58	+29 07 54.7	4.38	3.88	0.20	1	19.12	23.5	-1.26	0.262	ELG	...	2773-6537	41.9	21.5	20.8	21.8	
J131658.1-291017	13 16 58.29	+29 10 18.8	3.06	2.18	0.20	1	23.69	23.5	0.31	0.951	ELG	A	2075-4818	42.9	22.6	22.3	23.0	
J131700.2-291307	13 17 00.37	+29 13 08.6	3.84	4.12	-0.15	1	22.45	23.5	0.09	0.580	ELG	I	2215-5031	42.7	21.4	20.0	21.8	
J131701.2-290657	13 17 01.37	+29 06 58.6	4.12	8.85	-0.30	1	20.48	23.5	-0.36	0.491	BLAGN	J	2347-5264	42.9	20.9	<	21.3	
J131701.3-291432	13 17 01.51	+29 14 34.5	4.86	17.50	0.01	2	23.50	23.5	1.13	1.169	ELG	...	1613-3964	44.0	22.4	22.3	22.5	
J131706.0-290916	13 17 06.17	+29 09 18.2	1.69	40.00	-0.42	1	19.94	23.5	0.08	1.020	BLAGN	...	1881-4455	44.2	21.0	20.5	21.3	
J131706.2-291058	13 17 06.35	+29 10 59.8	1.46	2.29	0.50	1	20.51	23.5	-0.94	0.579	ELG	I	2216-5668	42.4	22.9	22.7	23.1	
J131708.6-291117	13 17 08.78	+29 11 19.0	1.25	6.62	0.49	1	19.80	23.5	-0.76	1.680	BLAGN	J	1380-3414	43.9	23.4	23.2	23.6	
J131713.8-291519	13 17 14.01	+29 15 21.2	5.04	3.94	0.64	1	19.36	23.5	-1.16	0.367	ELG	N	3108-6858	42.2	22.8	22.7	23.0	
J131714.5-291041	13 17 14.66	+29 10 42.7	0.64	3.80	-0.43	1	20.64	23.5	-0.66	2.702	BLAGN	J	945-2431	44.1	21.9	<	22.4	
J131714.7-290636	13 17 14.82	+29 06 37.8	3.74	4.60	-0.18	1	18.39	23.5	-1.48	0.181	ELG	...	2963-6591	41.6	20.3	<	21.1	
J131717.1-290639	13 17 17.26	+29 06 40.7	3.81	10.70	-0.15	1	19.57	23.5	-0.64	2.701	BLAGN	...	945-2107	44.5	22.6	22.3	22.8	
J131718.8-291111	13 17 19.01	+29 11 12.8	1.71	7.49	-0.30	1	21.98	23.5	0.17	0.803	BLAGN	H	2107-4991	43.3	<	<	21.2	
J131722.0-291124	13 17 22.12	+29 11 25.8	2.40	5.78	0.59	1	24.15	23.5	0.92	0.793	ELG	H	2230-5242	43.1	22.9	22.8	23.0	
J131727.4-290930	13 17 27.59	+29 09 32.0	3.43	4.63	0.87 ^h	1	22.05	23.5	-0.01	0.847	ELG	...	1894-4656	43.1	23.6	23.4	23.8	
J131729.7-290730	13 17 29.82	+29 07 32.0	4.74	15.50	-0.15	1	22.17	23.5	0.56	2.540	BLAGN	...	988-2175	44.6	22.5	22.3	22.7	
J131730.7-291055	13 17 30.86	+29 10 57.0	4.09	5.09	-0.46	1	21.74	23.5	-0.10	1.748	BLAGN	J	1410-3347	43.8	20.8	<	21.8	
J131730.8-291217	13 17 30.94	+29 12 19.4	4.53	3.60	0.45	1	22.56	23.5	0.08	0.830	ELG	...	1912-4453	43.0	22.9	22.8	23.1	
J131732.9-291055	13 17 33.06	+29 10 57.3	4.57	2.98	-0.19	1	21.61	23.5	-0.38	1.034	ELG	A	1769-3947	43.1	21.1	<	21.8	
J131733.4-290810	13 17 33.59	+29 08 12.2	5.11	8.84	-0.03	1	22.53	23.5	0.46	1.690	BLAGN	...	1301-2992	44.0	22.2	21.9	22.4	
J131736.5-291114	13 17 36.71	+29 11 15.7	5.40	8.44	-0.45	1	19.88	23.5	-0.62	1.958	BLAGN	...	1419-3177	44.1	21.8	20.8	22.1	
J131737.3-291524	13 17 37.50	+29 15 26.4	7.50	4.56	-0.43	1	22.81	23.5	0.28	5710-9400 ⁱ	
J131742.5-290911	13 17 42.67	+29 09 12.7	6.72	5.29	0.75 ^h	1	24.23	23.5	0.92	1.019	ELG	...	1733-4160	43.3	24.3	24.1	24.4	
J131745.2-291201	13 17 45.40	+29 12 02.7	7.42	4.56	0.70 ^h	1	22.34	23.5	0.09	0.715	ELG	...	2623-5481	42.9	24.0	23.7	24.1	
J131746.0-290912	13 17 46.16	+29 09 13.7	7.47	15.40	-0.32	1	19.64	23.5	-0.46	2.040	BLAGN	...	1151-2861	44.4	<	<	21.0	
J133730.8-292747	13 37 30.95	+29 27 48.4	6.56	8.62	-0.62	1	21.06	22.5	-0.14	1.428	BLAGN	...	1729-3871	43.9	<	<	20.9	
J133734.7-292830	13 37 34.85	+29 28 31.2	5.57	16.50	-0.30	1	21.53	22.5	0.33	0.830	BLAGN	...	2295-5136	43.6	20.6	<	21.4	
J133739.0-292712	13 37 39.17	+29 27 13.3	5.11	5.47	-0.37	1	20.76	22.5	-0.46	1.551	BLAGN	...	1646-3684	43.7	21.0	<	22.0	
J133741.8-292623	13 37 41.98	+29 26 24.1	5.05	53.20	-0.48	1	20.79	22.5	0.54	0.675	BLAGN	...	2507-5611	44.0	<	<	20.3	
J133744.1-292605	13 37 44.24	+29 26 06.5	4.89	12.10	-0.24	1	21.89	22.5	0.34	1.064	ELG	...	2034-4554	43.7	21.4	<	21.9	
J133744.2-293511	13 37 44.32	+29 35 12.9	6.56	22.70	-0.32	1	20.57	22.5	0.08	1.207	BLAGN	...	1585-4259	44.1	21.7	21.3	21.9	
J133753.0-293452	13 37 53.11	+29 34 53.2	5.49	9.28	-0.55	1	20.62	22.5	-0.28	1.610	BLAGN	...	1340-3601	44.0	<	<	21.4	
J133753.2-292433	13 37 53.35	+29 24 34.4	5.23	16.50	-0.49	1	19.90	22.5	-0.32	2.738	BLAGN	...	1123-2514	44.7	21.4	<	22.1	
J133755.4-293502	13 37 55.50	+29 35 03.7	5.54	29.90	0.22	1	22.25	22.5	0.88	0.426	ELG	L	3927-6591	43.3	22.5	22.4	22.6	
J133755.5-292745	13 37 55.65	+29 27 46.8	2.05	10.60	-0.66	1	19.52	22.5	-0.67	0.632	ALG	...	2573-5637	43.2	<	<	20.3	
J133757.9-292608	13 37 58.04	+29 26 10.0	3.46	11.30	-0.17	1	18.30	23.0	-1.13	0.304	ELG	...	3220-7131	42.5	21.4	20.9	21.5	

TABLE 2 — *Continued*

CXOEXSL_	X-ray Data						Optical Counterpart Data											
	α_x (J2000)	δ_x (J2000)	OAA	$S_{2-10}^{(-15)}$	HR	Flag	R	R_{limit}	$\log \frac{L_x}{L_{\odot}}$	z	Class	Notes	$\Delta\lambda_{\text{rest}}$	$\log L_x^{(2-10)}$	$\log N_{\text{H}}$	$\log N_{\text{H}}^-$	$\log N_{\text{H}}^+$	
(1)	(2) ^a	(3) ^a	(4)	(5)	(6) ^b	(7) ^c	(8)	(9)	(10)	(11)	(12) ^d	(13) ^e	(14) ^f	(15)	(16) ^g	(17) ^g	(18) ^g	
J133800.7+292927	13 38 00.82	+29 29 29.0	0.23	5.82	-0.05	2	23.00	23.0	0.45	0.853	ELG	...	2293–5072	43.2	22.3	22.0	22.5	
J133803.0+292825	13 38 03.11	+29 28 26.9	1.35	8.18	0.80	1	21.86	23.0	0.16	0.717	ELG	...	3261–5474	43.2	23.0	22.8	23.1	
J133803.6+292915	13 38 03.75	+29 29 16.7	0.89	10.10	0.76	1	22.46	23.0	0.49	1.001	NLAGN	...	2123–4622	43.6	23.0	22.8	23.2	
J133805.1+292422	13 38 05.22	+29 24 23.3	5.34	9.98	-0.59	1	20.38	23.0	-0.35	1.100	BLAGN	...	1809–4476	43.7	<	<	20.8	
J133807.0+292852	13 38 07.16	+29 28 53.9	1.72	4.31	0.70 ^h	2	23.00	23.0	0.32	0.375	ELG	...	2545–6836	42.3	23.0	22.7	23.2	
J133807.2+292734	13 38 07.39	+29 27 35.7	2.58	4.86	0.21	1	23.42	23.0	0.55	2.140	BLAGN	...	1114–2993	44.0	22.9	22.4	23.2	
J133808.8+293128	13 38 08.98	+29 31 29.6	2.73	13.50	0.48	1	22.95	22.5	0.81	1.322	ELG	...	1851–4026	44.0	23.3	23.2	23.4	
J133808.9+292412	13 38 09.06	+29 24 13.4	5.74	12.90	-0.50	1	19.64	23.0	-0.53	2.384	BLAGN	...	1241–2777	44.5	22.1	20.0	22.4	
J133810.9+293119	13 38 11.06	+29 31 20.1	2.98	25.70	-0.33	1	19.81	22.5	-0.17	2.032	BLAGN	...	1418–3100	44.7	20.3	<	21.6	
J133816.8+292350	13 38 16.98	+29 23 51.5	6.84	15.70	0.43	1	22.89	23.0	0.85	0.755	ELG	A	2905–5356	43.5	22.7	22.5	22.9	
J133825.7+292956	13 38 25.83	+29 29 57.9	5.65	13.70	0.85 ^h	1	23.18	23.0	0.91	0.983	NLAGN	...	2874–4538	43.7	23.4	23.2	23.7	
J133833.0+292908	13 38 33.15	+29 29 09.1	7.24	32.50	-0.18	1	20.12	23.0	0.06	0.000	star	D	3700–9000	
J133836.0+292940	13 38 36.15	+29 29 41.4	7.88	35.30	-0.14	1	20.42	23.0	0.22	0.469	ELG	...	3097–6296	43.4	21.6	21.4	21.8	
J141114.2+520630	14 11 14.26	+52 06 30.6	6.54	22.60	-0.38	1	19.76	21.9	-0.24	1.524	BLAGN	...	1545–3763	44.3	<	<	20.7	
J141119.4+521400	14 11 19.43	+52 14 00.5	1.56	30.90	-0.40	4	19.14	21.4	-0.35	1.279	BLAGN	...	1711–4168	44.3	<	<	20.0	
J141123.4+521331	14 11 23.40	+52 13 31.6	1.89	90.70	-0.51	1	19.05	21.4	0.08	0.472	BLAGN	H	2625–6793	43.8	<	<	<	
J141127.4+521131	14 11 27.38	+52 11 31.4	2.87	33.10	0.09	1	19.78	21.9	-0.07	0.451	ALG	HK	2412–6374	43.4	21.9	21.8	22.0	
J145143.6+430600	14 51 43.70	+43 06 00.4	6.73	38.50	-0.21	1	20.47	22.9	0.27	0.558	BLAGN	...	2278–5969	43.6	<	<	21.0	
J145149.0+430125	14 51 49.14	+43 01 25.2	4.23	86.90	0.09	1	20.38	22.9	0.59	1.150	BLAGN	...	1488–4418	44.7	20.9	<	21.3	
J145150.2+430801	14 51 50.25	+43 08 01.5	7.45	14.80	0.03	1	22.98	21.9	0.86	1.785	BLAGN	...	1256–3231	44.3	22.0	<	22.3	
J145151.2+430256	14 51 51.33	+43 02 56.6	4.00	25.90	-0.05	1	20.57	22.9	0.14	0.963	BLAGN	N	1782–4583	44.0	<	<	21.2	
J145156.1+431008	14 51 56.22	+43 10 08.7	8.90	65.10	-0.14	1	21.34	21.9	0.85	0.744	ELG	...	2379–5676	44.1	22.0	21.8	22.1	
J145200.2+430349	14 52 00.33	+43 03 49.3	3.01	10.80	0.09	1	21.64	22.9	0.19	1.548	BLAGN	N	1373–3649	44.0	21.9	<	22.4	
J145201.7+430640	14 52 01.75	+43 06 40.1	5.29	43.10	0.73	1	19.25	22.9	-0.17	0.279	BLAGN	N	2873–7427	43.0	22.8	22.7	23.0	
J145203.0+430542	14 52 03.13	+43 05 42.3	4.30	42.90	-0.44	1	20.67	22.9	0.40	1.609	BLAGN	...	1379–3641	44.7	21.6	20.8	21.9	
J145209.4+430101	14 52 09.48	+43 01 00.9	0.88	23.30	-0.15	1	21.76	22.9	0.57	1.340	BLAGN	...	1769–4102	44.2	21.7	21.3	21.9	
J145210.3+430525	14 52 10.35	+43 05 25.8	3.71	20.20	-0.44	1	20.51	22.9	0.01	1.385	BLAGN	...	1740–3983	44.2	21.9	21.4	22.1	
J145215.0+430439	14 52 15.07	+43 04 39.1	2.96	8.59	0.48	1	19.95	22.9	-0.59	0.346	ELG	...	2749–7431	42.5	22.7	22.4	23.0	
J145215.6+430448	14 52 15.66	+43 04 48.7	3.14	180.00	-0.41	1	17.91	22.9	-0.08	0.297	BLAGN	M	2853–7711	43.7	<	<	20.5	
J150925.5+565729	15 09 25.64	+56 57 29.3	6.75	18.00	-0.13	1	21.27	24.0	0.26	1.607	BLAGN	...	1814–3807	44.3	22.0	21.7	22.2	
J150929.9+570413	15 09 30.07	+57 04 13.6	4.21	13.90	-0.20	6	0.000	star	...	3500–5700	
J150934.1+570314	15 09 34.25	+57 03 14.5	3.37	3.47	-0.36	1	22.91	24.0	0.20	2.826	BLAGN	...	914–2404	44.1	22.7	22.4	22.9	
J150934.2+571006	15 09 34.33	+57 10 07.0	8.26	9.40	-0.24	1	20.54	24.0	-0.31	1.938	BLAGN	J	1242–3063	44.2	22.7 ^j	
J150935.7+570324	15 09 35.87	+57 03 25.1	3.20	8.60	-0.14	1	20.18	24.0	-0.49	0.310	BLAGN	...	2671–7099	42.4	21.7	21.5	21.8	
J150935.8+565922	15 09 35.91	+56 59 22.7	4.41	43.50	-0.02	1	21.48	24.0	0.73	0.681	BLAGN	...	2769–5883	43.9	21.7	21.5	21.8	
J150937.2+570507	15 09 37.28	+57 05 07.9	3.88	6.90	0.90 ^h	6	1.093	ELG	...	2675–4300	43.5	22.7	22.5	22.9	
J150941.1+565856	15 09 41.22	+56 58 56.2	4.30	4.64	-0.39	1	23.16	24.0	0.43	1.500	BLAGN	...	1954–4040	43.6	21.4	<	21.8	
J150945.8+570100	15 09 45.91	+57 01 00.4	2.30	8.36	-0.31	6	0.003	ELG	E	4596–9825	38.3	
J150946.6+565946	15 09 46.71	+56 59 46.9	3.19	4.89	0.04	6	0.002	ELG	E	4850–10079	37.7	
J150949.5+570000	15 09 49.65	+57 00 00.4	2.80	54.50	-0.31	6	1.458	ELG	K	1989–4119	44.7	21.5	21.4	21.7	
J150951.4+565928	15 09 51.50	+56 59 28.2	3.21	8.23	-0.03	1	21.37	24.0	-0.04	0.003	star	E	5029–10249	38.3	
J150953.2+570547	15 09 53.34	+57 05 48.1	3.33	3.66	-0.67	1	21.09	24.0	-0.50	0.806	BLAGN	...	1937–5121	43.0	<	<	20.0	
J150953.7+570048	15 09 53.80	+57 00 48.2	1.85	17.70	-0.32	1	22.35	24.0	0.69	1.973	BLAGN	...	1633–3393	44.5	21.4	20.9	21.6	
J150956.0+570534	15 09 56.14	+57 05 34.6	3.05	3.71	0.73	1	20.46	24.0	-0.75	0.150	ELG	A	3130–8173	41.4	22.6	22.3	22.7	
J151004.7+570038	15 10 04.83	+57 00 38.6	2.08	8.90	0.09	2	24.00	24.0	1.04	1.215	ELG	...	2334–4695	43.7	22.5	22.3	22.6	
J151008.4+570537	15 10 08.51	+57 05 37.6	3.37	21.10	0.92	1	20.62	24.0	0.07	0.272	ELG	...	2830–7272	42.7	23.0	23.0	23.1	
J151010.3+570609	15 10 10.44	+57 06 09.6	3.97	33.90	0.54	1	20.34	24.0	0.17	0.546	NLAGN	...	2328–6015	43.6	22.7	22.6	22.7	
J151013.3+570155	15 10 13.40	+57 01 56.1	2.12	3.35	0.35	2	24.00	24.0	0.61	0.101	ELG	...	3269–8628	41.0	22.2	22.1	22.4	
J151015.1+570341	15 10 15.26	+57 03 41.7	2.56	6.00	-0.37	1	23.23	24.0	0.57	1.303	BLAGN	...	2103–4363	43.6	<	<	20.5	
J151029.9+570513	15 10 30.03	+57 05 13.3	5.06	10.70	0.11	1	20.30	24.0	-0.35	0.536	ELG	...	3193–6484	43.0	22.3	22.2	22.4	
J151030.9+570014	15 10 30.99	+57 00 14.8	4.98	5.26	-0.25	1	22.93	24.0	0.39	1.943	BLAGN	N	1427–3160	43.9	20.7	<	21.7	
J151044.8+570340	15 10 44.89	+57 03 40.6	6.41	23.00	0.78	1	24.26	24.0	1.57	1.531	NLAGN	...	1422–3318	44.4	23.7	23.6	23.8	
J152132.9+074856	15 21 33.02	+07 48 56.1	6.95	9.78	-0.47	1	21.29	23.4	0.01	1.539	BLAGN	...	1963–3938	44.0	20.8	<	21.7	

TABLE 2 — *Continued*

CXOEXSL (1)	X-ray Data						Optical Counterpart Data											
	α_x (J2000) (2) ^a	δ_x (J2000) (3) ^a	OAA (4)	$S_{2-10}^{(-15)}$ (5)	HR (6) ^b	Flag (7) ^c	R (8)	R_{limit} (9)	$\log \frac{L_x}{L_{\odot}}$ (10)	z (11)	Class (12) ^d	Notes (13) ^e	$\Delta\lambda_{\text{rest}}$ (14) ^f	$\log L_x^{(2-10)}$ (15)	$\log N_{\text{H}}$ (16) ^g	$\log N_{\text{H}}^-$ (17) ^g	$\log N_{\text{H}}^+$ (18) ^g	
J152135.0+074836	15 21 35.08	+07 48 36.7	6.35	9.41	-0.52	1	20.93	23.4	-0.15	1.513	BLAGN	...	2001-4058	44.0	<	<	21.3	
J152151.4+074826	15 21 51.50	+07 48 26.3	3.34	14.70	-0.44	1	18.88	23.4	-0.78	2.049	BLAGN	...	1626-3345	44.4	21.7	20.5	22.0	
J152151.6+074651	15 21 51.72	+07 46 51.8	1.99	10.20	-0.51	1	17.63	23.4	-1.44	0.000	star	...	5365-10500	
J152156.3+074809	15 21 56.41	+07 48 09.1	2.75	10.50	0.07	1	17.73	23.4	-1.39	0.267	ALG	...	3946-7892	42.4	22.1	21.9	22.2	
J152158.2+074832	15 21 58.29	+07 48 32.2	3.14	3.73	-0.19	1	21.92	23.4	-0.16	0.632	ALG	K	2993-6188	42.7	22.4	22.2	22.6	
J152207.5+074528	15 22 07.56	+07 45 28.1	2.57	12.50	-0.39	1	21.30	22.9	0.12	5580-10500 ⁱ	
J152218.4+074916	15 22 18.48	+07 49 16.8	6.54	14.10	-0.41	1	21.49	22.9	0.25	1.027	BLAGN	...	2217-4686	43.8	21.3	<	21.7	
J152227.2+074833	15 22 27.32	+07 48 33.1	8.10	38.40	0.04	1	21.90	22.9	0.84	0.998	BLAGN	...	2489-4604	44.2	22.2	22.0	22.3	
J162252.1+263852	16 22 52.28	+26 38 52.3	7.89	19.00	-0.38	1	20.83	22.4	0.11	0.815	NLAGN	...	2947-5757	43.7	21.2	<	21.6	
J162255.0+263720	16 22 55.12	+26 37 20.4	6.89	18.30	-0.01	1	21.41	22.4	0.33	1.017	BLAGN	A	2456-4923	43.9	21.8	<	22.1	
J162256.7+264103	16 22 56.83	+26 41 02.9	8.03	18.50	0.43	4	21.70	22.4	0.45	0.690	ELG	...	3340-6213	43.5	22.8	22.6	23.0	
J162300.1+263755	16 23 00.22	+26 37 55.2	5.91	35.20	-0.42	4	17.36	22.4	-1.01	0.091	ELG	...	4472-9165	41.9	<	<	20.3	
J162305.6+263918	16 23 05.71	+26 39 18.2	5.40	9.07	0.62	1	22.09	23.9	0.29	0.929	ELG	...	2584-5287	43.5	23.1	22.9	23.3	
J162315.4+263506	16 23 15.56	+26 35 06.3	2.48	5.14	-0.43	1	20.96	23.9	-0.41	0.425	ELG	...	3185-6866	42.5	21.6	20.9	21.9	
J162327.2+263207	16 23 27.30	+26 32 07.3	4.10	19.90	-0.23	4	19.38	24.4	-0.45	1.438	BLAGN	K	2255-4388	44.2	21.5	<	21.9	
J162328.0+264034	16 23 28.15	+26 40 33.7	4.39	16.20	0.61	1	23.92	23.9	1.28	0.951	ELG	...	2275-4971	43.8	23.2	23.0	23.3	
J162331.9+264125	16 23 31.99	+26 41 25.6	5.42	8.60	0.07	1	21.96	23.9	0.22	1.575	BLAGN	...	1759-3782	44.0	22.9	22.6	23.1	
J162333.9+263525	16 23 34.01	+26 35 25.0	2.06	7.06	-0.09	1	21.88	23.9	0.10	4805-9500 ⁱ	
J162335.9+263652	16 23 36.07	+26 36 52.5	2.45	11.40	-0.30	1	22.81	23.9	0.68	4450-9570 ^j	
J162343.7+263244	16 23 43.79	+26 32 44.6	5.36	122.00	-0.35	1	19.15	23.9	0.25	0.659	BLAGN	...	3408-6389	44.3	20.7	<	21.0	
J162345.7+263335	16 23 45.88	+26 33 34.9	5.26	16.70	0.47	1	21.63	23.9	0.37	1.283	ELG	K	2492-4485	44.1	23.4	23.2	23.5	
J170318.8+514319	17 03 18.96	+51 43 20.3	8.64	14.40	-0.55	1	20.52	22.9	-0.13	0.305	ELG	...	2681-7662	42.6	< ^j	
J170320.5+514602	17 03 20.62	+51 46 02.9	7.77	11.70	-0.23	1	21.06	22.9	-0.01	0.957	ELG	...	1788-5033	43.6	22.2 ^j	
J170321.8+514526	17 03 21.88	+51 45 27.3	7.64	20.00	-0.23	1	18.39	22.9	-0.84	0.259	ELG	...	2779-7942	42.6	21.7 ^j	
J170323.2+514240	17 03 23.31	+51 42 40.8	8.31	23.00	0.75 ^h	1	18.28	22.9	-0.83	0.297	ELG	...	2698-7710	42.8	22.8 ^{jk}	
J170334.5+514207	17 03 34.66	+51 42 08.3	7.13	9.86	0.23	2	22.90	22.9	0.66	4000-9400 ⁱ	
J170342.4+514847	17 03 42.49	+51 48 48.5	4.90	27.40	-0.47	1	20.13	22.9	-0.01	1.476	BLAGN	N	1413-3634	44.4	<	<	20.3	
J170343.8+514707	17 03 43.94	+51 47 08.1	4.18	18.50	-0.49	1	21.83	22.9	0.50	0.967	BLAGN	...	1779-5083	43.8	<	<	20.7	
J170348.8+514454	17 03 48.94	+51 44 55.3	3.76	26.50	-0.53	1	19.99	22.9	-0.08	1.091	BLAGN	N	2068-4782	44.1	<	<	20.0	
J170352.5+515340	17 03 52.65	+51 53 40.9	7.63	14.70	0.73 ^h	1	18.59	22.9	-0.90	0.297	ELG	...	3084-7710	42.6	24.7	24.1	26.3	
J170355.1+514935	17 03 55.17	+51 49 36.5	3.87	10.40	-0.16	1	21.24	22.9	0.01	0.631	BLAGN	...	2145-6131	43.2	21.8	21.6	22.0	
J170355.8+514949	17 03 55.89	+51 49 49.7	3.98	29.40	-0.23	1	20.66	22.9	0.23	0.670	BLAGN	...	2095-5988	43.7	<	<	20.6	
J170400.9+515515	17 04 01.03	+51 55 15.6	8.81	21.60	-0.27	1	20.64	22.9	0.09	1.974	BLAGN	...	1176-3093	44.6	22.5	22.2	22.6	
J170402.8+514247	17 04 02.92	+51 42 48.4	3.96	6.93	-0.49	1	21.76	22.9	0.04	1.426	BLAGN	A	1236-3998	43.8	21.4	<	21.9	
J170403.3+514756	17 04 03.44	+51 47 57.1	1.78	12.60	-0.26	1	19.74	22.9	-0.50	4.270	BLAGN	...	721-1802	45.0	<	<	22.0	
J170403.3+514854	17 04 03.46	+51 48 54.9	2.60	13.30	-0.08	1	22.85	22.9	0.76	1.806	BLAGN	...	1318-3385	44.3	<	<	21.1	
J170407.4+514957	17 04 07.47	+51 49 57.6	3.42	8.03	0.11	1	22.56	22.9	0.43	0.693	ELG	...	2362-5906	43.2	22.7	22.5	22.8	
J170416.4+514306	17 04 16.55	+51 43 07.2	3.57	6.83	-0.44	1	21.02	22.9	-0.26	1.962	BLAGN	...	1114-3207	44.1	<	<	21.7	
J170419.1+514233	17 04 19.24	+51 42 33.9	4.22	11.00	0.03	1	23.59	22.9	0.98	1.049	ALG	...	1781-4880	43.7	22.5	22.3	22.7	
J170421.9+514403	17 04 21.99	+51 44 03.6	3.06	15.90	-0.27	1	20.76	22.9	0.01	1.915	BLAGN	N	1166-3327	44.4	22.2	22.0	22.4	
J170423.0+514321	17 04 23.14	+51 43 22.2	3.74	8.82	-0.05	1	19.83	22.9	-0.62	0.325	ELG	...	2792-7547	42.5	21.9	21.6	22.1	
J170425.1+514716	17 04 25.22	+51 47 16.7	2.35	11.50	-0.07	2	22.90	22.9	0.73	2.220	BLAGN	...	1086-2950	44.4	21.6	<	22.0	
J171600.9+670807	17 16 01.02	+67 08 06.7	6.85	8.68	-0.36	1	22.46	24.4	0.42	1.714	BLAGN	...	1470-3316	44.0	22.1	21.6	22.4	
J171613.3+671133	17 16 13.40	+67 11 32.2	4.62	14.40	-0.31	1	22.99	23.9	0.85	1.584	BLAGN	J	1393-3482	44.2	22.5	22.4	22.7	
J171614.4+671344	17 16 14.52	+67 13 43.5	4.94	12.90	-0.00	1	23.07	23.9	0.84	1.133	BLAGN	...	2625-4406	43.8	22.2	21.9	22.4	
J171621.3+671312	17 16 21.39	+67 13 11.3	4.12	4.92	-0.43	1	21.13	23.9	-0.36	1.081	BLAGN	...	1729-4469	43.4	22.3	21.9	22.4	
J171624.7+671239	17 16 24.81	+67 12 38.2	3.63	6.65	0.08	1	23.99	23.9	0.92	3.417	NLAGN	...	837-1924	44.5	23.5	23.1	23.8	
J171635.5+671626	17 16 35.62	+67 16 24.9	5.31	21.30	-0.19	1	20.19	23.9	-0.10	0.501	BLAGN	...	2331-6195	43.3	20.9	<	21.3	
J171636.9+670829	17 16 36.99	+67 08 28.5	3.99	38.60	0.72	1	22.00	24.4	0.89	0.795	ELG	H	2005-5236	44.0	23.3	23.2	23.4	
J171637.9+671307	17 16 38.03	+67 13 06.4	2.63	18.00	0.38	1	23.27	23.9	1.06	1.272	NLAGN	...	1716-3807	44.1	23.2	23.0	23.2	
J171638.0+671155	17 16 38.17	+67 11 54.7	2.23	9.85	-0.43	1	22.92	23.9	0.66	1.326	BLAGN	J	1590-3869	43.9	21.5	<	21.8	
J171639.7+671640	17 16 39.88	+67 16 39.2	5.35	12.10	0.87 ^h	1	23.36	23.9	0.93	1.275	NLAGN	...	1604-3846	43.9	24.0	23.9	24.2	

TABLE 2 — *Continued*

CXOEXSL (1)	X-ray Data						Optical Counterpart Data											
	α_x (J2000) (2) ^a	δ_x (J2000) (3) ^a	OAA (4)	$S_{2-10}^{(-15)}$ (5)	HR (6) ^b	Flag (7) ^c	R (8)	R_{limit} (9)	$\log \frac{L_x}{L_{\odot}}$ (10)	z (11)	Class (12) ^d	Notes (13) ^e	$\Delta\lambda_{\text{rest}}$ (14) ^f	$\log L_x^{(2-10)}$ (15)	$\log N_{\text{H}}$ (16) ^g	$\log N_{\text{H}}^-$ (17) ^g	$\log N_{\text{H}}^+$ (18) ^g	
J171651.7+670855	17 16 51.81	+67 08 53.8	2.95	30.80	0.03	2	23.90	23.9	1.55	2.067	NLAGN	...	1206–2771	44.8	23.1	23.0	23.2	
J171652.0+671508	17 16 52.12	+67 15 07.7	3.52	4.22	−0.33	1	22.84	23.9	0.26	1.800	BLAGN	J	1367–2857	43.8	21.7	<	22.2	
J171700.6+670520	17 17 00.77	+67 05 18.9	6.40	24.70	−0.40	1	20.68	24.4	0.16	1.147	BLAGN	...	1630–4191	44.1	<	<	21.1	
J171703.8+670900	17 17 03.90	+67 08 58.8	2.75	4.32	0.58	4	21.79	23.9	−0.15	0.812	ELG	H	2378–5118	43.0	23.2	22.5	24.1	
J171713.4+671433	17 17 13.50	+67 14 32.7	3.08	104.00	0.03	1	21.66	23.9	1.18	1.811	BLAGN	...	1316–3201	45.2	23.0	23.0	23.1	
J171714.5+671136	17 17 14.65	+67 11 35.0	1.32	5.77	0.62	1	22.68	23.9	0.33	0.815	ELG	...	1983–5509	43.2	23.0	22.8	23.2	
J171715.1+671217	17 17 15.23	+67 12 15.8	1.48	3.37	0.67 ^h	2	23.90	23.9	0.59	1.340	ELG	...	1623–4017	43.4	23.8	23.5	24.1	
J171724.7+670913	17 17 24.81	+67 09 11.9	3.41	3.65	0.16	1	17.16	23.9	−2.07	0.138	ELG	...	3075–8347	41.3	21.5	20.6	21.8	
J171725.3+670616	17 17 25.39	+67 06 15.6	5.94	16.30	−0.29	1	21.30	24.4	0.23	1.814	BLAGN	...	1279–3020	44.4	<	<	21.2	
J171731.9+670934	17 17 32.01	+67 09 33.7	3.69	6.03	0.48	1	23.36	23.9	0.62	2.850	NLAGN	...	935–2337	44.3	23.5	23.2	23.7	
J171740.6+671147	17 17 40.76	+67 11 46.1	3.85	6.10	−0.56	1	21.83	23.9	0.02	2.313	BLAGN	A	1109–2867	44.2	22.6	22.3	22.9	
J171747.4+671449	17 17 47.58	+67 14 48.3	5.46	7.63	0.10	1	22.91	22.9	0.55	0.846	ELG	A	2166–5146	43.3	22.8	22.7	23.0	
J171748.5+670545	17 17 48.59	+67 05 43.9	7.55	26.50	−0.48	1	19.74	24.4	−0.18	0.480	BLAGN	...	2364–6081	43.3	<	<	20.8	
J171758.4+671203	17 17 58.56	+67 12 01.9	5.58	37.20	−0.38	1	20.87	23.9	0.42	1.808	BLAGN	...	1246–3205	44.7	21.5	20.3	21.8	
J171806.0+671219	17 18 06.11	+67 12 18.1	6.33	6.71	−0.38	1	22.56	23.9	0.35	0.840	ELG	...	1956–5027	43.3	21.2	<	21.7	
J171807.6+670647	17 18 07.73	+67 06 45.9	8.15	45.40	−0.38	1	21.75	23.9	0.86	0.797	BLAGN	...	2114–4730	44.0	<	<	20.8	
J171837.5+671351	17 18 37.62	+67 13 50.1	9.59	13.80	−0.44	1	20.56	22.9	−0.14	1.540	BLAGN	J	1417–3346	44.1	20.3	<	21.8	
J171838.3+671309	17 18 38.42	+67 13 08.6	9.54	17.80	0.16	1	22.14	23.9	0.61	0.000	star	...	5600–9200	
J171859.5+671443	17 18 59.67	+67 14 42.7	11.87	52.70	−0.37	1	20.40	22.4	0.38	1.147	BLAGN	...	1676–3959	44.5	<	<	20.8	
J175745.4+664112	17 57 45.50	+66 41 12.2	5.12	14.70	0.68	1	20.32	22.9	−0.20	0.680	ELG	K	3133–5636	43.4	23.1	23.0	23.2	
J175812.1+664252	17 58 12.20	+66 42 52.7	4.71	12.50	0.12	2	22.90	22.9	0.75	2.750	NLAGN	...	1488–2800	44.6	23.5	23.4	23.7	
J175823.5+663950	17 58 23.65	+66 39 50.7	1.47	14.00	−0.45	1	19.66	22.9	−0.49	0.995	BLAGN	K	2513–5130	43.7	21.0	20.3	21.3	
J175859.6+663729	17 58 59.69	+66 37 29.8	3.17	3.78	0.81 ^h	2	22.90	22.9	0.23	4870–10100 ⁱ	
J175911.9+663512	17 59 12.04	+66 35 12.3	5.36	45.90	−0.29	1	20.46	22.9	0.35	1.922	BLAGN	...	1519–3319	44.9	21.6	21.4	21.7	
J175928.1+663851	17 59 28.21	+66 38 51.5	5.84	20.70	−0.33	1	20.22	22.9	−0.10	4.328	BLAGN	A	1036–2016	45.2	<	<	21.9	
J175947.3+663552	17 59 47.42	+66 35 53.0	8.17	14.70	0.08	1	23.08	22.9	0.90	0.838	ELG	...	2725–5505	43.6	22.6 ^l	
J204359.5+771417	20 43 59.58	+77 14 17.6	2.87	5.58	0.71 ^h	1	22.15	21.4	0.11	0.807	ELG	...	2855–5755	43.1	23.6	23.3	23.8	
J204411.3+771427	20 44 11.43	+77 14 27.6	3.15	10.30	−0.26	1	22.75	21.4	0.61	1.023	ELG	...	2469–5042	43.6	21.9	21.4	22.1	
J204412.5+771927	20 44 12.65	+77 19 28.1	3.54	12.70	0.31	1	18.30	21.4	−1.08	0.366	ELG	...	3715–7503	42.7	22.2	22.0	22.3	
J204420.5+772039	20 44 20.65	+77 20 39.7	4.76	11.10	0.59	2	21.40	21.4	0.11	5230–9750 ⁱ	
J204430.7+771215	20 44 30.81	+77 12 15.4	5.53	9.68	−0.63	1	20.77	21.4	−0.21	0.768	ELG	A	2641–5599	43.3	<	<	20.7	
J204433.8+772049	20 44 33.93	+77 20 50.0	5.33	50.70	−0.08	1	20.16	21.4	0.27	0.816	BLAGN	...	2813–5214	44.1	21.8	21.7	21.9	
J204441.1+771146	20 44 41.26	+77 11 46.4	6.26	8.62	0.69 ^h	1	22.95	21.4	0.62	4510–9735 ⁱ	
J205531.8+043101	20 55 31.94	−04 31 02.3	12.18	36.70	−0.94	3	10.74	22.8	−3.64	0.000	star	B	
J205558.2+043340	20 55 58.27	−04 33 40.7	5.18	13.30	−0.23	1	19.27	23.8	−0.67	1.676	BLAGN	...	1765–3714	44.2	22.2	21.8	22.4	
J205601.1+042955	20 56 01.25	−04 29 55.5	6.36	9.60	0.75 ^h	1	20.68	22.8	−0.25	5435–10000 ⁱ	
J205602.0+043644	20 56 02.08	−04 36 45.2	4.70	12.10	0.79	1	21.21	23.8	0.07	0.467	NLAGN	...	2215–6816	43.0	23.7	23.5	23.9	
J205603.0+043613	20 56 03.14	−04 36 14.0	4.24	11.40	0.25	1	20.32	23.8	−0.32	0.469	ELG	...	2314–6398	42.9	22.5	22.3	22.6	
J205603.1+043848	20 56 03.24	−04 38 48.8	5.75	11.60	0.72	1	23.66	23.8	1.03	1.395	ELG	...	1908–4085	44.0	23.7	23.5	23.8	
J205603.6+043117	20 56 03.68	−04 31 17.5	4.98	11.00	−0.60	1	20.57	23.8	−0.23	1.477	BLAGN	...	1251–5248	44.0	<	<	21.1	
J205604.1+043149	20 56 04.26	−04 31 49.4	4.53	8.60	−0.12	1	23.98	23.8	1.03	1.902	BLAGN	K	1309–3273	44.1	21.8	<	22.7	
J205605.5+044058	20 56 05.57	−04 40 58.4	7.21	33.30	−0.28	1	20.80	23.8	0.34	0.801	BLAGN	...	2501–5391	43.9	20.9	<	21.4	
J205606.1+043329	20 56 06.17	−04 33 29.6	3.31	6.62	−0.43	1	22.55	23.8	0.34	5225–10400 ⁱ	
J205606.6+043725	20 56 06.75	−04 37 25.7	4.15	16.80	−0.55	1	19.56	23.8	−0.45	1.190	BLAGN	...	2239–4611	44.0	<	<	21.3	
J205608.1+043210	20 56 08.21	−04 32 11.0	3.54	7.32	0.42	1	22.24	23.8	0.26	0.731	ELG	A	2108–5488	43.2	22.3	21.9	22.7	
J205608.9+043539	20 56 08.99	−04 35 39.4	2.67	7.95	0.51	1	20.75	23.8	−0.30	1.435	BLAGN	...	2141–4271	43.8	22.3	21.0	23.1	
J205609.3+043832	20 56 09.46	−04 38 32.8	4.62	10.40	−0.12	1	20.44	23.8	−0.31	0.398	BLAGN	...	3551–7296	42.7	21.6	21.1	21.8	
J205609.5+043728	20 56 09.62	−04 37 29.1	3.71	23.60	−0.27	1	17.86	23.8	−0.98	0.000	star	...	5075–10300	
J205614.9+044135	20 56 14.99	−04 41 35.9	7.11	9.51	−0.53	1	21.33	23.8	0.01	2.478	BLAGN	...	1434–2903	44.4	22.2	<	22.5	
J205618.6+043429	20 56 18.74	−04 34 29.5	0.06	28.90	0.78	1	21.52	22.3	0.57	0.529	NLAGN	...	2288–6212	43.5	23.0	22.9	23.1	
J205622.2+044005	20 56 22.29	−04 40 06.2	5.62	28.60	−0.35	1	20.67	23.8	0.22	0.641	ELG	...	3397–6398	43.6	<	<	20.9	
J205624.7+043533	20 56 24.84	−04 35 34.2	1.83	32.20	0.89	1	19.40	23.8	−0.23	0.260	ELG	...	2777–7936	42.8	23.3	23.1	23.4	

TABLE 2 — *Continued*

CXOEXSL (1)	X-ray Data						Optical Counterpart Data											
	α_x (J2000) (2) ^a	δ_x (J2000) (3) ^a	OAA (4)	$S_{2-10}^{(-15)}$ (5)	HR (6) ^b	Flag (7) ^c	R (8)	R_{limit} (9)	$\log \frac{L_x}{L_{\odot}}$ (10)	z (11)	Class (12) ^d	Notes (13) ^e	$\Delta\lambda_{\text{rest}}$ (14) ^f	$\log L_x^{(2-10)}$ (15)	$\log N_{\text{H}}$ (16) ^g	$\log N_{\text{H}}^-$ (17) ^g	$\log N_{\text{H}}^+$ (18) ^g	
J205628.8-043521	20 56 28.87	-04 35 22.1	2.65	4.84	-0.27	1	19.83	22.3	-0.88	0.262	ELG	...	2694-7450	42.0	21.2	<	21.6	
J205629.1-043415	20 56 29.23	-04 34 16.2	2.63	7.82	-0.62	1	21.29	22.3	-0.09	1.035	BLAGN	...	1769-4422	43.5	20.5	<	21.4	
J205631.3-043614	20 56 31.46	-04 36 14.7	3.59	21.10	-0.23	1	21.92	23.8	0.59	0.953	BLAGN	...	1740-4608	43.9	21.3	<	21.6	
J205635.1-043944	20 56 35.27	-04 39 45.2	6.63	23.00	0.89 ^h	1	22.35	23.8	0.80	0.732	ELG	...	2020-5773	43.7	23.4	23.3	23.6	
J205636.7-043950	20 56 36.84	-04 39 50.5	6.95	9.54	-0.31	1	23.10	23.8	0.72	1.536	BLAGN	...	1380-3667	44.0	22.3	22.1	22.5	
J205638.1-043753	20 56 38.18	-04 37 53.7	5.88	18.90	-0.48	1	19.21	23.8	-0.54	2.974	BLAGN	...	962-2491	44.9	22.4	22.0	22.6	
J224638.3+034124	22 46 38.37	+03 41 23.2	12.02	36.60	-0.44	1	20.65	23.4	0.32	1.110	BLAGN	K	2665-4976	44.3	21.6	21.4	21.8	
J224649.9+033937	22 46 50.02	+03 39 36.2	9.03	15.60	0.55	1	20.44	23.4	-0.13	0.533	ELG	K	3496-6849	43.2	22.8 ^l	
J224703.1+034350	22 47 03.17	+03 43 49.6	6.95	9.98	0.74 ^h	1	19.78	23.4	-0.59	0.367	ELG	N	3785-7534	42.6	23.6	23.2	23.9	
J224706.0+033951	22 47 06.09	+03 39 50.8	5.02	77.10	0.62	1	20.01	23.4	0.39	0.452	BLAGN	...	3133-6749	43.7	22.9	22.8	22.9	
J224707.5+034629	22 47 07.62	+03 46 28.1	8.02	9.87	0.31	1	22.02	23.4	0.30	0.840	ELG	...	2491-5095	43.4	23.0	22.8	23.1	
J224708.7+033619	22 47 08.80	+03 36 18.8	5.65	14.40	-0.19	2	23.40	23.4	1.00	5090-10300 ^j	
J224710.2+033657	22 47 10.34	+03 36 56.4	4.96	11.70	-0.24	2	23.40	23.4	0.91	0.972	ELG	K	2487-5121	43.6	22.2	21.9	22.3	
J224710.5+033738	22 47 10.64	+03 37 37.3	4.51	4.57	0.54	2	23.40	23.4	0.50	3.335	NLAGN	...	1098-2306	44.3	24.1	23.9	24.3	
J224712.0+034124	22 47 12.10	+03 41 23.7	3.81	18.80	0.49	2	23.40	23.4	1.11	1.248	ELG	K	2355-4679	44.1	23.3	23.2	23.4	
J224716.7+034127	22 47 16.75	+03 41 26.5	2.80	31.90	-0.32	1	19.27	23.4	-0.29	0.264	BLAGN	...	4022-8164	42.8	20.9	<	21.2	
J224716.9+033432	22 47 17.02	+03 34 31.2	5.87	58.90	-0.37	1	21.32	23.4	0.80	3.818	BLAGN	...	1040-2117	45.6	22.1	21.3	22.4	
J224717.4+033230	22 47 17.45	+03 32 29.1	7.75	19.30	0.10	1	23.53	23.4	1.20	1.046	ELG	...	2727-4936	43.9	22.8	22.6	22.9	
J224718.7+033651	22 47 18.81	+03 36 50.5	3.59	18.50	0.93 ^h	1	23.00	23.4	0.97	1.288	NLAGN	...	1975-4254	44.1	23.7	23.6	23.8	
J224720.5+033249	22 47 20.61	+03 32 48.6	7.25	11.70	0.41	1	23.17	23.4	0.84	0.608	ELG	...	3420-6082	43.2	22.6	22.4	22.8	
J224722.2+034319	22 47 22.33	+03 43 18.0	3.51	12.70	-0.22	1	22.48	23.4	0.60	1.251	ELG	...	1974-4309	43.9	21.9	21.6	22.2	
J224729.5+033916	22 47 29.57	+03 39 15.5	1.07	5.62	0.09	1	22.85	23.4	0.39	1.065	ELG	...	2397-4891	43.4	22.7	22.4	22.9	
J224729.8+034559	22 47 29.86	+03 45 58.4	6.12	38.00	-0.53	1	18.73	23.4	-0.43	1.315	BLAGN	...	2051-4241	44.4	21.0	<	21.5	
J224729.8+034232	22 47 29.93	+03 42 31.1	2.76	11.50	0.40	2	23.40	23.4	0.90	5515-8095 ⁱ	
J224731.1+034709	22 47 31.22	+03 47 08.0	7.32	32.50	0.77	1	21.16	23.4	0.48	0.540	ELG	K	2938-6090	43.5	23.1	23.1	23.2	
J224731.6+033550	22 47 31.74	+03 35 49.1	4.33	17.00	-0.46	1	20.85	23.4	0.07	0.997	BLAGN	...	2759-5307	43.8	21.3	20.3	21.6	
J224732.0+033859	22 47 32.09	+03 38 58.1	1.75	4.97	-0.14	1	21.78	23.4	-0.09	2.154	BLAGN	...	1141-2694	44.0	22.3	21.2	22.7	
J224732.2+033818	22 47 32.26	+03 38 17.6	2.22	5.53	-0.12	1	21.05	23.4	-0.34	0.708	ELG	...	2936-5971	43.0	21.6	<	22.3	
J224734.1+033510	22 47 34.15	+03 35 09.3	5.16	22.00	0.23	1	22.23	23.4	0.73	0.711	ELG	...	3226-6136	43.6	22.5	22.4	22.6	
J224734.2+033608	22 47 34.28	+03 36 07.7	4.30	24.40	0.86	1	22.04	23.4	0.70	0.647	ELG	...	3242-6376	43.6	23.3	23.2	23.5	
J224735.4+034005	22 47 35.52	+03 40 04.6	2.33	8.94	0.11	1	22.62	23.4	0.50	4535-9755 ⁱ	
J224737.6+033645	22 47 37.68	+03 36 44.7	4.28	5.82	-0.47	1	23.51	23.4	0.67	1.775	BLAGN	...	1261-3063	43.9	21.8	<	22.2	
J224739.0+034129	22 47 39.13	+03 41 28.8	3.58	24.50	-0.19	1	23.23	23.4	1.18	0.767	ELG	...	3084-5998	43.7	22.1	21.9	22.3	
J224739.1+034416	22 47 39.19	+03 44 15.2	5.41	42.60	-0.56	1	19.18	23.4	-0.20	0.962	BLAGN	...	2464-5096	44.2	<	<	20.3	
J224744.5+034314	22 47 44.55	+03 43 13.9	5.65	7.86	-0.15	1	21.80	23.4	0.12	1.319	BLAGN	K	2104-4355	43.8	22.7	22.5	22.9	
J224745.3+033740	22 47 45.40	+03 37 39.7	5.30	10.10	-0.46	1	21.63	23.4	0.16	1.427	BLAGN	...	1918-3887	43.9	<	<	21.5	
J224745.9+033630	22 47 46.04	+03 36 29.8	6.02	6.42	-0.07	1	24.83	23.4	1.24	5145-9340 ⁱ	
J234757.9+010328	23 47 57.95	+01 03 28.9	7.01	8.82	-0.02	1	19.91	23.4	-0.59	0.248	ELG	...	4046-8213	42.2	21.9	21.6	22.2	
J234759.5+010122	23 47 59.53	+01 01 22.9	5.41	11.30	-0.02	1	24.19	23.4	1.23	1.325	BLAGN	G	1952-4204	43.9	22.2	22.0	22.4	
J234806.5+010351	23 48 06.57	+01 03 51.5	5.99	14.80	-0.27	2	23.40	23.4	1.04	5300-10500 ⁱ	
J234806.6+010043	23 48 06.61	+01 00 44.1	3.58	7.95	-0.24	1	20.70	23.4	-0.32	0.768	BLAGN	...	1979-5260	43.3	<	<	21.2	
J234808.0+005812	23 48 08.00	+00 58 13.1	2.56	6.69	0.17	1	22.37	23.4	0.27	2.792	BLAGN	J	949-2241	44.4	23.2	22.9	23.4	
J234808.4+010111	23 48 08.40	+01 01 12.1	3.56	16.80	-0.10	1	22.96	23.4	0.91	1.425	BLAGN	K	1917-4082	44.2	20.0	<	21.5	
J234811.5+005700	23 48 11.55	+00 57 00.7	2.29	12.30	-0.59	1	21.45	23.4	0.17	1.820	BLAGN	...	1241-3191	44.2	<	<	20.3	
J234812.7+005750	23 48 12.73	+00 57 50.6	1.55	16.40	-0.37	1	23.36	23.4	1.06	1.040	BLAGN	...	1789-4166	43.9	20.6	<	21.0	
J234812.8+010022	23 48 12.89	+01 00 22.7	2.20	26.40	-0.44	1	20.92	23.4	0.29	0.718	BLAGN	...	2639-5681	43.7	20.8	<	21.2	
J234813.2+005611	23 48 13.27	+00 56 11.9	2.69	14.30	0.81	1	21.24	23.4	0.15	0.550	NLAGN	...	2322-5806	43.2	23.1	23.0	23.2	
J234813.7+005639	23 48 13.78	+00 56 40.2	2.22	7.24	0.60	1	20.48	23.4	-0.45	1.031	BLAGN	...	1723-4529	43.5	23.0	22.8	23.4	
J234814.4+010312	23 48 14.46	+01 03 12.8	4.70	13.60	-0.47	1	23.06	23.4	0.86	1.388	BLAGN	...	2206-4396	44.0	22.1	21.9	22.3	
J234815.3+010139	23 48 15.33	+01 01 39.8	3.14	10.60	0.93 ^h	1	25.94	23.4	1.90	4900-10100 ^j	
J234818.4+005520	23 48 18.47	+00 55 21.0	3.26	3.93	0.04	1	22.96	23.4	0.28	0.957	ELG	...	1839-4726	43.2	22.6	22.4	22.6	
J234818.9+005950	23 48 18.94	+00 59 50.4	1.25	15.10	-0.45	1	21.80	23.4	0.40	1.930	BLAGN	...	1194-2901	44.4	<	<	20.5	

TABLE 2 — *Continued*

CXOEXSL_	X-ray Data					Optical Counterpart Data											
	α_x (J2000)	δ_x (J2000)	OAA	$S_{2-10}^{(-15)}$	HR	Flag	R	R_{limit}	$\log \frac{L_x}{L_{\odot}}$	z	Class	Notes	$\Delta\lambda_{\text{rest}}$	$\log L_x^{(2-10)}$	$\log N_H$	$\log N_H^-$	$\log N_H^+$
(1)	(2) ^a	(3) ^a	(4)	(5)	(6) ^b	(7) ^c	(8)	(9)	(10)	(11)	(12) ^d	(13) ^e	(14) ^f	(15)	(16) ^g	(17) ^g	(18) ^g
J234820.2+005437	23 48 20.21	+00 54 37.9	4.01	17.80	0.57	1	19.31	23.4	-0.53	0.279	ELG	...	2814–7271	42.6	22.6	22.5	22.7
J234820.8+010024	23 48 20.83	+01 00 24.5	1.93	29.90	-0.38	1	21.19	23.4	0.45	1.208	BLAGN	...	2117–4479	44.3	20.0	<	20.8
J234823.2+010358	23 48 23.23	+01 03 58.7	5.52	8.21	-0.59	1	21.47	23.4	0.00	2.223	BLAGN	...	1739–3350	44.2	21.9	21.6	22.2
J234825.5+010425	23 48 25.58	+01 04 25.6	6.11	21.60	-0.03	1	21.53	23.4	0.45	1.281	BLAGN	...	2452–4603	44.2	21.8	20.9	22.1
J234826.2+010330	23 48 26.28	+01 03 31.0	5.32	52.90	-0.41	1	20.96	23.4	0.61	1.153	BLAGN	...	2575–3771	44.5	21.1	20.0	21.4
J234835.3+005832	23 48 35.32	+00 58 32.9	4.30	54.30	-0.39	1	20.59	23.4	0.47	0.948	BLAGN	...	2512–4594	44.3	<	<	20.0
J234835.5+005836	23 48 35.58	+00 58 36.6	4.37	35.30	-0.10	1	22.66	23.4	1.11	0.948	ELG	...	2733–5390	44.1	22.1	22.0	22.2
J234839.5+010828	23 48 39.58	+01 08 28.7	11.24	49.10	-0.35	1	22.13	23.4	1.04	1.021	ELG	FK	2770–4453	44.3	22.0 ^j
J234840.1+010753	23 48 40.15	+01 07 53.3	10.80	139.00	-0.47	1	18.39	23.4	-0.00	0.717	BLAGN	...	2871–5241	44.4	21.3 ^j

^a X-ray positions are corrected for average X-ray to optical offset (to correct *Chandra* pointing errors); see Paper II.

^b $HR = (H - S)/(H + S)$ where H is the corrected counts in the 2.0 – 10 keV band and S is the corrected counts in the 0.5 – 2.0 keV band. See § 5 for details.

^c See Paper II, § 4 for details of the flag code. Briefly: 0 = no optical coverage, 1 = solid optical ID, 2 = upper limit, 3 = saturated in SEXSI optical image; R -band magnitude taken from the Guide Star Catalog II (McLean et al. 2000), 4 = solid ID but R -band magnitude affected by nearby bright source, 5 = more than one optical source consistent with the X-ray source position, 6 = upper limit (no optical counterpart) but area contaminated by nearby bright source so limiting magnitude is unknown.

^d BLAGN = Broad-Lined AGN, NLAGN = Narrow-Lined AGN, ELG = Emission Line Galaxy, ALG = Absorption Line Galaxy. See § 4 for classification details.

^e Notes (Column 13):

- **A:** optical counterpart falls just outside the strict search area (see § 5 and Table 3).
- **B:** identification from the Guide Star Catalog II (McLean et al. 2000) or VIZIER database.
- **C:** identification from the Einstein Observatory Extended Medium-Sensitivity Survey (Stocke et al. 1991), object MS1214.3+3811.
- **D:** cataclysmic variable, spectrum shows 274 km s⁻¹ blueshift.
- **E:** member of (non-target) nearby galaxy, NGC 5879. This galaxy happened to be in the *Chandra* pointing of SEXSI field QSO 1508. The three 2 – 10 keV sources spectroscopically confirmed to be associated with NGC 5879 are flagged.
- **F:** this object was identified using its 2-D spectrum as it could not easily be extracted to form a 1-D spectrum; the observable wavelength range is thus omitted.
- **G:** in Paper II this source had optflag=5 (> 1 optical source in the search area). Our spectrum shows a BLAGN, thus we have changed the source to optflag=1, a secure optical counterpart identification.
- **H:** confirmed target cluster member (spectroscopically confirmed within 1 Mpc of target cluster center). In Papers I and II sources were flagged as being potentially within 1 Mpc of the target cluster center as determined by their position in the image. These sources were all ignored for the $\log N - \log S$ calculation in Paper I. Now that redshift information is available, only sources at the target cluster z remain flagged. See § 11 for details on these sources.
- **I:** confirmed (non-target) cluster/group detected in Holden et al. (2002) — see § 11.
- **J:** possible BALQSO.
- **K:** line identification or redshift tentative.
- **L:** this source spectrum shows two ELG, one at $z=0.426$, one at $z=1.432$. The nearer source matches the $R=22.25$ in our photometry (Paper II), but the fainter $z=1.432$ source, undetected in our photometry, also appears in the error circle. This source is thus eliminated from our analysis.
- **M:** J145215.6+430448: low-ionization, broad absorption line quasar.
- **N:** spectrum has gap of > 100 Å between red and blue side.

^f Optical spectroscopic wavelength coverage in angstroms.

^g Columns 16–18 present the logarithm of the best-fit N_H value, as well as 1σ low and 1σ high values from the fit. When a N_H measurement is zero we report '<' in the table.

^h HR is lower limit.

ⁱ $\Delta\lambda$ is in the observed frame — no z was measured, only continuum.

^j Source detected on an off-axis ACIS-S chip (2-3) and thus N_H is calculated from HR , not spectral fit. See § 5.

^k N_H is lower limit.

^l Bad XSPEC fit. N_H is calculated from HR , not spectral fit.

TABLE 3
PHOTOMETRY FOR SOURCES WITH SPECTRAL ID OUTSIDE THE FORMAL MATCH
AREA.

CXOSEXSI_ (1)	α_x (J2000) (2) ^a	δ_x (J2000) (3) ^a	R (4)	σ_R (5)	$\Delta\alpha$ (6)	$\Delta\delta$ (7)	Δr (8)	Rad. (9) ^b	$\log \frac{f_x}{f_o}$ (10)
J030527.0+035528	03 05 26.97	+03 55 29.3	17.61	0.17	2.5	0.1	2.5	1.5	-1.50
J084822.5+445854	08 48 22.62	+44 58 55.9	21.08	0.13	-2.3	-0.4	2.3	1.9	-0.50
J084823.9+445852	08 48 23.94	+44 58 53.8	22.01	0.13	-1.8	-0.6	1.9	1.8	0.12
J084824.8+445740	08 48 24.83	+44 57 41.3	20.52	0.13	2.2	-0.5	2.3	1.5	-0.79
J084846.4+444830	08 48 46.46	+44 48 32.0	20.55	0.13	2.2	0.8	2.4	1.5	-0.43
J084931.3+445549	08 49 31.38	+44 55 50.5	21.20	0.13	2.3	1.3	2.7	1.7	-0.22
J090955.5+541813	09 09 55.55	+54 18 15.4	22.21	0.13	-2.7	0.4	2.8	1.7	0.09
J091012.7+541205	09 10 12.74	+54 12 07.8	22.49	0.13	-1.1	3.5	3.6	2.8	0.68
J091034.2+542408	09 10 34.25	+54 24 10.7	21.24	0.12	-2.5	0.1	2.5	1.5	-0.62
J115930.1+291744	11 59 30.16	+29 17 45.2	23.04	0.24	0.4	-1.7	1.8	1.5	0.53
J121739.5+374655	12 17 39.54	+37 46 55.1	23.04	0.27	-1.1	-1.1	1.5	1.5	0.45
J125322.6-090246	12 53 22.64	-09 02 46.5	16.69	0.37	2.1	-2.0	3.0	2.3	-1.43
J131658.1+291017	13 16 58.29	+29 10 18.8	23.69	0.28	-1.3	1.8	2.2	1.5	0.31
J131732.9+291055	13 17 33.06	+29 10 57.3	21.61	0.26	-1.3	0.6	1.5	1.5	-0.38
J133816.8+292350	13 38 16.98	+29 23 51.5	22.89	0.16	1.8	0.3	1.9	1.8	0.85
J150956.0+570534	15 09 56.14	+57 05 34.6	20.46	0.10	0.1	2.9	2.9	1.5	-0.75
J162255.0+263720	16 22 55.12	+26 37 20.4	21.41	0.12	-0.5	-2.7	2.7	1.8	0.33
J170402.8+514247	17 04 02.92	+51 42 48.4	21.76	0.17	-0.2	-1.7	1.7	1.5	0.04
J171740.6+671147	17 17 40.76	+67 11 46.1	21.83	0.05	1.8	-0.8	2.0	1.5	0.02
J171747.4+671449	17 17 47.58	+67 14 48.3	22.91	0.20	1.4	0.4	1.5	1.5	0.55
J175928.1+663851	17 59 28.21	+66 38 51.5	20.22	0.07	-0.2	-2.2	2.3	1.5	-0.10
J204430.7+771215	20 44 30.81	+77 12 15.4	20.77	0.28	-0.8	-1.6	1.8	1.5	-0.21
J205608.1-043210	20 56 08.21	-04 32 11.0	22.24	0.04	-1.1	-1.6	1.9	1.5	0.26

^a X-ray positions are corrected for average X-ray to optical offset (to correct *Chandra* astrometry).

^b The search radius, in arcsec, used for X-ray-to-optical source matching (Paper 2). This radius may be compared with the value in Column (8), the offset from the X-ray source to the optical source in the spectroscopy catalog (Table 2).

TABLE 4
OPTICAL SPECTROSCOPIC LINE DETECTIONS.

Feature	BLAGN			NLAGN			ELG		
	# w/ $\Delta\lambda^a$	# w/ Det.	% Det.	# w/ $\Delta\lambda^a$	# w/ Det.	% Det.	# w/ $\Delta\lambda^a$	# w/ Det.	% Det.
C IV λ 1549	105	66	62%	13	10	76%	0
C III] λ 1909	129	83	64%	16	10	62%	0
Mg II λ 2800	169	151	89%	18	4	22%	112	13	11%
[Ne V] λ 3426	126	26	20%	21	17	80%	147	0	0%
[O II] λ 3727	119	54	45%	21	21	100%	151	115	76%
[Ne III] λ 3869	110	19	17%	19	12	63%	151	10	6%
CaHK $\lambda\lambda$ 3934, 3968	103	20	19%	19	7	36%	148	67	45%
D4000 break	102	10	9%	19	8	42%	146	59	40%
H β	58	26	44%	14	7	50%	113	24	21%
[O III] λ 5007	50	41	82%	14	13	92%	103	68	66%

^a These columns (# w/ $\Delta\lambda$) indicate the number of sources with spectral coverage of the given spectral feature.

TABLE 5
CLUSTER FIELDS: SEXSI SOURCES ASSOCIATED WITH KNOWN CLUSTERS

Field Name	cluster z	# flagged total ^a (# with spectra)	confirmed cluster members	additional cluster members ^b	Notes
AWM 7	0.017	28 (14)			
3C 123	0.218	10 (3)			
CL 0442+0202	1.11	8 (4)	BLAGN ^c		
CL 0848+4454	1.27	7 (5)	ELG, ELG		
RX J0910	1.11	13 (6)	ELG	ELG (~ 1.1 Mpc)	cluster at $z \sim 1.10$, 2 AGN ID ^d
HCG 62	0.014	39 (20)			
RX J1317	0.805	6 (4)	ELG, BLAGN		cluster at $z \sim 0.58$, 2 AGN ID ^d
BD 1338	0.640	5 (1)			
RX J1350	0.804	4 (0)			
3C 295	0.46	3 (3)	ALG, BLAGN		
MKW 3S	0.045	36 (8)			
MS 1621	0.428	6 (3)		ELG (~ 1.9 Mpc)	
RX J1716	0.81	7 (3)	ELG, ELG	ELG (~ 2.1 Mpc)	
MS 2053	0.583	0 (0)			
RX J2247	0.18	17 (9)			
TOTAL		189 (83)	10	3	4

^a A source was flagged in Paper I when it fell within an area potentially less than 1 Mpc from the target cluster center, and excluded from the $\log N - \log S$ calculation to avoid including target cluster members. With the addition of redshift data (# of flagged sources with spectroscopic redshifts are indicated in parenthesis), we can definitively identify or exclude cluster membership. Confirmed cluster members are flagged in the spectroscopic catalog, Table 2.

^b This column indicates sources within ~ 2 Mpc of the cluster center – the particular distances are noted in parenthesis. These sources are not cluster flagged in the Catalog. Their ID's are CXOSEXSI_J091040.8+542006, _J162315.4+263506, and _J171714.5+671136.

^c Cluster member is target radio galaxy, MG1 J04426+0202 (MG 0442+0202), a borderline NLAGN from our spectrum. See Stern et al. (2003).

^d Appendix A of Holden et al. (2002) (paper on RX J1317+2911, RX J1350+6007) notes that there is an X-ray group, CXOU_J091008.6+541856, at $z = 0.68 \pm 0.06$ or $z = 1.18^{+0.08}_{-0.07}$ (T, z degeneracy). We find two ELG (CXOSEXSI_J090954.0+541752 and _J091008.6+541806) at $z = 1.101$ and $z = 1.102$, 1.2 Mpc and 1.0 Mpc away from their reported position, respectively. See § 11.2.

^e Appendix A of Holden et al. (2002) notes that there is a cluster/group, CXOU_J131654.2+291415, at $z = 0.42^{+0.14}_{-0.10}$. We find two ELG (CXO-SEXSI_J131700.2+291307 and _J131706.2+291058) at $z \sim 0.58$, 0.8 Mpc and 2.0 Mpc from the reported position. See § 11.2.

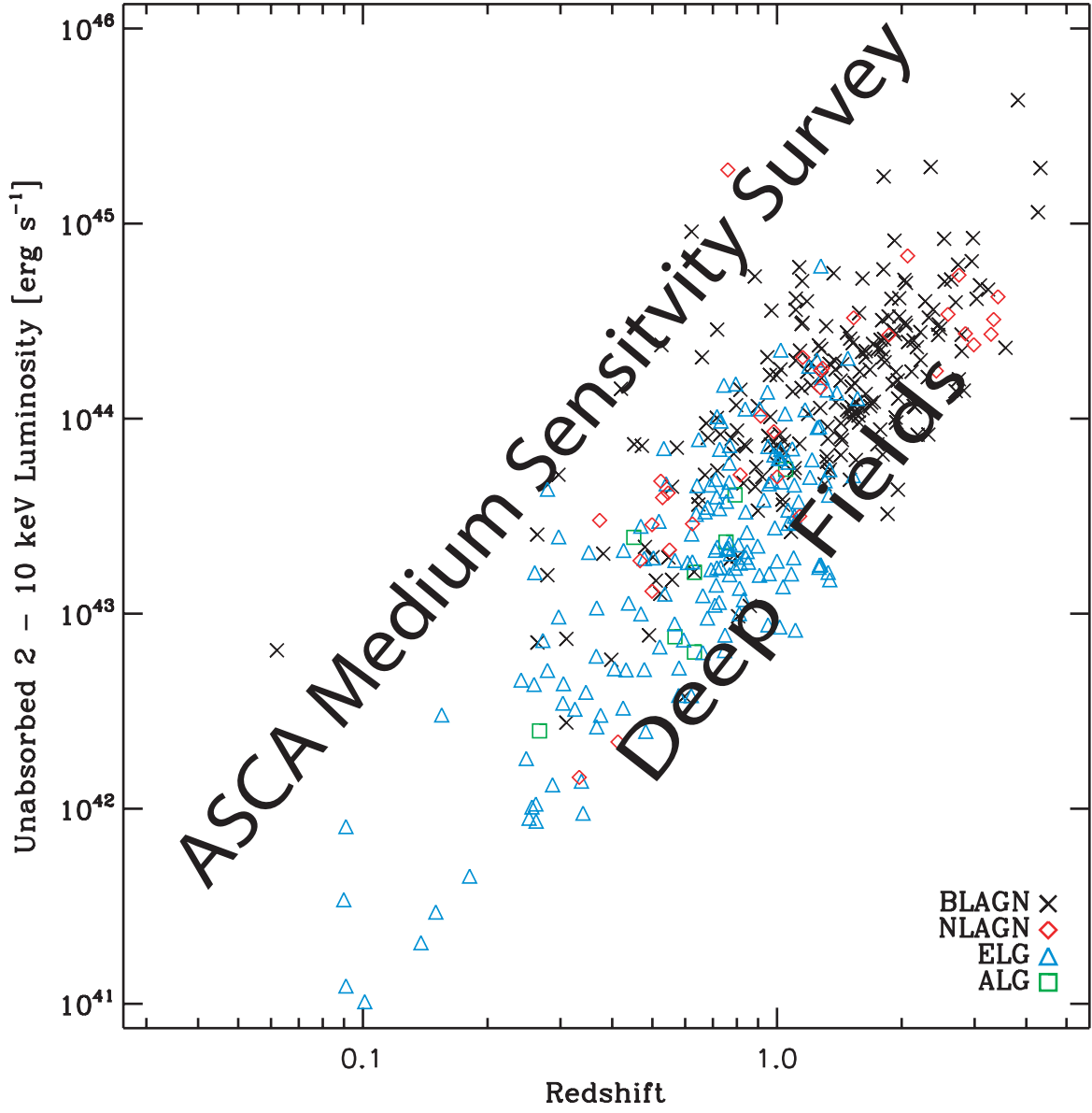


FIG. 1.— Redshift vs. luminosity for SEXSI sources, with optical spectral classification indicated. The approximate phase space covered by the ASCA Medium Sensitivity Survey (Akiyama et al. 2003) and the *Chandra* Deep Fields (e.g., CDF-N – Alexander et al. 2003; Barger et al. 2003; CDF-S – Rosati et al. 2002; Szokoly et al. 2004) is illustrated with text. The luminosity plotted is the intrinsic, unobscured luminosity in the rest-frame 2 – 10 keV band. See § 5 for a description of the unobscured luminosity calculation.

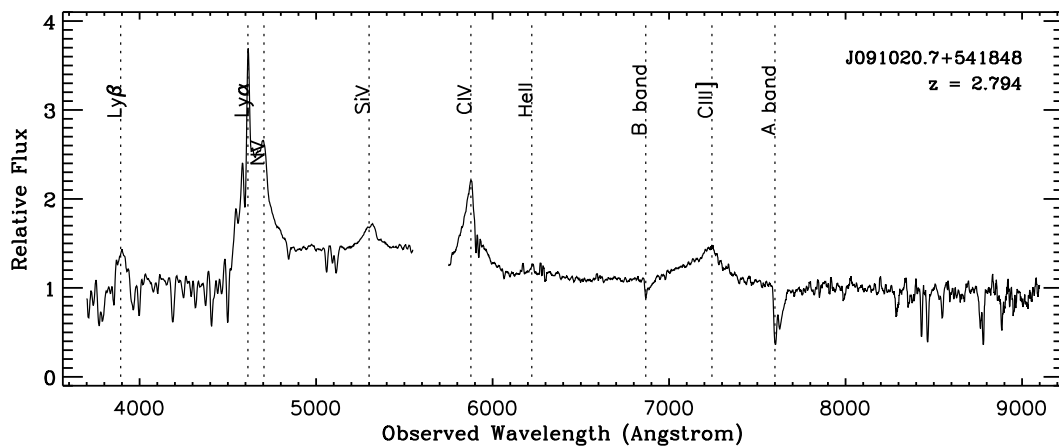


FIG. 2.— Example of one of the 212 SEXSI BLAGN. This source has $z = 2.794$. Note the broad, high-ionization emission lines typical of Type 1 Seyferts and quasars. This spectrum was obtained with LRIS, using a 5600 Å dichroic. The absorptions at 7600 Å (A-band) and 6850 Å (B-band) are telluric in nature.

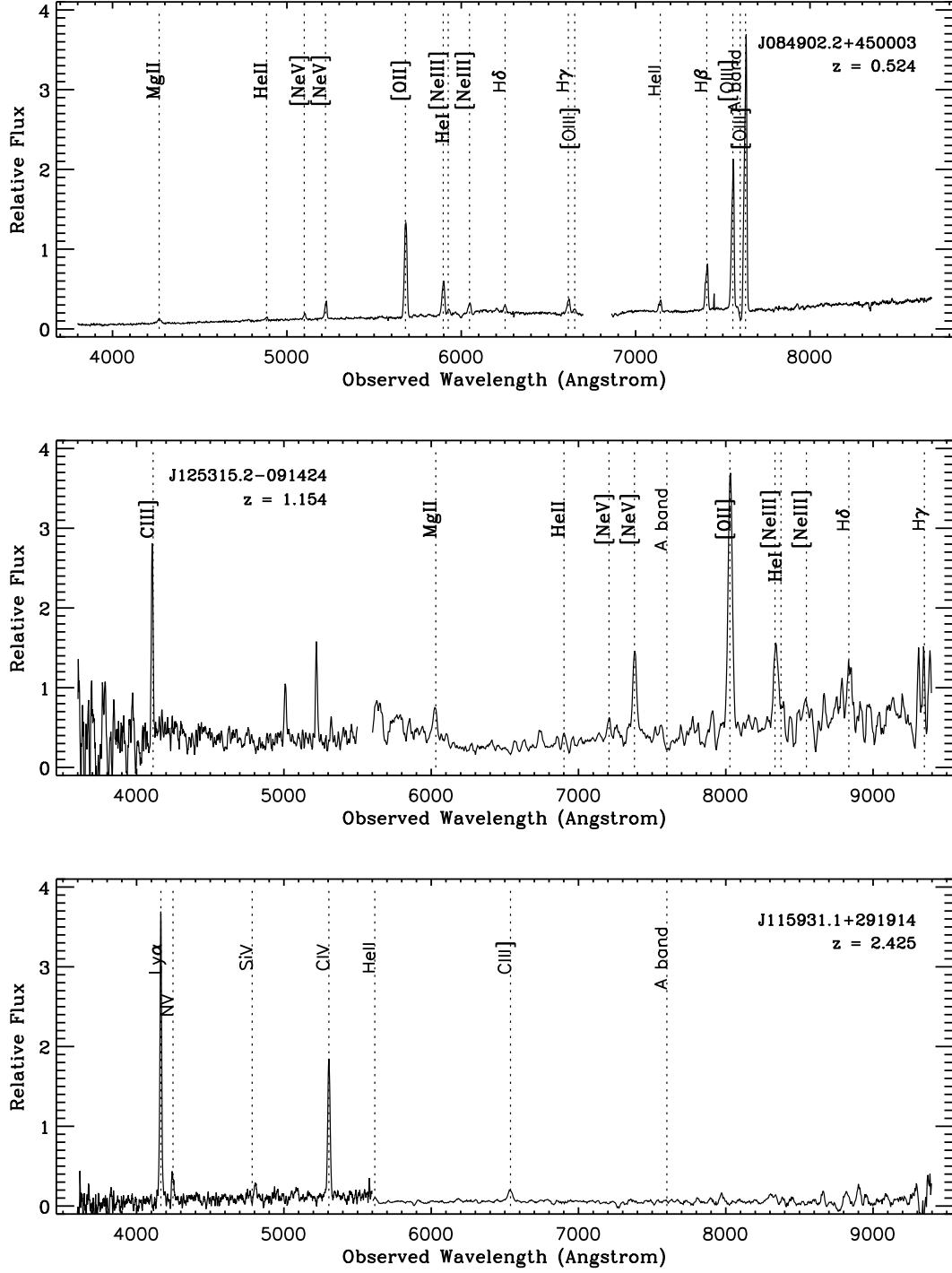


FIG. 3.— Example spectra of NLAGN at $z = 0.5$, $z = 1.2$, and $z = 2.4$. Note the narrow, high-ionization lines. For the lowest- z source (top panel) the classification depends on the [Ne V] $\lambda 3426$ detection, while the higher- z sources have narrow, high-ionization, UV emission lines.

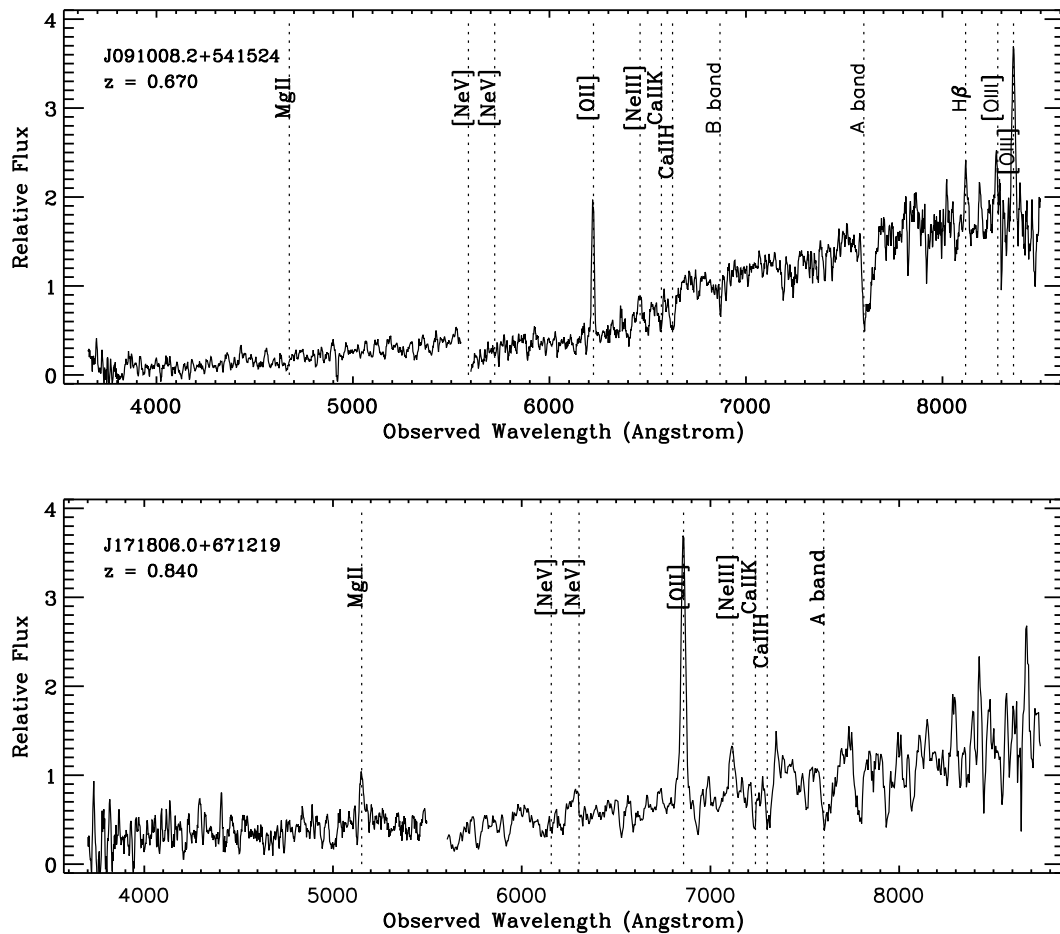


FIG. 4.— Example spectra for two of the 168 SEXSI ELG. The sources show narrow emission and absorption lines typical of normal galaxies and lack [Ne V] $\lambda 3426$.

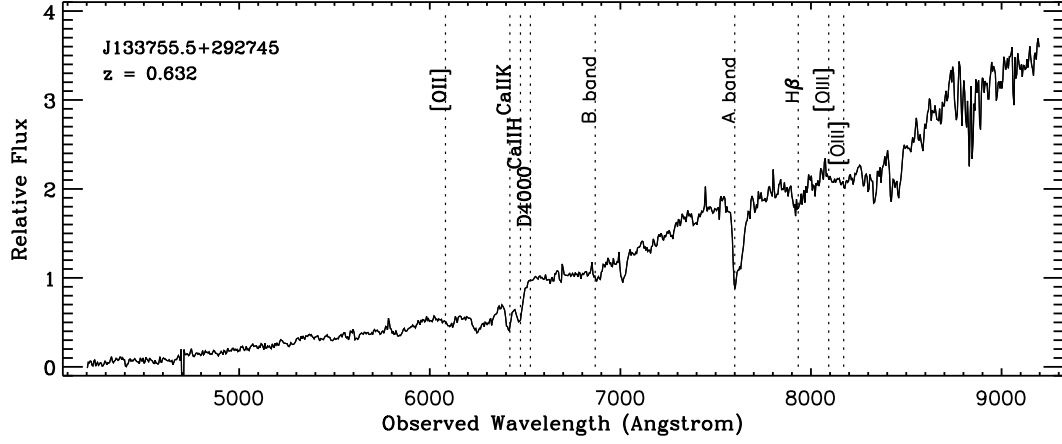


FIG. 5.— Example of one of the eight SEXSI ALG. The ALG are identified by CaHK $\lambda\lambda 3934, 3968$ absorption and the break at 4000 \AA , typical of early-type galaxies. No emission features are detected.

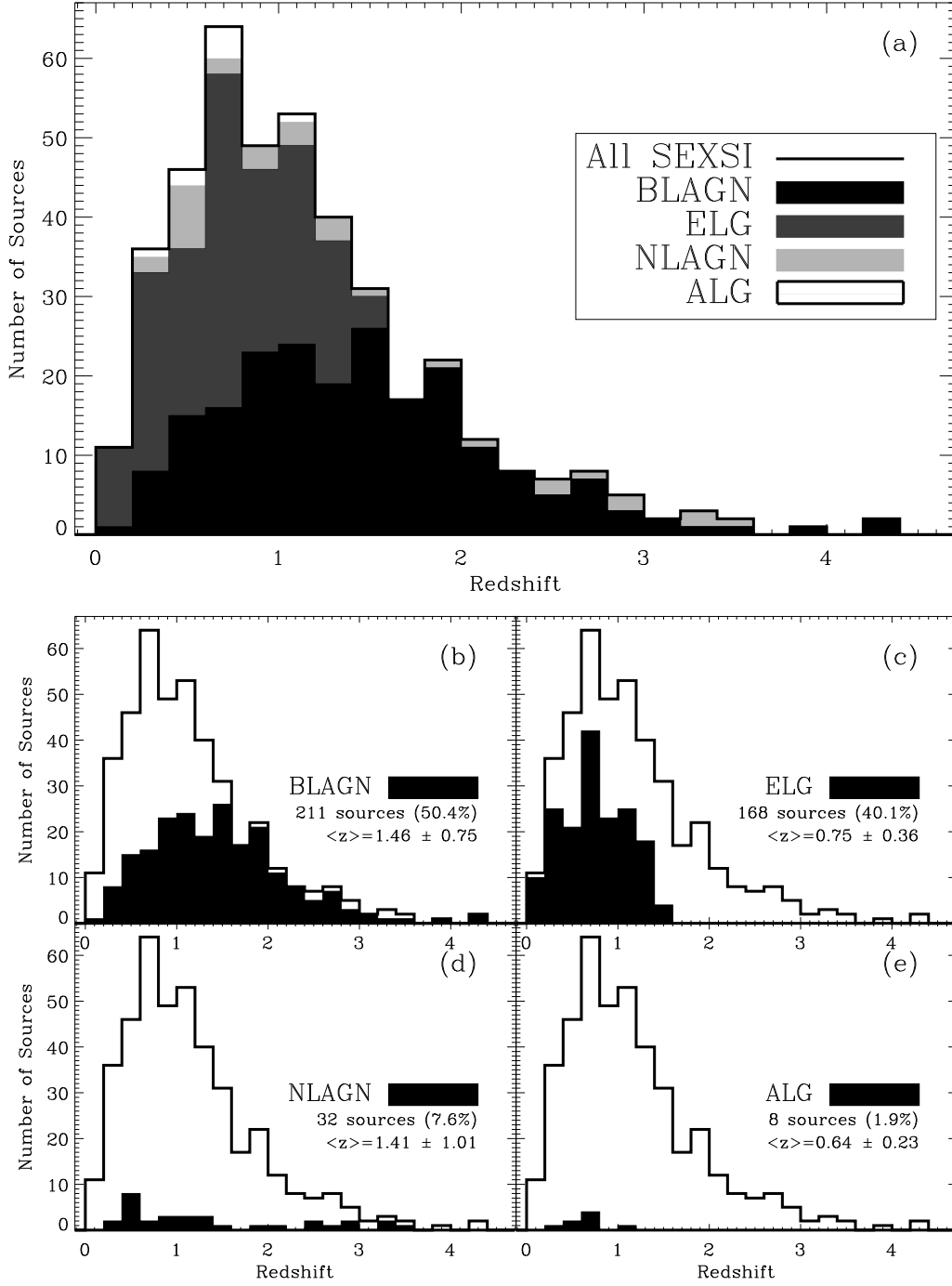


FIG. 6.— Redshift histogram for the 419 sources with spectroscopic redshifts presented in Table 2, excluding the stars (at $z = 0$). Panel (a) shows the entire histogram with shading according to class. Panels (b) – (e) show the same histogram with each individual source class highlighted in black. These plots emphasize that the sample is dominated by the BLAGN, with a broad redshift distribution, and the ELG, dominant at lower- z . The NLAGN have a z -distribution most similar to the BLAGN; the NLAGN are the only narrow-lined sources with $z > 1.5$.

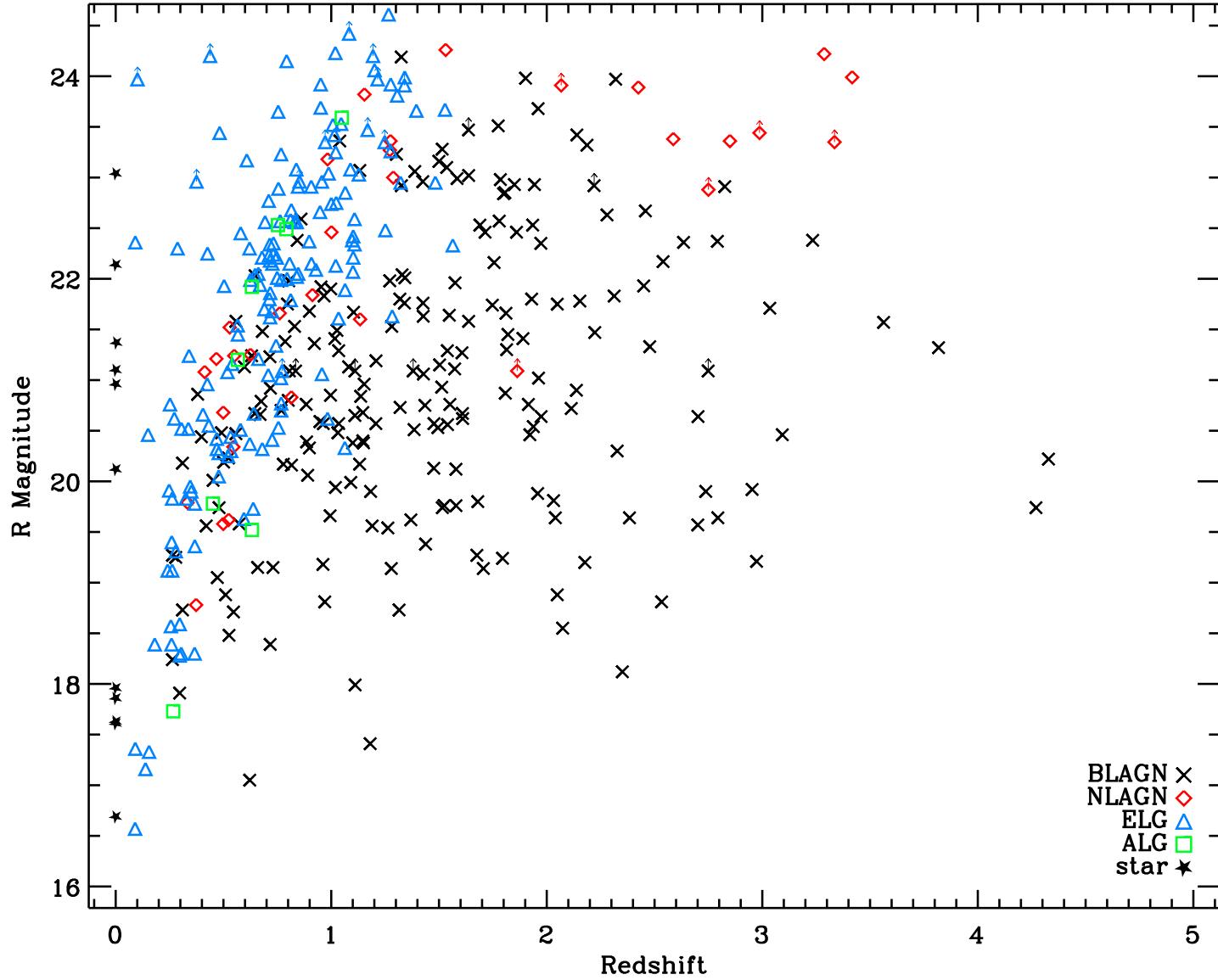


FIG. 7.— R -magnitude versus redshift for spectroscopically-identified sources. The distinct regions in R - z parameter space covered by each class type is illustrated. The BLAGN have the largest spread in z and also occupy a large spread R , though they are not found in as great number at the faintest R fluxes. The NLAGN are also spread widely in z , but tend to be the nearer the faint end of the R distribution. The ELG appear with $z \lesssim 1.5$ and are mainly found to have $R > 20$. The few ALG have a distribution similar to the ELG. Stars with $R > 18$ are most likely chance coincidences, and not real X-ray counterparts.

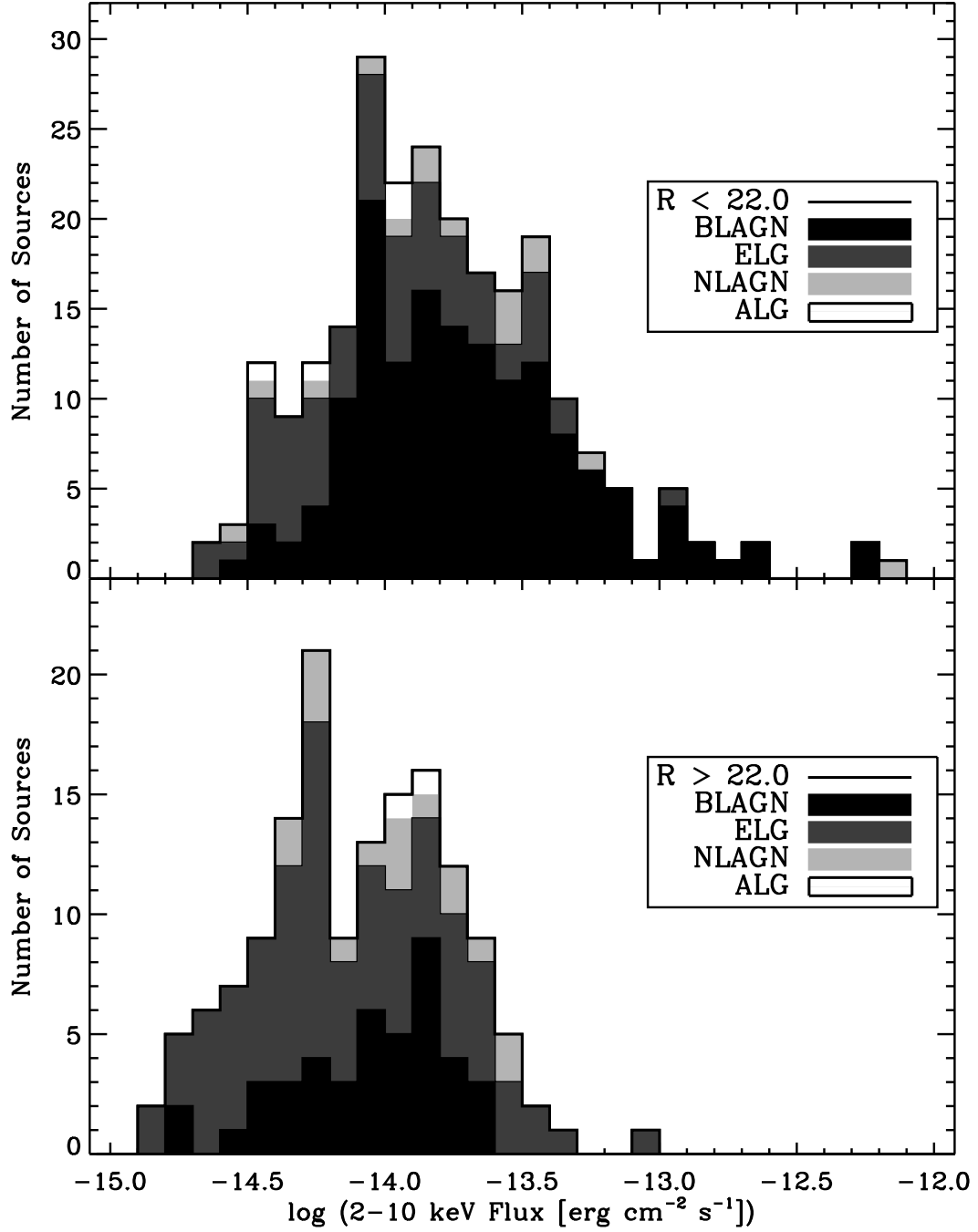


FIG. 8.— The 2–10 keV flux histogram of spectroscopically-identified sources, excluding stars, split at $R = 22$. The optically-brighter sources ($R < 22$), presented in the top panel, show a broad peak between $f_{2-10 \text{ keV}} \sim 10^{-14} \text{ erg cm}^{-2} \text{ s}^{-1}$ and $f_{2-10 \text{ keV}} \sim 10^{-13.5} \text{ erg cm}^{-2} \text{ s}^{-1}$. These $R < 22$ sources are dominated by BLAGN. The bottom panel shows the optically-fainter sources ($R > 22$). The hard-flux histogram is shifted to lower fluxes and includes many ELG as well as BLAGN, ALG, and NLAGN. (Only sources with $R_{\text{limit}} > 22$ are included in this plot. This cut eliminates few sources since most SEXSI imaging has $23 < R_{\text{limit}} < 24$.)

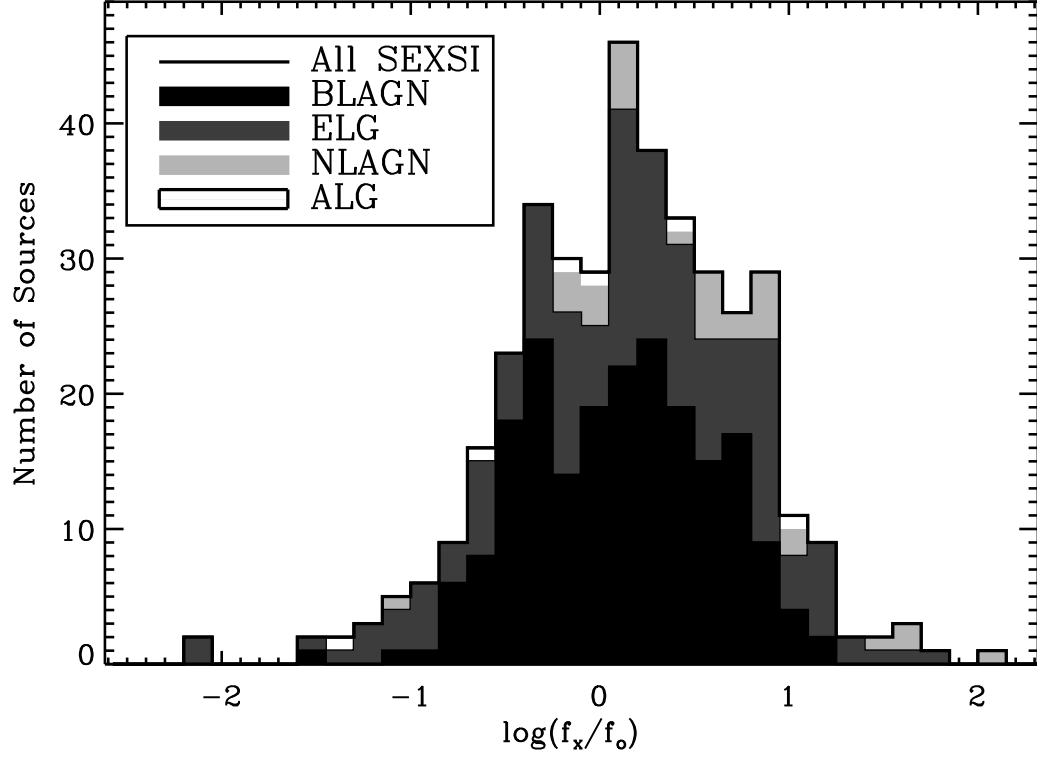


FIG. 9.— Histogram of $\log(f_x/f_o)$ distribution of spectroscopically-identified sources ($f_x = f_{2-10 \text{ keV}}$). Most sources are found between $-1 < \log(f_x/f_o) < 1$, while the NLAGN tend towards higher values of $\log(f_x/f_o)$. At $\log(f_x/f_o) > 1$, all but five of the twenty-six sources lack broad lines.

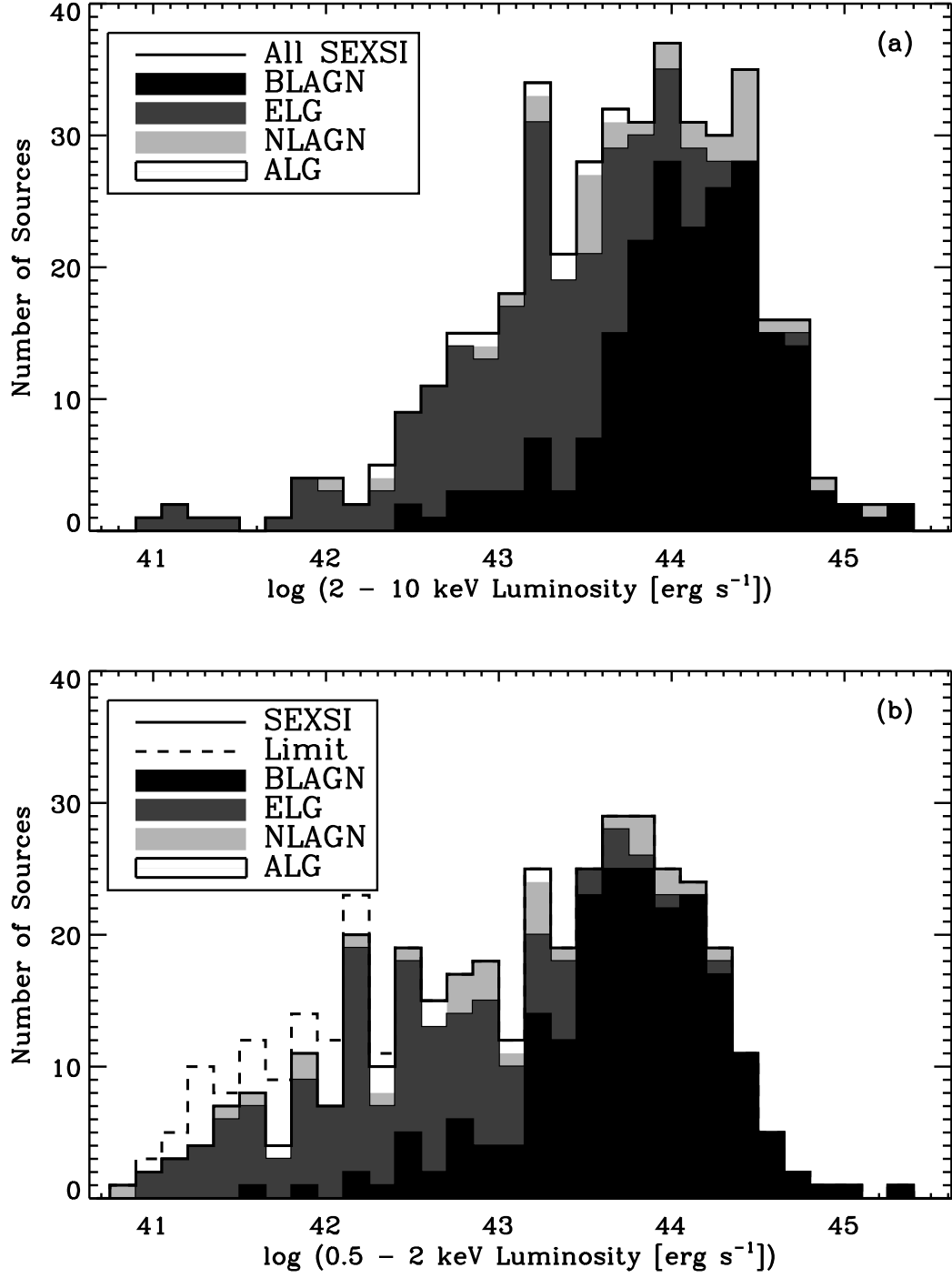


FIG. 10.— X-ray luminosity histograms, uncorrected for intrinsic absorption at the source. The top panel shows the 2 – 10 keV luminosity distribution, while the bottom panel shows the 0.5 – 2 keV distribution. The dashed histogram in the bottom panel indicates the 32 sources with upper limits to $L_{0.5-2.0 \text{ keV}}$; the majority of these sources (26/32) are ELG while 4 are NLAGN.

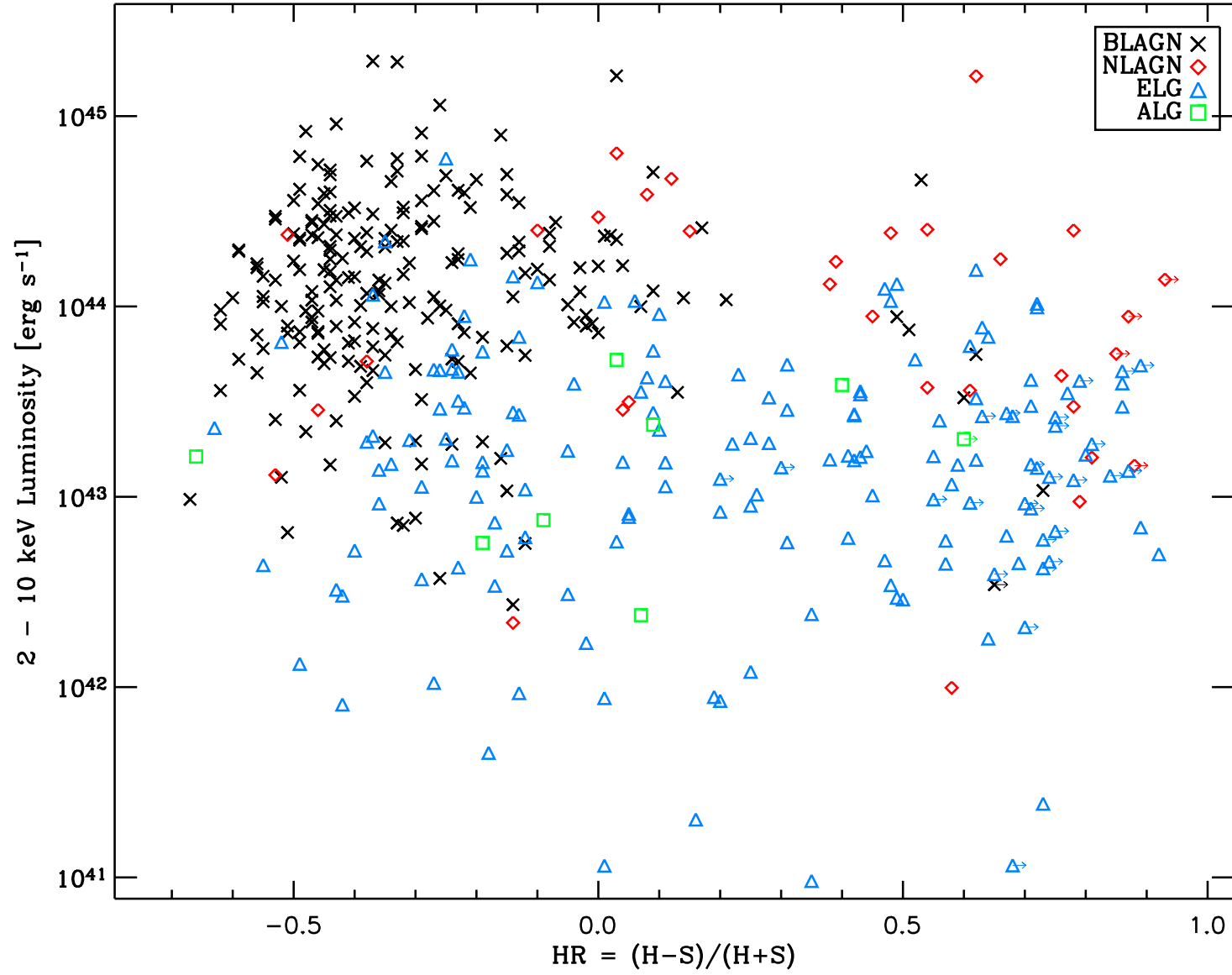


FIG. 11.— 2 – 10 keV luminosity vs. HR . Crosses indicate BLAGN – note that they mainly fall at high luminosity and $HR < 0$. NLAGN are shown in diamonds; most have $HR > 0$, consistent with the notion that obscuration at the source is involved. Emission-line galaxies (triangles) have a wide spread in HR , as do the absorption-line galaxies (squares).

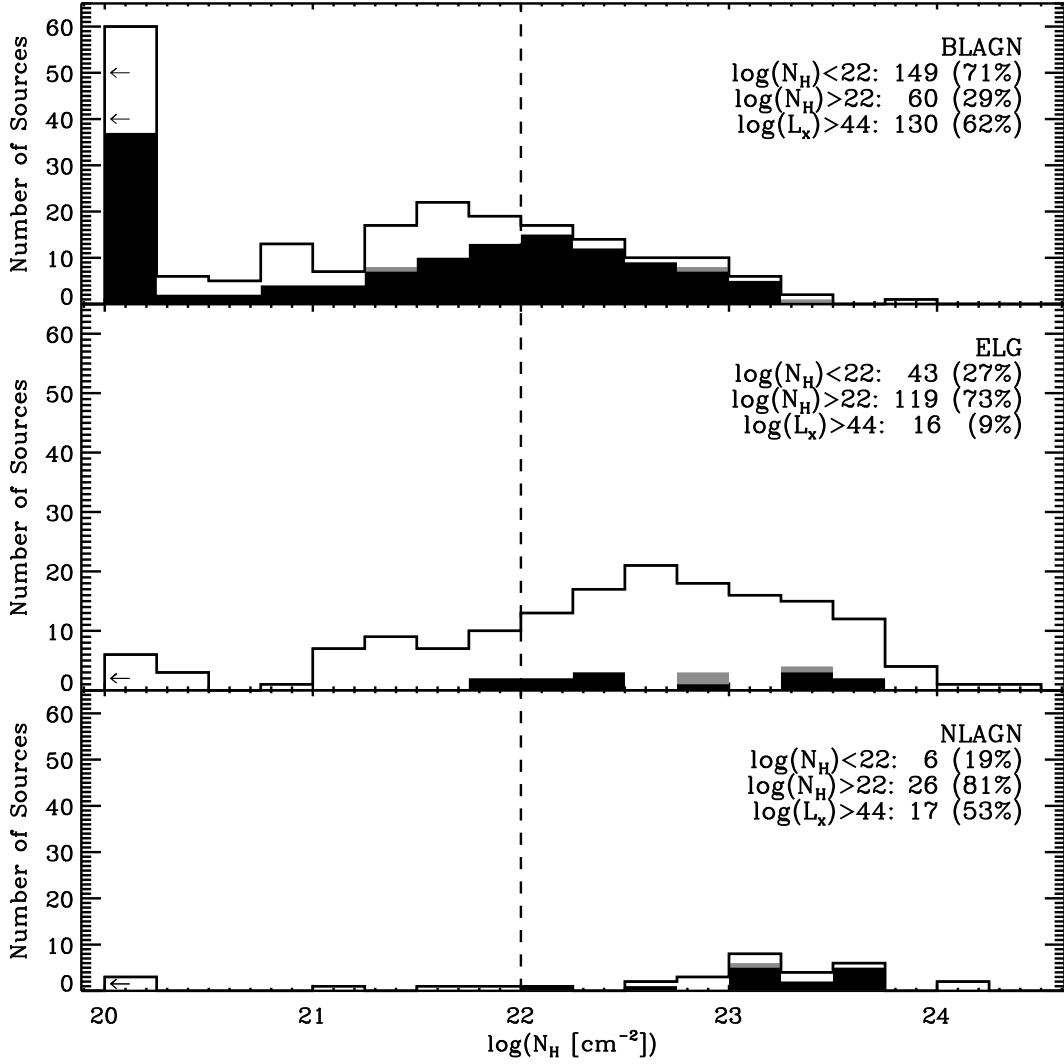


FIG. 12.— N_H histogram for BLAGN, ELG, and NLAGN. The small number of ALG are omitted. Sources with a best-fit N_H value below $\log N_H = 20$ are placed in the bin at 20. The black fill indicates sources with obscured $2-10$ keV rest-frame luminosities above $10^{44} \text{ erg s}^{-1}$, while gray indicates sources with unobscured luminosities above $10^{44} \text{ erg s}^{-1}$. The dashed line shows our adopted break, at $\log N_H = 22$, between obscured sources and unobscured sources. Note that while about half of the SEXSI sources have $N_H > 10^{22} \text{ cm}^{-2}$, it is the BLAGN that dominate the unobscured distribution. The majority of the ELG are obscured as are the NLAGN to an even greater extent.

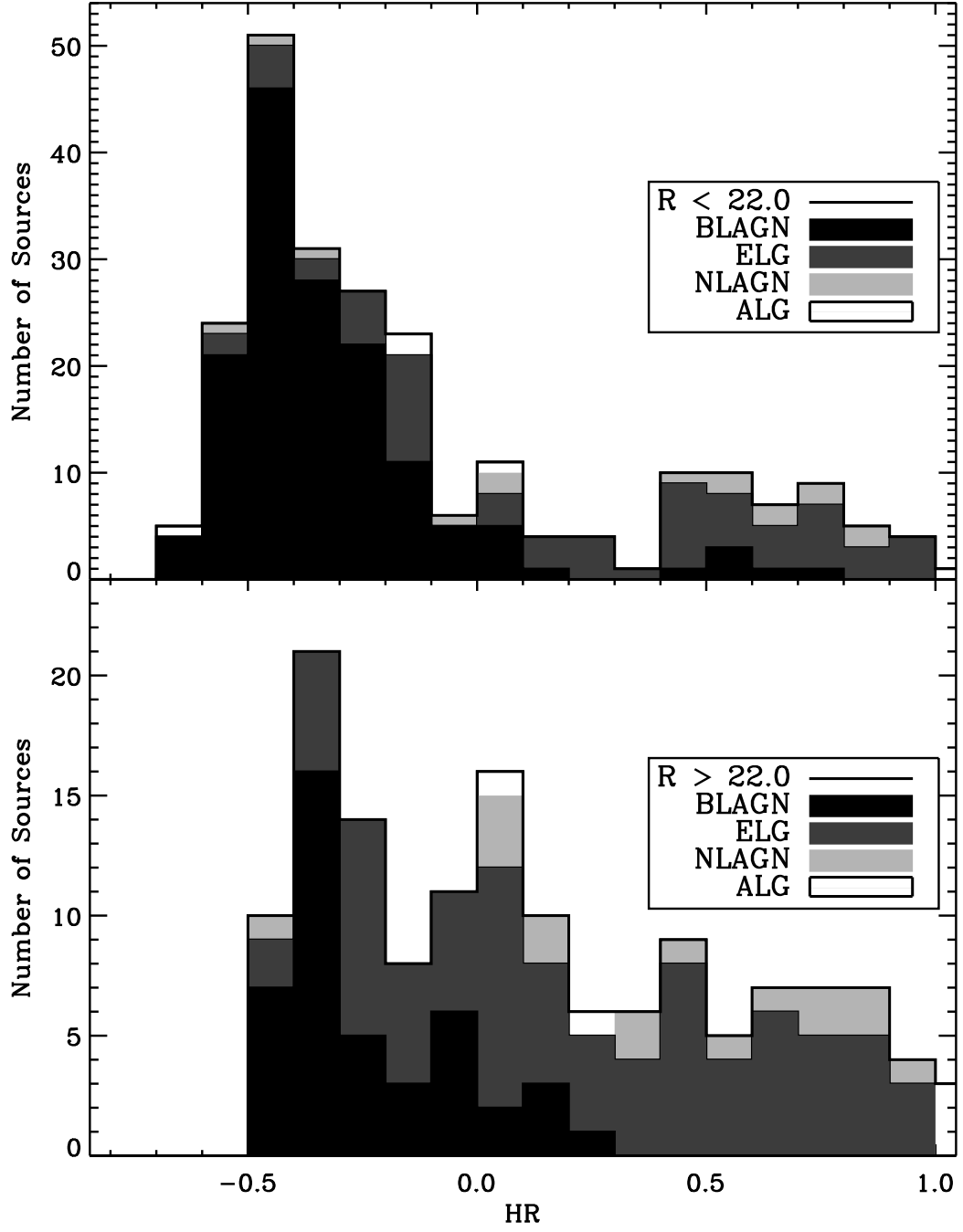


FIG. 13.— Hardness ratio histogram of spectroscopically-identified sources, excluding stars, split at $R = 22$. The top panel shows the optically-brighter sources ($R < 22$). The black-filled peak near $HR = -0.4$ represents the broad-lined sources, which dominate the optically-brighter population of 2 – 10 keV SEXSI sources. The lower panel shows the optically-fainter ($R > 22$) sources which are, on average, much harder and have a broader HR distribution. This group of sources is a mix of spectral classes: there are BLAGN, but in addition there are many ELG, ALG, and NLAGN.

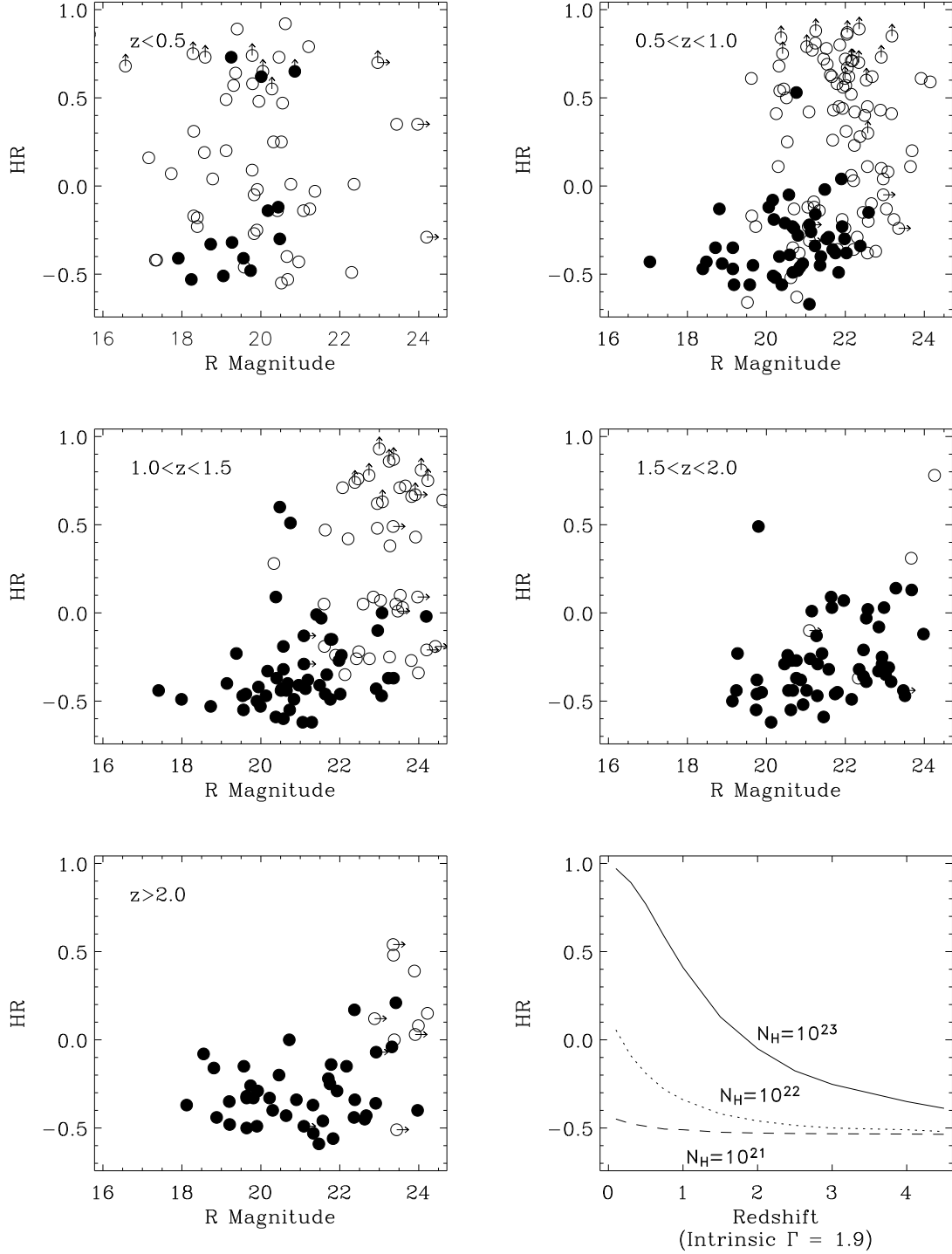


FIG. 14.— HR versus R -magnitude for five redshift ranges. Broad-lined sources (BLAGN) are shown with filled circles, while non-BL sources (NLAGN, ELG, ALG) are open. Arrows indicate limits to the HR (upward pointing) and R -magnitude (right pointing). The abrupt drop in the number of non-BL sources in the highest- z panels ($z > 1.5$) is apparent, and caused both by $[\text{O II}] \lambda 3727$ shifting out of the optical band, and the inability to spectroscopically identify faint sources. The bottom right panel shows HR versus z for three typical values of intrinsic obscuring column density given a source power-law index $\Gamma = 1.9$, for reference. The column densities indicated on the plot are in units of cm^{-2} .

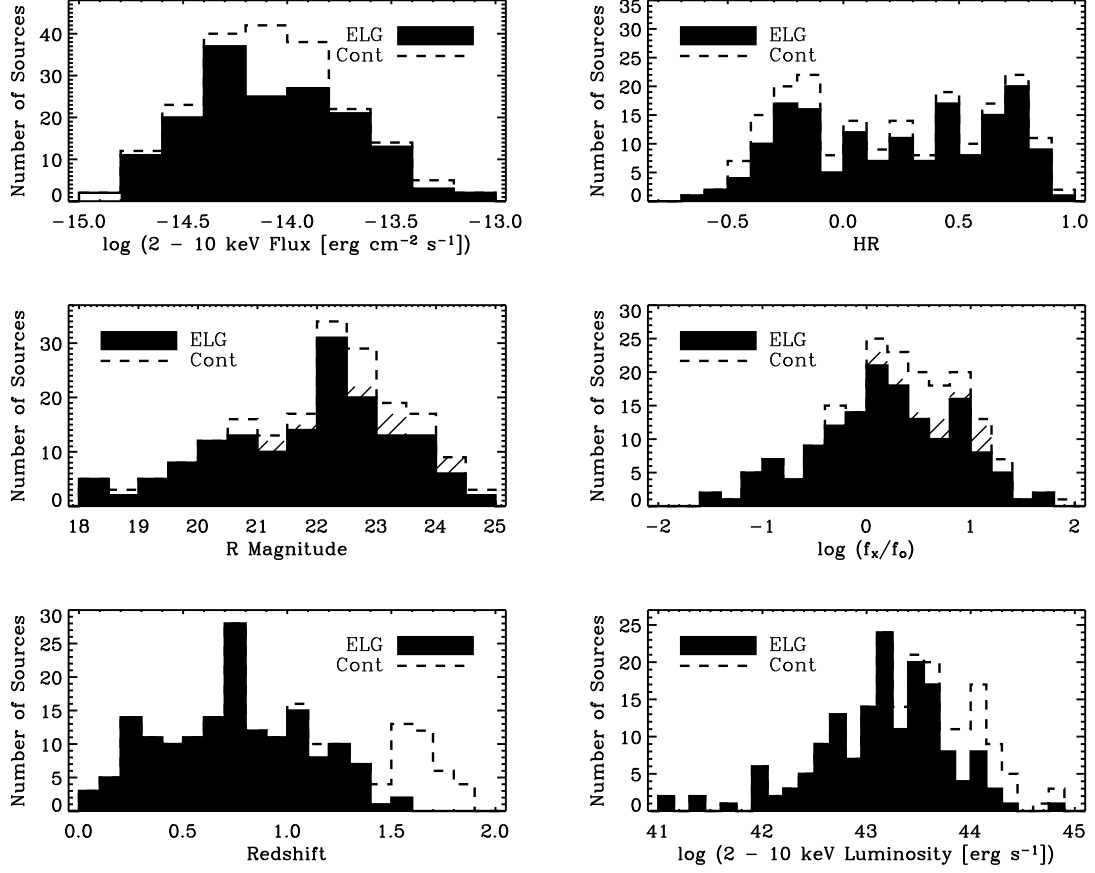


FIG. 15.— The ELG population compared to sources that have spectra with a continuum lacking detected emission or absorption features. The top panels show the 2 – 10 keV flux, HR , R -magnitude, and $\log(f_x/f_o)$ distributions of the ELG (filled black) and the continuum-only sources (dashed line). The hatched regions show the continuum-only sources that have $R = R_{\text{limit}}$. The bottom two panels show the spectroscopic redshift distribution and corresponding L_x distribution for the ELG (filled black). These distributions are compared to distributions of the continuum-only sources whose assigned “redshift limits” were calculated assuming that $[\text{O II}] \lambda 3727$ falls just longward of the optical spectral range for each source.

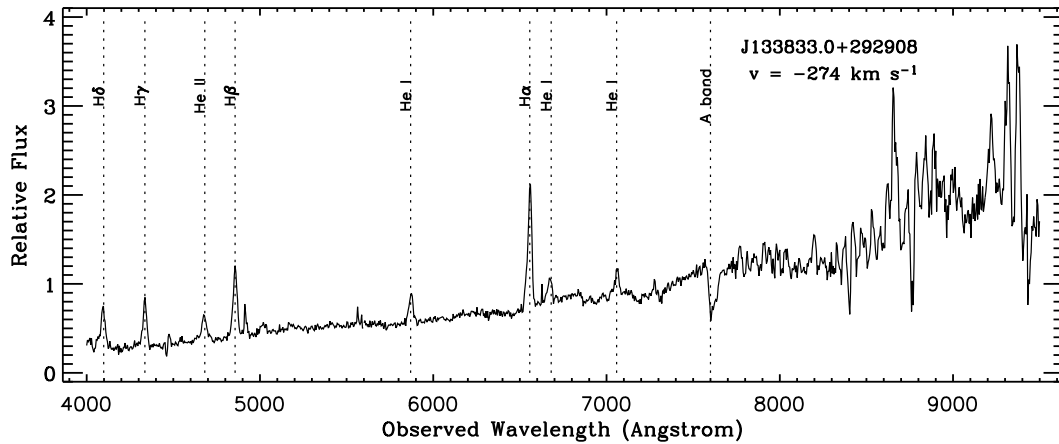


FIG. 16.— A cataclysmic variable (CV) that shows a blueshift of 274 km s^{-1} . This source has $f_{2-10 \text{ keV}} = 3.25 \times 10^{-14} \text{ erg cm}^{-2} \text{ s}^{-1}$, $HR = -0.18$, and $R = 20.1$. The measured velocity indicates either that the star is at an extremum in its orbit or that it is a rare halo-CV.

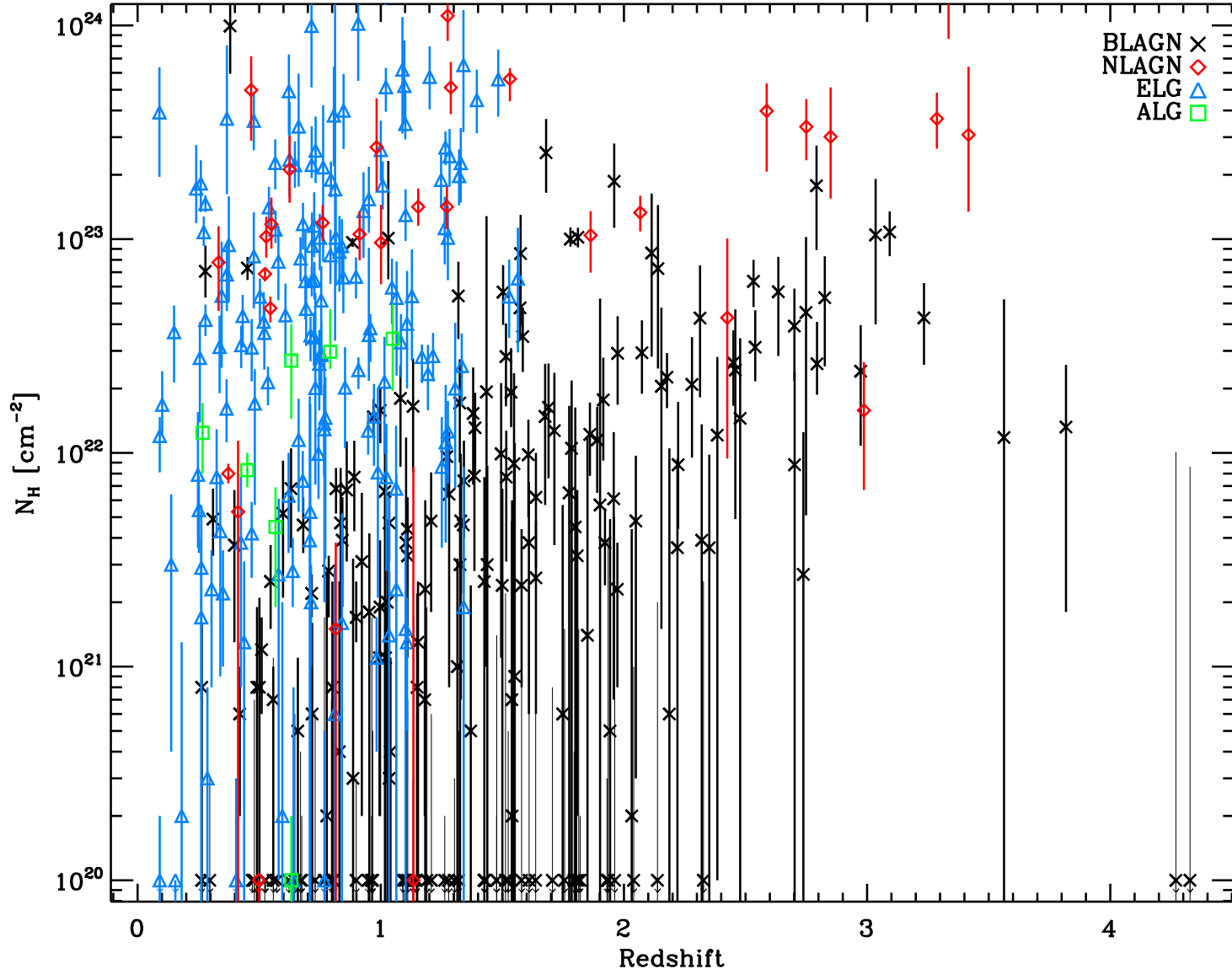


FIG. 17.— N_H versus redshift. 1σ error bars from the XSPEC fits are presented; the 14 sources with N_H values determined from the *HR* (see § 5) are omitted. Sources with a best-fit N_H value below 10^{20} cm^{-2} are placed at 10^{20} cm^{-2} with a downwards-pointing arrow. If the 1σ upper-bound to the N_H is above 10^{20} cm^{-2} then the error bar shows on the plot; conversely if the upper-bound is also below 10^{20} cm^{-2} no error bar is present.

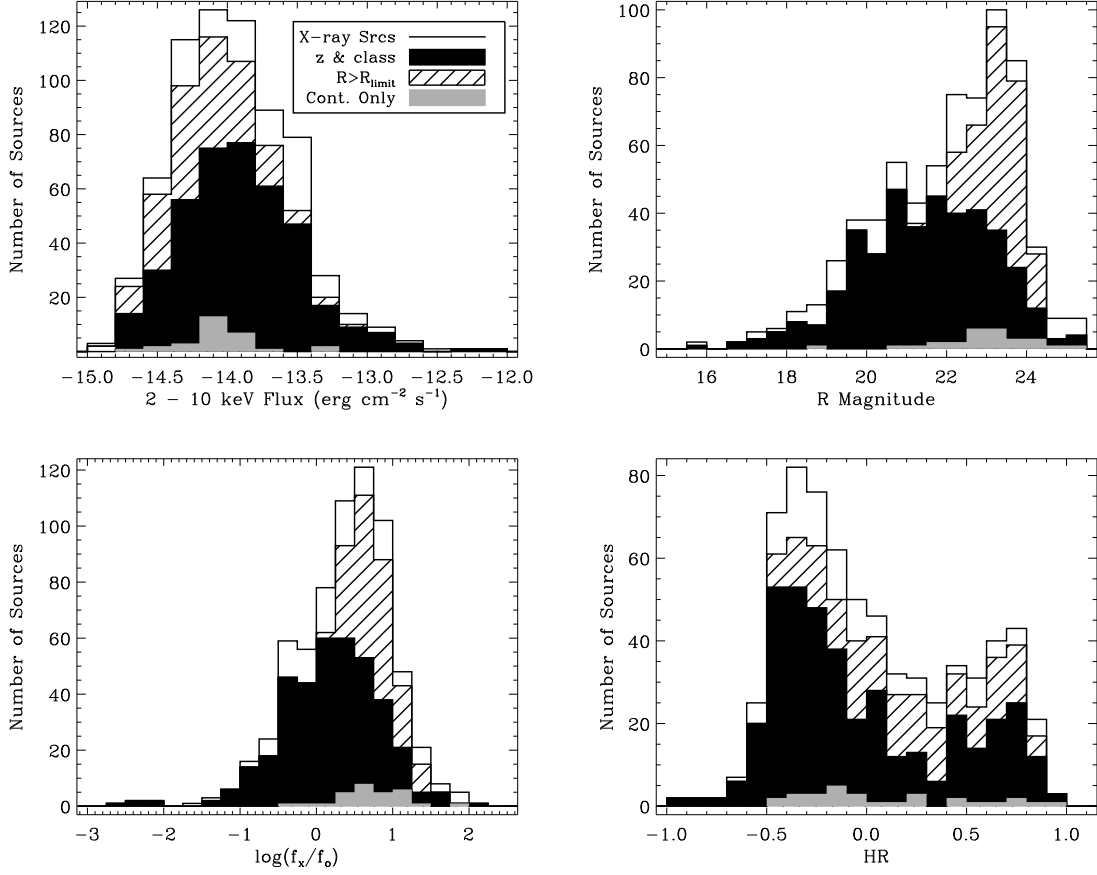


FIG. 18.— Histograms of $f_{2-10 \text{ keV}}$, R , $\log(f_x/f_o)$, and HR from seventeen fields where we have extensive spectral coverage. Each panel shows a histogram of all SEXSI 2 – 10 keV sources from these fields. Sources with a spectroscopic redshift and classification are filled with black and sources with a spectra that show continuum only are shaded in gray. The hatched part of each histogram indicates sources with no photometrically identified optical counterpart ($R > R_{\text{limit}}$). For the R -magnitude and f_x/f_o plot the R -magnitude plotted is R_{limit} . Sources with no shading or hatch marks have optical photometric ID's but no spectroscopic followup.

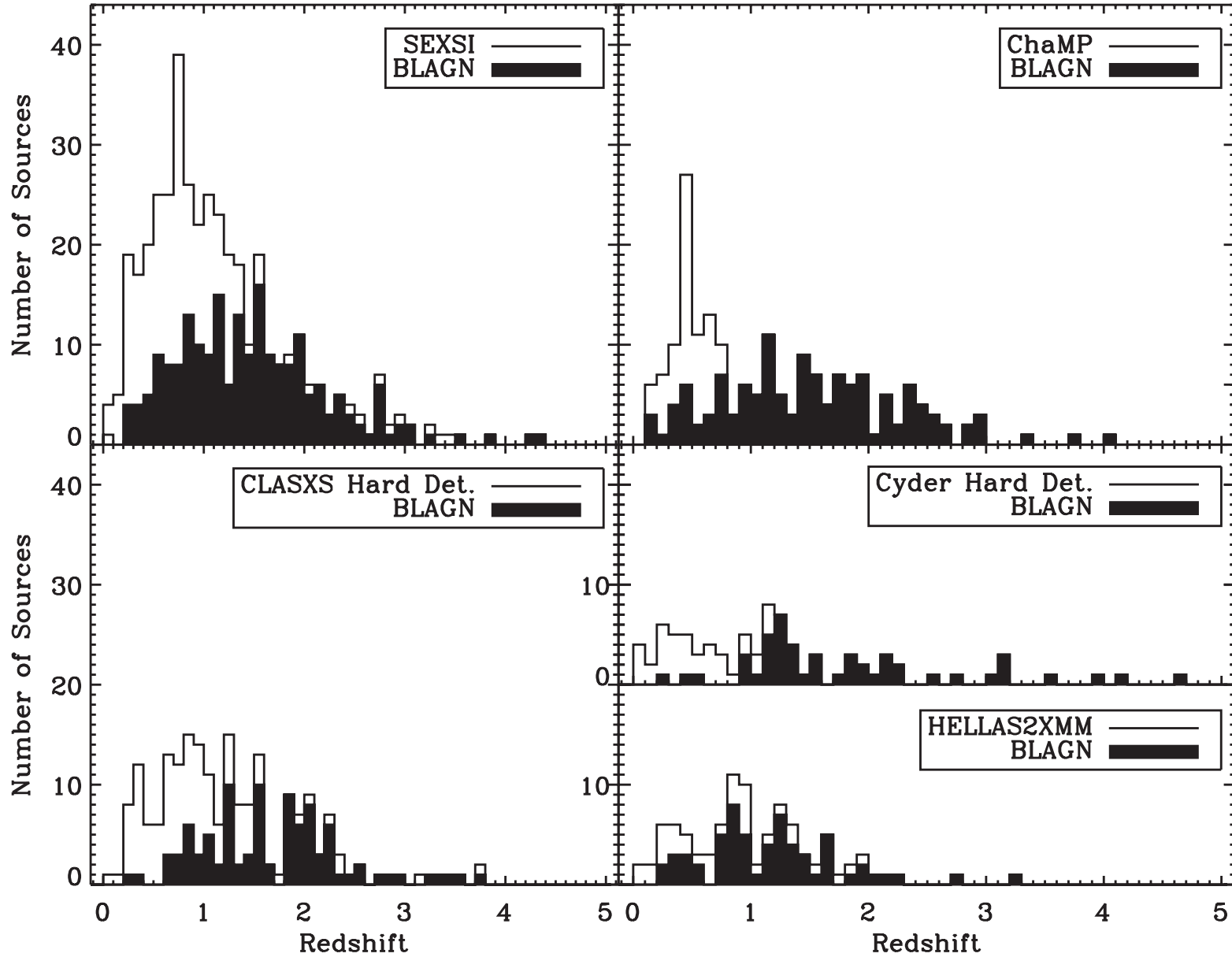


FIG. 19.— Redshift distribution of SEXSI, ChaMP (Silverman et al. 2005), CLASXS (Steffen et al. 2004), CYDER (Treister et al. 2005), and HELLAS2XMM (Fiore et al. 2003). Broad-lined AGN are represented by filled histograms, while non-broad-lined sources are left unshaded. We plot only *hard-band-selected* sources; to this end we have eliminated sources with $f_{2-10 \text{ keV}} < 2 \times 10^{-15} \text{ erg cm}^{-2} \text{ s}^{-1}$. See §9.1 for details.

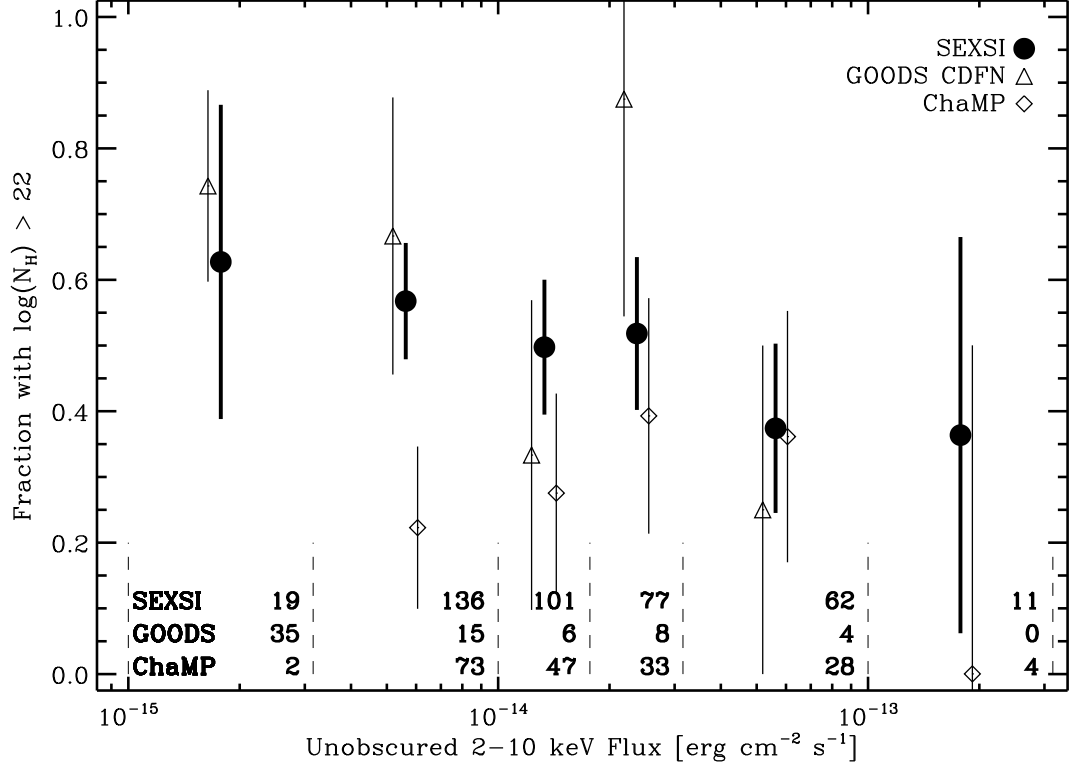


FIG. 20.— Fraction of obscured ($\log N_H > 22$) sources as a function of *unobscured* 2–10 keV flux for the spectroscopically identified samples from SEXSI (filled circles), GOODS CDFN (triangles; E. Treister, private communication), and ChaMP (diamonds; Silverman et al. 2005). The datapoints are calculated using the available catalogs, binned into flux ranges shown by the vertical dashed lines at the bottom of the plot. The errors on the GOODS CDFN fractions are 1σ , calculated from Poisson counting statistics, while the SEXSI and ChaMP error bars incorporate the individual N_H error bars from the spectral fits in addition (see § 9.2 for details). The numbers printed near the bottom of each bin show the number of sources in each bin for each survey. Datapoints are offset slightly along the x-axis for clarity. The GOODS CDFN data lacks sources in the highest flux bin so we omit the datapoint at $\sim 2 \times 10^{-13} \text{ erg cm}^{-2} \text{ s}^{-1}$. Conversely, ChaMP has only two sources below $\sim 3 \times 10^{-15} \text{ erg cm}^{-2} \text{ s}^{-1}$ and we omit the lowest flux datapoint.

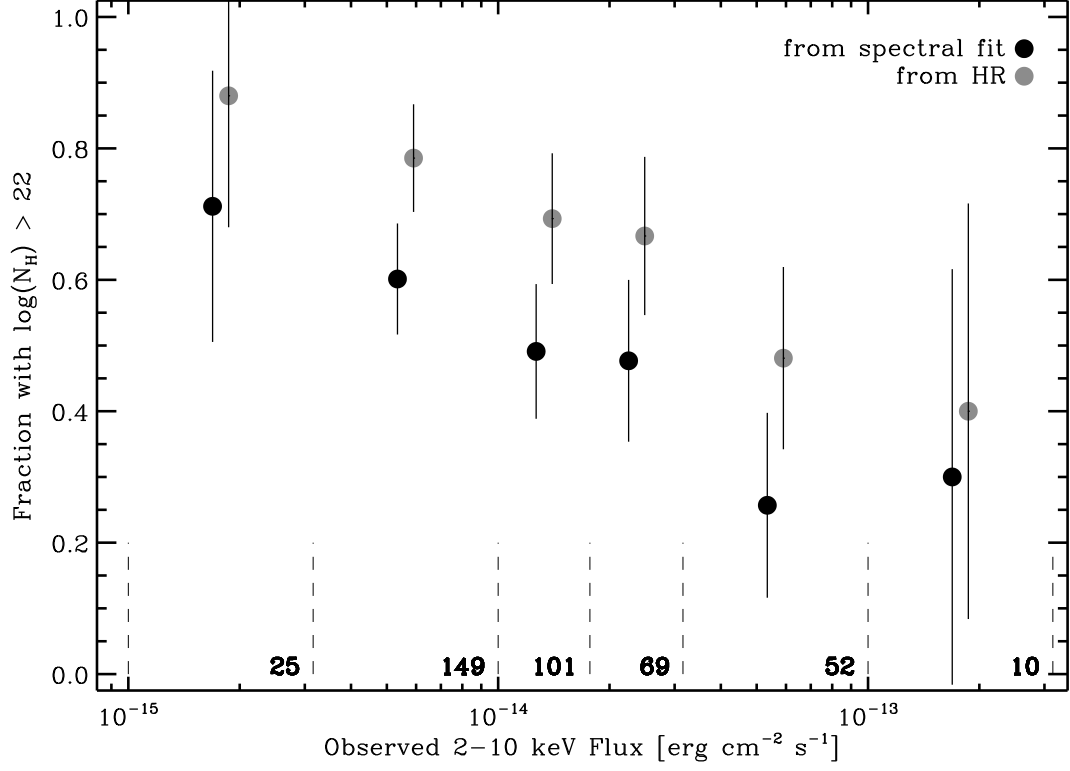


FIG. 21.— Comparison of N_H calculation methods. The fraction of obscured sources as a function of observed (absorbed) 2 – 10 keV flux for SEXSI sources with N_H calculated by X-ray spectral fitting (black), as presented in the source catalog and throughout this article, and from hardness ratios (gray). The HR derived obscured fractions tend to be significantly higher. See § 9.2 for discussion. The number of sources in each bin are shown in text along the bottom.

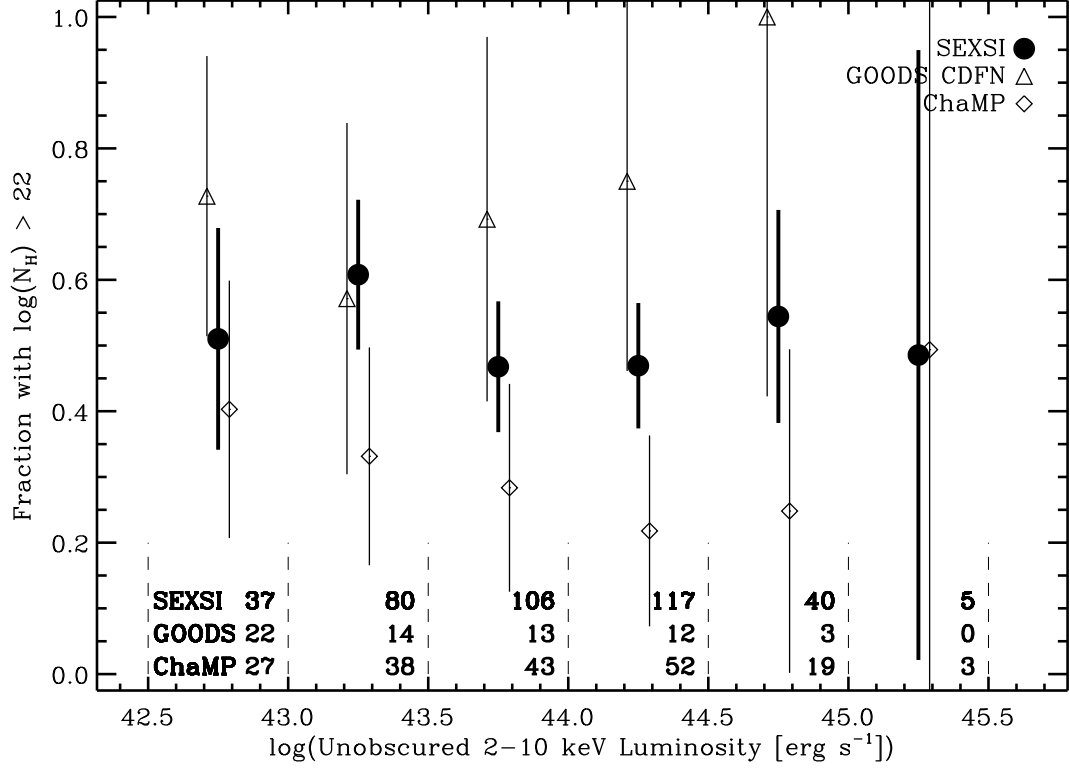


FIG. 22.— Fraction of obscured sources as a function of *unobscured* luminosity for spectroscopically identified sources. The luminosities are calculated based on the observed luminosity corrected for intrinsic N_H . Figure 20 gives references to the catalogs used to calculate the non-SEXSI points. The luminosity bins are shown by the vertical dashed lines at the bottom of the plot; the errors are 1σ , calculated using Poisson counting statistics and the N_H errors when available (for ChaMP and SEXSI). The numbers printed near the bottom of each bin show the number of sources in each bin for each survey. Each datapoint is offset slightly along the x-axis for clarity.

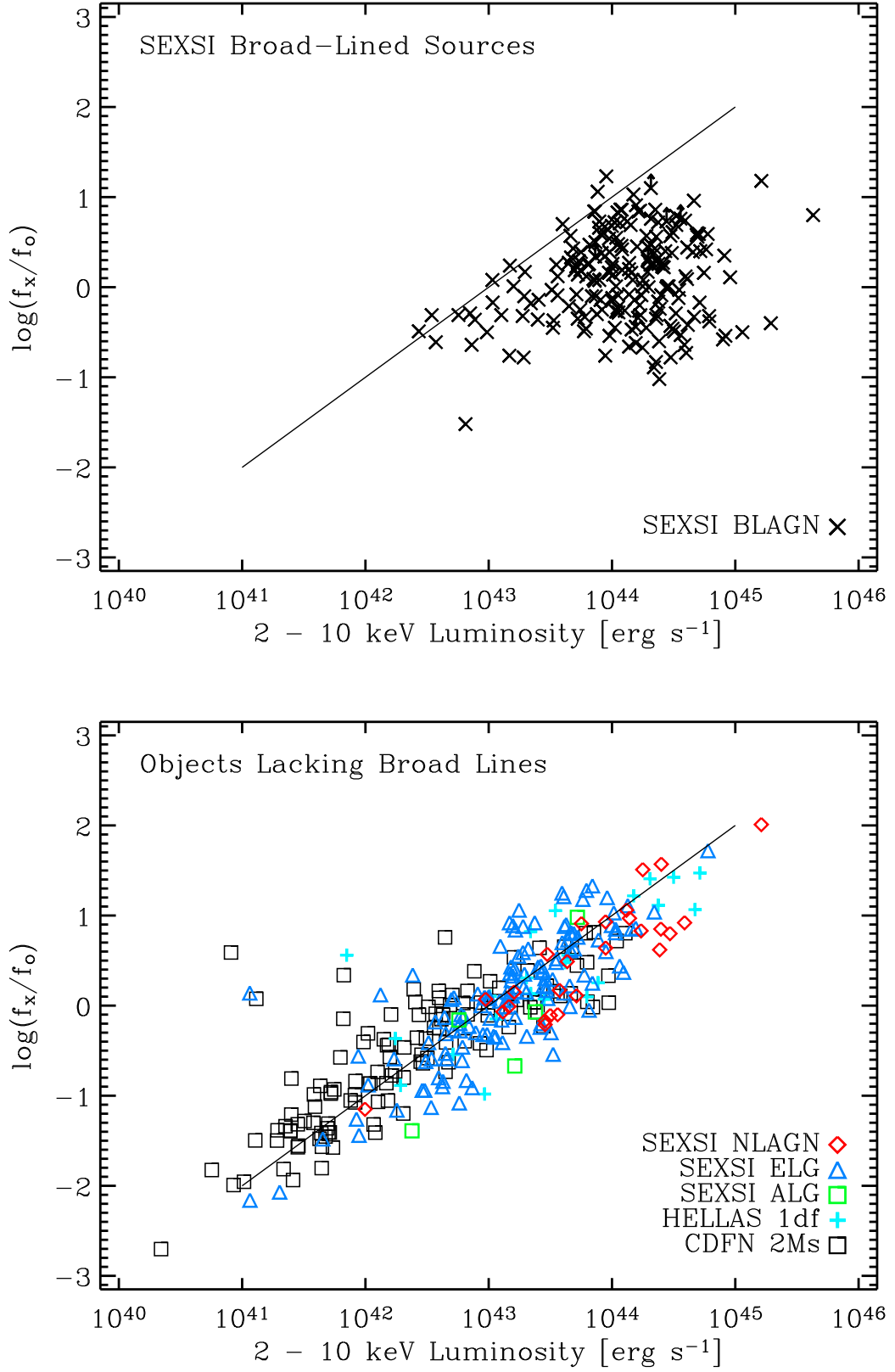


FIG. 23.— These plots show the relationship between $\log(f_x/f_o)$ versus $\log(L_{2-10 \text{ keV}})$ for SEXSI BLAGN (top panel) and sources that lack broad emission lines in their optical spectrum including SEXSI NLAGN, ELG, and ALG as well as the HELLAS2XMM 1 degree field (Fiore et al. 2003) and the CDFN 2Ms sample (Barger et al. 2003). The objects that lack broad lines show a correlation between $\log(f_x/f_o)$ and $\log(L_{2-10 \text{ keV}})$, which would be expected were the optical photometry dominated by galactic light (see §7.3) as opposed to emission from the AGN. The BLAGN do not show the correlation. The line shown in both panels is a linear regression to the data of Fiore et al. (2003).

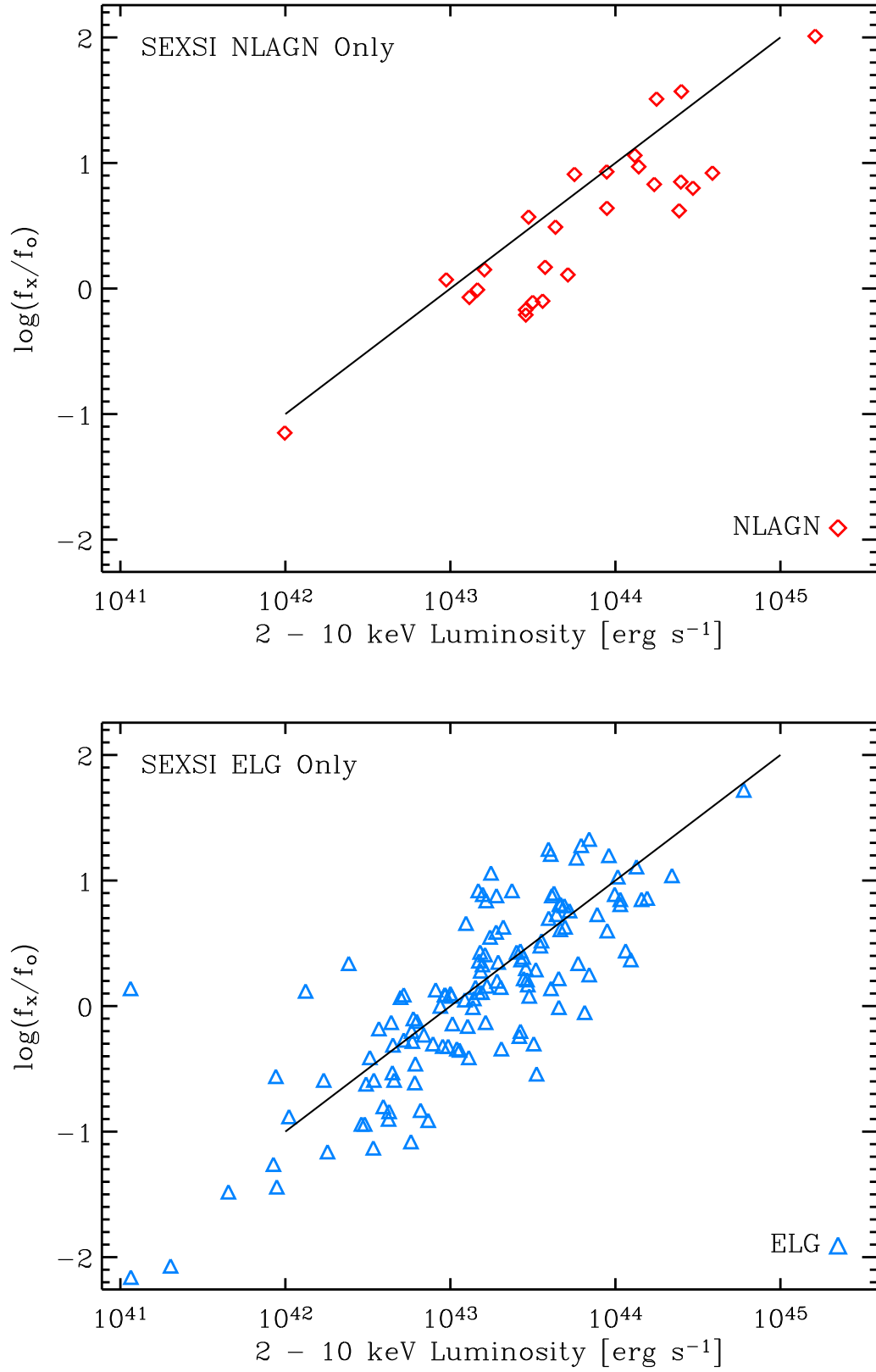


FIG. 24. — Here we again plot the relationship between $\log(f_x/f_o)$ and $\log(L_{2-10 \text{ keV}})$ for the NLAGN and ELG separately. The identified ELG may well be fit by the line (again, from Fiore et al. 2003), but the NLAGN tend to fall below the line.

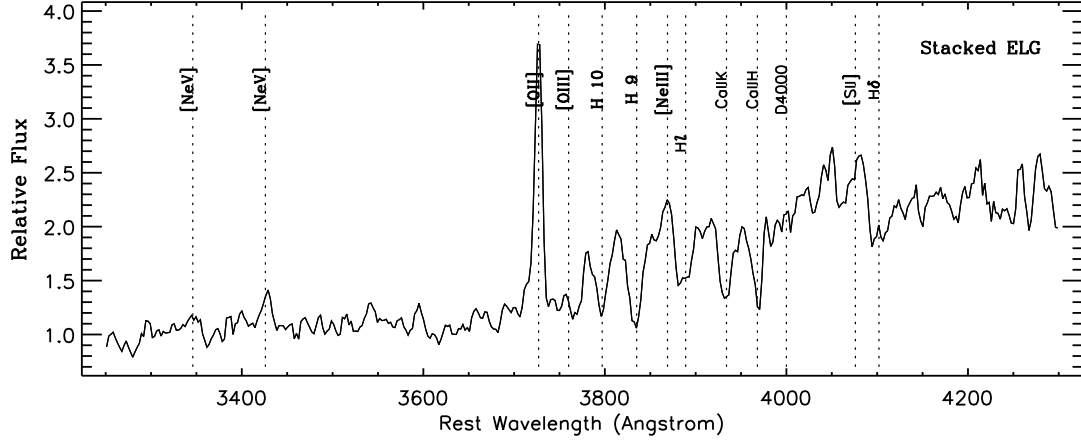


FIG. 25.— Stacked spectrum of 21 ELG all obtained with LRIS on the Keck I Telescope (individual ELG example spectra are shown in Figure 4, for reference). See § 10.3 for further details of the stacking procedure. Note that the individual ELG spectra do not show evidence of the [Ne V] $\lambda 3426$ high-ionization emission line indicative of underlying AGN activity, while the increased S/N of the stacked spectrum does show the [Ne V] $\lambda 3426$ emission. In addition, [Ne III] $\lambda 3869$ emission and several absorption features from ~ 3800 – 4000 Å are well detected.